QUANTITATIVE DETERMINATION OF GAS-PHASE THERMODYNAMIC BARRIERS OF PROTEINS FOR NATIVE ION MOBILITY-MASS SPECTROMETRY: APPLICATIONS AND IMPLEMENTATION OF AN IMPROVED IMPULSIVE COLLISION THEORY

by

Samantha O. Shepherd

A dissertation accepted and approved in partial fulfillment of the
requirements for the degree of
Doctor of Philosophy
in Chemistry

Dissertation Committee:
Michael J. Harms, Chair
James S. Prell, Advisor
Cathy Wong, Core Member
Marian Hettiaratchi, Core Member

University of Oregon

Winter 2024

© 2024 Samantha O. Shepherd

DISSERTATION ABSTRACT

Samantha O. Shepherd

Doctor of Philosophy in Chemistry

Title: *Quantitative determination of gas-phase thermodynamic barriers of proteins for native Ion Mobility-Mass Spectrometry: applications and implementation of an Improved Impulsive Collision Theory*

Ion mobility-mass spectrometry is a powerful tool for identifying and elucidating biomolecular structures and behaviors. This technique is able to retain even weak and non-covalent interactions permitting the study of native or native-like gas-phase biomolecular complexes including folded proteins, protein-protein complexes, and protein-ligand complexes. Historically, energetic and thermodynamic information has been limited to techniques on specialized instrumentation and/or computationally expensive strategies. This changed with the development of “proto-IonSPA” to allow rapid determination of thermochemical barriers for protein dissociation and unfolding on modern, commercially available instrumentation.

In this work, reproducibility, repeatability, and applications of the use of thermochemical measurements on modern, commercially available instruments are assessed, inspired by a need to compare gas-phase dissociation and unfolding of proteins more broadly. This groundwork enables the development of an Improved Impulsive Collision Theory (IICT) in a Monte-Carlo python script, which in turn improves qualitative and quantitative understanding of activation in Collision Induced Unfolding and Dissociation. This program further enables the determination of gas-phase thermochemical barriers for the dissociation of proteins in modern commercially available mass spectrometers. Reasonable agreement is shown with literature standards and between different mass spectrometer designs and experimental parameters. This agreement is

particularly noteworthy due to the drastic difference in timescales being compared (seconds in the literature to as low as microseconds in this work) This dissertation includes previously published co-authored material.

CURRICULUM VITAE

NAME OF AUTHOR: Samantha O. Shepherd

GRADUATE AND UNDERGRADUATE SCHOOLS ATTENDED:

University of Oregon, Eugene, OR

Brandeis University, Waltham, MA

DEGREES AWARDED:

Doctor of Philosophy, Chemistry, 2024 University of Oregon

Masters of Science, Chemistry, 2022 University of Oregon

Bachelors of Science, Chemistry and Studio Art, 2018 Brandeis University

AREAS OF SPECIAL INTEREST:

Mass spectrometry

Thermodynamics

Protein Structure Determination and Quantitation

GRANTS, AWARDS, AND HONORS:

Dean’s First Year Merit Award, University of Oregon, 2018

Excellence in Chemistry, Brandeis University, 2018

Jordan-Dreyer Fellowship for Summer Research, 2017

PUBLICATIONS:

1. **SO Shepherd**, KR Newton, AW Green, JC May, J McLean, RT Kurulugama, JS Prell. "IonSPA: Ion Simulations of Physics of Activation, an improved impulsive collision theory." *In preparation.*
2. **SO Shepherd**, AW Green, ES Resendiz, KR Newton, RT Kurulugama, JS Prell. "Investigation of capillary position on unintentional in-source activation influencing collision induced dissociation and unfolding on a Waters Synapt G2-S*i* and an Agilent 6545 XT Q-TOF Mass Spectrometer." *JASMS. 2024.*
3. J Dorogin, HB Hochstatter, **SO Shepherd**, *JE Svendsen*, *MA Benz,* AC Powers, KM Fear, JM Townsend, JS Prell, P Hosseinzadeh, MH Hettiaratchi. "*Moderate-Affinity Affibodies for Bone Morphogenetic Protein-2 to Tune Protein Delivery Rates and Bioactivity*." *Adv. Healthc. Mat.* (2023).
4. MT Donor*, JW Wilson*, **SO Shepherd***, and JS Prell. "*Lipid Head Group Adduction to Soluble Proteins Follows Gas-Phase Basicity Predictions: Dissociation Barriers and Charge Abstraction*." *IJMS.* (2021).
5. M Cheung See Kit, **SO Shepherd**, JS Prell, and IK Webb. "*Experimental Determination of Activation Energies for Covalent Bond Formation via Ion/Ion Reactions and Competing Processes.*" *JASMS.* (2021).
6. C Konow, Z Li, **SO Shepherd**, D Bullara, I Epstein. "*Influence of survival, promotion, and growth on pattern formation in zebrafish skin.*" *Sci. Rep.* (2021).
7. JW Wilson, MT Donor, **SO Shepherd**, and JS Prell. "*Increasing Collisional Activation of Protein Complexes Using Smaller Aperture Source Sampling Cones on a Synapt Q-IM-TOF Instrument with a Stepwave Source*." *JASMS.* (2020).
8. MT Donor, **SO Shepherd**, and JS Prell. "*Rapid Determination of Activation Energies for Gas-Phase Protein Unfolding and Dissociation in a Q-IM-ToF Mass Spectrometer*." *JASMS.* (2020).

ACKNOWLEDGMENTS

I would like to thank my advisor, Dr. Jim Prell, for his continued mentorship and support in my development as a quantitative experimental scientist. This work would not have been possible without his mentorship. I am thankful for the members of my committee and their commitment to supporting me through every step of the doctoral process as well as their insightful feedback on my work and potential career trajectories. I have a deep appreciation for the students that I have had the opportunity to mentor and work in collaboration with during my time in the Prell lab; their insight, new ways of looking at problems, and excitement in the face of the “science science-ing” brought me joy, focus, and motivation throughout my PhD studies.

I would also like to thank the collaborators I had the opportunity of working with during my PhD, both on work presented in this dissertation with Kenneth Newton and Ruwan Kurulugama, and on research outside of the scope of this dissertation. This research outside of the scope of this dissertation work provided me with a great breadth of experiments and knowledge and inspired me to move closer to biological studies.

I would also like to thank the funding that has supported the work in this PhD Agilent University Relations Award and renewal (JSP), Agilent Technologies for the loan of a 6545XT Q-TOF Mass Spectrometer (JSP), NIH Grant R01 – GM 144507 (JSP), and NSF REU Grant 1949900 CHE (ESR).

Finally, I would like to thank the extensive support network I have had the pleasure to lean on throughout this process. Without my friends both in and out of graduate school, graduated and still working, old and young, I would not have had the wisdom, insight, motivation, or resources to complete this PhD.

Table of Contents

Chapter Page

I. INTRODUCTION 17

Quantitative energetics by mass spectrometry....................................19

History of mass spectrometry and native mass spectrometry....................................21

nano-electrospray ionization (nESI)....................................23

Reproducibility 26

Activation of Proteins and Peptides 28

Ion Mobility....................................30

Collision Induced Unfolding and Dissociation (CIU/D)....................................31

In this dissertation… 33

II. LIPID HEAD GROUP ADDUCTION TO SOLUBLE PROTEINS FOLLOWS GAS-PHASE BASICITY PREDICTIONS: DISSOCIATION BARRIERS AND CHARGE ABSTRACTION....................................35

Abstract....................................35

Introduction....................................36

Materials and Methods 41

Sample preparation....................................41

Native IM-MS and CID....................................41

Data analysis 42

Results and Discussion 43

Mass spectra of lipid head group binding. 44

CID of protein-head group complexes: proton abstraction. 48

CID of protein-head group complexes: dissociation energies. 49

Activation energies for protein-head group CID. 51

Non-specific binding to a larger soluble protein: transferrin. 53

Competitive head group binding to transferrin 55

Conclusions...58

III. EFFECTS OF NANO-ELECTROSPRAY IONIZATION EMITTER POSITION ON UNINTENTIONAL IN-SOURCE ACTIVATION OF PEPTIDE AND PROTEIN IONS 60

Abstract...60

Introduction...61

Methods 64

Results and Discussion 66

Choice of samples. 66

Assessment of protein CIU and CID repeatability using a single nESI emitter and fixed emitter position...67

Reproducibility of CID and CIU using fixed vs. uncontrolled nESI emitter position. 69

Spatial map of extent of in-source activation due to emitter position in CID experiments. .72

Variation of protein CIU fingerprints at fixed emitter positions as measured using RMSD. 75

Differences in CIU fingerprints collected at different emitter positions as measured by RMSD. 77

Differences in CIU fingerprints at different emitter positions as measured using CIU50 78

Conclusions 79

IV. AN IMPROVED IMPULSIVE COLLISION THEORY FOR DETERMINING THERMOCHEMICAL BARRIERS OF NATIVE PROTEIN COMPLEX DISSOCIATION WITH MODERN MASS SPECTROMETERS 81

Abstract 82

Introduction 83

Methods 85

Results and discussion 88

Choice of standards 88

To compare structural disruption between laboratories and over time a standardized, internally referenced energy metric is needed 88

The Improved Impulsive Collision Theory (IICT) reasonably models ion internal energy through ion activation in modern commercially available instruments 90

Enthalpy and entropy values calculated with IonSPA can show high precision in determination across pressures and instruments. 95

Enthalpy and entropy values calculated with IonSPA show moderate agreement with BIRD values. 96

Consideration of Uncertainty. 98

Conclusion 99

V. OUTLOOK 102

APPENDICES 104

A. SUPPORTING INFORMATION FOR LIPID HEAD GROUP ADDUCTION TO SOLUBLE PROTEINS FOLLOWS GAS-PHASE BASICITY PREDICTIONS: DISSOCIATION BARRIERS AND CHARGE ABSTRACTION 104

Theory and Data Analysis....104

B. SUPPORTING INFORMATION FOR EFFECTS OF NANO-ELECTROSPRAY IONIZATION EMITTER POSITION ON UNINTENTIONAL IN-SOURCE ACTIVATION OF PEPTIDE AND PROTEIN IONS 118

Appendix S2: RMSD analysis 124

REFERENCES CITED 138

List of Figures

Figure Page Number

Figure II-1. Schematic potential energy surface for native protein-adduct complex in aqueous solution....38

Figure II-2. Structures of lipid head groups 44

Figure II-3. Mass spectra of GPC, PS, PC, PG, and PE bound to Ubq....45

Figure II-4. Mass spectra of GPC, PC, PE, PG, and PS bound to LZ 47

Figure II-5. Breakdown curves for dissociation of lipid head groups 52

Figure II-6. Gibbs free energies of dissociation for lipid head groups bound to Ubq and LZ 53

Figure II-7. Mass spectra showing lipid head group adduction to TF....55

Figure II-8. Deconvolved mass spectra of lipid head group binding to transferrin at different levels of collisional activation. 57

Figure III-1. Mass spectra for myoglobin ions....67

Figure III-2. CIU fingerprints of NIST mAb25+....69

Figure III-3. CID breakdown curves (a-c, e-g) and CIU fingerprint differences 70

Figure III-4. (a) A map of the effect 73

Figure III-5. Statistics for RMSD of quintuplicates of BSA collected on three separate days....76

Figure III-6. Statistics for CIU50 transitions in far (blue) and close (red) positions....78

Figure IV-1. CID breakdown curves for dissociation of heme from holomyoglobin^{9+}................88

Figure IV-2. Schematic cartoon representing key steps in the IICT (Improved Impulsive Collision theory)...92

Figure IV-3. Fits of pseudo-atom mass based on MD simulations. 92

Figure IV-4. Temperature vs. time curves showing the effective temperature of the holomyglobin 9+ ions 94

Figure IV-5. Thermodynamic barriers determined by IonSPA. 95

Figure IV-6. Overall thermodynamic barriers determined by IonSPA. 96

Figure A-S1. Mass spectra of (a) ubiquitin (Ubq) and (b) lysozyme (LZ). 105

Figure A-S2: Mass spectra of Ubiquitin and GPC...106

Figure A-S3: Mass spectra of Ubiquitin and PC 106

Figure A-S4: Mass spectra of Ubiquitin and PS..107

Figure A-S5: Mass spectra of Ubiquitin and PE..107

Figure A-S6: Mass spectra of Ubiquitin and PG 108

Figure A-S7: Mass spectra of Lysozyme and PS 108

Figure A-S8: Mass spectra of Lysozyme and PG...109

Figure A-S9: Mass spectra of Lysozyme and PE 109

Figure A-S10: Mass spectra of Lysozyme and PC 110

Figure A-S11: Mass spectra of Lysozyme and GPC 110

Figure A-S12. Eyring plots for CID of ubiquitin, 5+ losing bound lipid head groups 112

Figure A-S13. Eyring plots for CID of lysozyme, 7+ losing bound lipid head groups.............113

Figure A-S14. Native mass spectra of transferrin with no lipid head group present.................115

Figure A-S15. Change in weighted-average charge state of isolated TF19+ with increasing collisional activation...116

Figure A-S16. Overlaid deconvolved mass spectra for TF^{19+} 117

Figure B-S1. Representative emitter SEM images 122

Figure B-S2. Example of CID50 vs signal strength for partially denatured holomyoglobin^{9+} on a Waters Synapt G2-Si 125

Figure B-S3. Spatial map of CID50 shift for partially denatured myoglobin^{10+} as a function of emitter position. 126

Figure B-S4. Emitter position influence on leucine enkephalin..127

Figure B-S5. Representative mass spectra of leucine enkephalin 128

Figure B-S6. CID of leucine enkephalin...129

Figure B-S7 Diagram and CID breakdown curves on an Agilent 6545XT Q-TOF Mass Spectrometer...130

Figure B-S8. Summary of CID50 values in “close” (blue), “far” (green) and “below” nESI emitter positions (gray)..131

Figure B-S9. Images of the Agilent 6545XT Q-TOF Mass Spectrometer (a) and Waters Synapt G2-Si (b) nESI source designs with representative diagrams............................132

Figure B-S10. Representative native mass spectra of BSA 133

Figure B-S11. Representative mass spectra of NIST mAb 134

Figure B-S12. Average of quintuplicate CIU fingerprints taken at each nESI emitter position on 3 separate days 135

Figure B-S13. Average difference of CIU fingerprints for quintuplicates taken at each nESI emitter position on 3 separate days 135

Figure B-S14. CIU50 fits of the averages of the quintuplicate data 136

Figure B-S15. RMSD (a) and CIU50 analysis (b) for native charge states of BSA with the exclusion of the high RMSD replicate 137

List of Tables

Table Page Number

Table IV-1. Enthalpy, entropy, Gibbs Free Energy, and Temperature determined by IonSPA....98

Table A-S1**.** Activation enthalpies and entropies for lipid head group CID. 114

Table B-S1: Summary of Settings and Positions. 118

Table B-S2. CIUSuite2 Processing Parameters. 123

I. INTRODUCTION

Mass spectrometry is an extremely useful tool for analysis of intact biochemical samples, and nano-electrospray-ion mobility-mass spectrometry (nESI-IM-MS) is well poised to manage many difficult to characterize biological samples due to its low sample needs, extreme sensitivity, specificity, and speed.[1–11] Analysis by nESI-IM-MS typically requires 10-50 microliters or less of 1-10 micromolar protein, data collection can typically be completed in minutes, and mass accuracy can be as good as a few ppm. Ions can be isolated or separated by m/z and/or ion mobility to allow analysis of a single m/z species of ion mobility conformer family (i.e., set of related conformers with similar collision cross section). The capabilities of nESI-IM-MS can be expanded by including a collisional activation step, typically prior to ion mobility separation, where internal energy is deliberately deposited into proteins from collisions between the ion and a buffer gas to dissociate or unfold (Collision Induced Dissociation (CID) or Collision Induced Unfolding (CIU)). CIU can be used to generate a CIU fingerprint, a representation of the unfolding of protein’s collision cross section (CCS) as a function of nominal voltage (energy), which, like a spectroscopic fingerprint, can be highly unique to that protein.[7,12] Mass spectrometry is regularly used directly and in combination with other biophysical and computational techniques to infer biomolecular structure beyond mass assignment.[13–21] Protein unfolding and dissociation are incredibly useful tools in mass spectrometry for studying fragmentation patterns,[1,22–30] complex and binding partner identification,[31] subtle structure differentiation,[32,33] and protein classification.[34,35] However, a major challenge in the field is to correlate the results of native mass spectrometry to solution phase structure, function, and behavior.[36] In this introduction, I describe in detail the nature of this challenge, the context of previous quantitation of energetics, and briefly outline my dissertation work.

One challenge in interpreting nESI-CIU/D-IM-MS data, especially quantitatively, in terms of solution phase structure, is that mass spectrometry data are collected in a very different environment than in living organisms.[14] Many biophysical studies use and leverage techniques to determine biological structural information that necessitate data collection in different from life environments. These techniques include x-ray crystallography, in which structures are destabilized from solution to cause crystallization (necessarily leaving more solution-stable species behind); cryo-EM, which requires a protein to be cryogenically frozen and stationary; atomic force microscopy (AFM)[37] and optical tweezers, which tether and apply mechanical forces to proteins;[38] and protein NMR. Like these biophysical techniques, nESI-IM-MS occurs in an environment very different from the cell, but can still provide valuable insights on protein structure and behavior. Some approaches to this problem have focused on using nESI-IM-MS, primarily or exclusively, as a measurement tool for probing solution phase experiments.[9,39–42]

To approach these problems a strong understanding of the limitations of each technique is valuable. For example, in x-ray crystallography, because most often the protein is in a single conformation, the relative position of the atoms and amino acids can be determined with high resolution. Consequently, x-ray crystallography is not ideal for studying dynamics and kinetics of disordered regions or proteins, but can be a powerful technique to study folded proteins or as a starting point for further study using orthogonal techniques such as molecular dynamics simulations.[43–45] Cryo-EM is limited by beam induced motion of analytes, can lead to sample degradation, requires averaging of many similarly oriented structures, and is limited to larger structures (typically > 100 kDa).[46] NMR typically a maximum size limit of 30 kDa and requires a protein be soluble, though some techniques are pushing past those boundaries.[47,48] All of these techniques have been used to generate relevant biological structure information, but an understanding of each technique’s specific limitations informs decisions on experimental approaches for a given problem and inferences on protein structure and behavior from the results. To take full advantage of mass spectrometry then, it is useful to develop a strong understanding of the fundamentals underlying transfer to the gas phase and subsequent gas phase behavior.

Prior studies have explored gas phase fundamentals extensively. From these works, it is understood that transfer to the gas phase using nESI can kinetically trap biomolecules and their complexes in structures very closely resembling those in the condensed phase.[49–53] However, the ion can only remain kinetically trapped as long as it does not gain sufficient additional energy or have sufficient time to rearrange to a more energetically stable gas-phase conformation. The gas-phase free energy landscape factors influencing this new conformation include the dramatic (at least 18x) difference in dielectric permittivity in the gas phase as compared to water, the lack of solvent that causes a reduction in hydrophobic driving forces of protein folding, changes in gas phase basicity,[54–57] and carrying a non-water-solvated charge.[58–61]

While nESI-CIU/D-IM-MS techniques can quickly generate a wealth of information, some of that information does not yet inform structure assignments, including fragments not assigned,[62,63] and the rate of change in CCS as a function of voltage (shape or "slope" of a CIU transition) is generally not considered. To interpret and synthesize the entirety of the information generated using these techniques will require further careful experimentation and theoretical developments. Furthermore, development of a greater understanding of the underlying mechanisms of structural disruption techniques will aid in both quantitation and interpretation of these gas phase measurements. By developing a stronger understanding of the underlying mechanisms of collisional activation in native mass spectrometry, we hope data can be more intuitively and confidently interpreted, artefacts more easily identified,[55,57,64] and experiments and instruments designed for answering novel research questions with novel techniques. Ideally, one day CIU fingerprints might be interpreted in terms of biomolecular structure, especially those recalcitrant to conventional structural techniques, in a way similar to force-extension curves in AFM pulling and optical tweezers experiments, but with the much higher throughput, specificity, and speed available in IM-MS.

Quantitative energetics by mass spectrometry

A major challenge in native mass spectrometry, and modern CIU/D in particular, has been to define the energy axis to allow for comparison to external standards, comparison between laboratories, and comparison over time. In CIU , the CCS axis is well standardized and calibrated,[65–68] but the energy axis is neither calibrated nor standardized. Some attempts at calibration between techniques have been performed,[69,70] in some cases internal energy has been considered,[71–79] and other techniques do utilize energetic calibration standards (thermometer ions).[80–85] Most often these values are reported as the voltage used in the collision cell to generate 50 percent dissociation (CIU50, CID50, SID50),[86–88] an instrument specific parameter, or this voltage multiplied by the charge of the ion.[69,89]

CIU/D50 values measured on different instruments for the same dissociation reaction can differ significantly, especially with the development of new collisional activation instrumentation such as the Agilent's in-source CIU cell.[90] Additionally, inter-instrument reproducibility of collisional activation techniques remains largely uncharacterized, although inter-lab and inter-user studies suggest the potential for high inter-lab reproducibility on the same instrument.[90] A potential approach comparing the results from activation experiments in different instruments, between laboratories, and over time is through the use of internal energy and determination of thermodynamic barriers. Thermodynamic barrier parameters, by definition, remain the same for the same reaction in any instrument cell and can offer insight into transition states and mechanisms of reactions, which in turn can allow for inferences about reactant and product structures. One can imagine being able determine the area of an interface in a protein-protein complex, confidently differentiate between specific and non-specific binding of ligands, determine the interface area of a particular folding domain in a protein, and/or aid in determining structural differences between similar protein structures (such as originator antibody drugs and biosimilars). Comparing CIUD50 values between instruments and labs is increasingly important and increasingly challenging due to diverging instrument designs, the potential for long term drift in these techniques, and the lack of clear procedures in place for standardizing and calibrating native mass spectrometry activation in modern commercially available instruments.

There is a long history of thermodynamics, energetics, and kinetics work in mass spectrometry. However, the currently available strategies for taking gas phase thermodynamic measurements are limited to smaller molecules[80,91–98] and/or specialized instrument setups.[72,99] These techniques also typically require extensive ab initio and RRKM modeling, which is challenging to scale up as protein analytes studied by mass spectrometry increase in size. Consequently these techniques can be exceedingly difficult or impractical to apply to CIU and CID in modern commercially available instruments.

At present, uncertainty over the structural changes proteins undergo and their relative energetic barriers in the gas phase can lead to uncertainty in assigning gas-phase observations to solution phase structures and dynamics.[14] As an example, the possibility of misassignment of a gas-phase artefact to a significant and biophysically relevant structure increases when the gas-phase dynamics and free-energy landscape underlying activation induced structural changes in mass spectrometric measurements are not considered.[55,100,101] Quantitating dissociation and unfolding based on internal energy, as has been previously performed with other activation techniques in mass spectrometry, could solve these challenges as long as the method for doing so is sufficiently flexible to many instrument designs and analytes, sufficiently computationally inexpensive to apply, and sufficiently accurate in comparison to previously determined thermodynamic barriers for gas-phase protein dissociation.

In this dissertation I describe my contributions to developing a stronger mechanistic understanding of the physical principles underlying modern native ion mobility mass spectrometry for the purpose of developing a method able to quantitate the energy involved in gas-phase dissociation in modern, commercially available collision cells. A "fundamentals-forward" approach has already been shown to have considerable benefits including 1) identification of gas-phase artefacts or confirmation of their absence,[55,57,64] 2) more facile structural interpretation available from the standardization of CCS in TWIMS[65,66,68] and an analytical and computational assessment of gas-phase compaction,[100] and 3) experimental design for desired reaction products.[102] In this dissertation I describe in detail my research in applying and expanding a model for determining quantitative gas-phase protein ion thermodynamic barriers by careful assessment of reproducibility and repeatability of nESI-CIU/D-IM-MS measurements, theoretical considerations of ion-gas particle collisions and their impact on protein internal energy, and consideration of the physics of other portions of ion trajectories through mass spectrometers.

History of mass spectrometry and native mass spectrometry

For over a century mass spectrometry has been applied across scientific disciplines. It has undergone many transformations since its initial development, aiding in its application to a wide variety of problems. In some of its most recognizable modern applications, mass spectrometry is coupled to a separation technique, such as gas or liquid chromatography (GC/MS or LC/MS) and used for compound identification, structural characterization, and quantitation in a wide variety of fields from earth and planetary sciences to synthetic chemistry, pharmaceutical development, and many other applications.

In addition to developments in orthogonally coupled techniques, ion optics, which steer the ions through mass spectrometers, and mass analyzers, which separate ions by mass in space and or time for detection, within mass spectrometers themselves have undergone many transformations over the technique's lifetime. Mass spectrometers can have a range of mass analyzers including those from time-of-flight (TOF),[103–105] in which ions are accelerated through a long, high vacuum region to determine their mass-to-charge ratio, to Fourier-Transform- Ion Cyclotron Resonance (FT-ICR) mass spectrometers,[106–109] which are used to determine mass-to-charge ratios by measuring their cyclotron frequencies within an external magnetic field. These mass analyzers and detection methods alone measure the mass-to-charge ratio of an intact or pre-fragmented analytes to determine information about their structure. However, current analysis in mass spectrometry is not limited to simple measurement of sample masses. Instead, there are many mass spectrometry coupled techniques which add internal energy to ions in the gas phase to generate product ion patterns that can be used to determine the structure of small molecules or peptides,[22,110,111] dissociate non-covalent complexes,[3] perform ion reactions,[102,112–114] or partially unfold native-like protein structures.[7,12,36]

Innovations that enable these experiments include collision-induced dissociation (whether in the trap of an FT/ICR, inside a multipole trap,[23,115–117] or other variants), electron capture/transfer dissociation,[11,118–122] nozzle-skimmer dissociation in the ion source region,[123–126] surface induced dissociation,[71] and blackbody infrared radiative dissociation.[72] To enable analysis and fragmentation of large ions, such as proteins, nucleic acids, large polymers, and even intact viral capsids, innovations in ionization and steering have been highly effective[2,127,127] to determine thermodynamic barriers for the dissociation of protein complexes,[58,128] identification of protein structure modifications,[129] and small structural differences.[130]

While, in its initial forms, mass spectrometry was limited to the characterization of small to moderate sized ions, the discovery of electrospray ionization (ESI) as an ionization method in mass spectrometry tremendously increased the size of ions that could be transferred to the gas-phase intact.[131] Since the development of ESI, instrumentation development has increasingly supported the analysis of larger biological samples by mass spectrometry.[18,20,21,36] To date, intact biomolecular complexes as large as ~18 MDa have been characterized using ESI, and no upper mass limit for this ionization technique has been established.

nano-electrospray ionization (nESI)

In 1980s, electrospray ionization (ESI) was developed[131,132] based on earlier electrospray-bath gas-free-jet experiments.[133] In these experiments Fenn and Yamashita measured ion clusters and characterized the influences of voltage, ion currents, and cluster distribution on each other. Fenn subsequently received the 2002 Nobel Prize in chemistry for showing that ESI could be used to ionize intact proteins ("flying elephants")[134] from solution directly into the gas phase without the need for digestion into much smaller peptides. Subsequently this method of ionization was applied to analytes eluted from liquid chromatography, which fortuitously can be operated at flow rates well-suited toward analyte detection with mass spectrometry, and to intact protein analytes directly introduced from "static" capillary sources without LC.[129,135,136] Unlike many other ionization techniques, ESI can transfer large proteins and protein complexes to the gas phase as ions and is able to do so softly, i.e., with minimal disruption of the delicate non-covalent interactions structures found in folded native-like proteins and protein complexes.[49,50] Nano-electrospray ionization (nESI) was initially developed in the 1990s as "micro-electrospray", using gold-coated capillary emitters with a 1-3 micrometer opening.[137] The development of nESI has enabled the study of proteins and protein complexes under even softer (less disruptive) conditions in part by requiring lower spray potentials.

ESI generates micrometer-scale droplets, whereas nESI generates nanometer-scale droplets from micrometer scale openings. nESI has much lower sample needs and is a softer technique (preserves more delicate structure) than ESI. In nESI, droplets with diameters of many tens to hundreds of nanometers are formed by applying an electric potential between solution contained in an emitter (via a gold coating on the outside of the capillary or a platinum wire in direct contact with the solution) and the entrance to a mass spectrometer without the aid of a pump (static nESI) or with the aid of a syringe pump to generate charged droplets. There are several reasons for nESI's "softness" including evaporative cooling as water evaporates from solvent droplets keeping proteins from heating considerably, the decreased potential required to form charged droplets, and the increasing strength of noncovalent interactions as the solvent evaporates. Several exquisite studies have demonstrated that proteins can retain both secondary and higher-order structure as well as function upon transfer to the gas phase,[49,50] and a plethora of other experimental and computational studies provide additional evidence of structure retention.[3–7,138,139] Since its initial development, nESI has enabled characterization of increasingly larger complexes, such as intact ribosomes, viral capsids, and large membrane protein assemblies with adducted native lipids.[15,140–144] nESI's softness as an ionization method, e.g. its ability to retain non-covalent structure, and its low sample needs these make nESI a widely appealing and commonly used ionization method for native (ion mobility) mass spectrometry analyses.

Many studies have investigated the principles and mechanisms underlying (n)ESI and informed its development. Previous studies have focused both on modeling evaporation and fission of droplets in electrospray ionization[51,145–149] and on the mechanism of charge deposition[52,54,150–155] using both theoretical and empirical methods.[137,148,149,156–159] As water from a droplet evaporates the charges on the surface move closer together. At the Rayleigh limit the repulsion from these charges is too great for the droplet to remain stable. At this point the droplet undergoes a process called Rayleigh fission, where a Taylor cone, or elongated point on the surface of the droplet, is formed and cone small charged droplets are pinched off. The analyte may be contained in the initial droplet ("parent" droplet), or the resulting droplet ("progeny droplets"). When the analyte remains contained in the parent droplet or any larger droplet, more evaporation is needed for this analyte to become a 'bare' ion, detectable by mass spectrometry as its own mass.

The detailed mechanisms by which charges are deposited onto an analyte have been described by three conceptual models. These are the Ion Evaporation Model (IEM),[160–162] applicable to small analytes; the Charged Residue Model (CRM),[160,163,164] which dominates in the case of large compact ions; and the Chain Ejection Model (CEM),[163,165] which applies to large analytes in non-native conditions. In the IEM a charged analyte evaporates from the surface of droplet, while in the CRM a droplet undergoes cycles of evaporation and fission and the final shell of water surrounding the analyte transfers charges onto the (still folded) protein as it evaporates. In the CEM, one or more longer more tendril-like portions of the (unfolded) analyte extend beyond the boundaries of the droplet; to remain well distributed along available space some charges remain on the portions of the analyte beyond the boundary of the droplet. Each model likely contributes to the entire picture of charge deposition in ionization, and the model which most accurately describes the behavior differs depending on experimental conditions.

If other nonvolatile components are contained in the droplet, such as sodium and potassium ions, the analyte and non-volatile components can bond as they occupy a decreasing volume of solvent. This is one cause of non-specific adduction, a noncovalent interaction that is observed by mass spectrometry but does not reflect the analyte's typical structure or binding partner. Non-specific adduction is a major challenge in native-mass spectrometry.[166–169] Salts present in solution adduct to the desired analyte confounding inferences of solution phase structure and behavior of analytes. These adductions can cause structural disruption, obscure accurate masses of analyte, or even, in cases of extensive adduction for large ions, obfuscate analyte identification.[170–172] Non-specific adduction poses another challenge when nESI is used to interrogate protein-protein or protein-ligand complexes. Similarly to salt adduction, the results may be influenced by non-specific or artefactual binding of other solution components such as ligands, monomers, or lipids to the analyte. These challenges are often mitigated in three ways: first, through the use of solutions made of volatile salts (such as ammonium acetate), which typically evaporate rather than adduct to analytes in the gas-phase; second, through the use of deliberately more activating (less soft) ionization conditions, which may destabilize salt adductions; and, third, through the use of smaller (submicron-diameter) emitters, which produce smaller initial droplets.

Typical nESI emitters are 1-3 micrometers in internal diameter. Recently several studies have been published with the purpose of communicating strategies to make nESI emitters with less than one micrometer i.d..[166,168] The use of these submicron emitters reduces the number of droplets with 2 or more components present in the same droplet at a given concentration. This can allow for a much more confident assessment of specific binding of proteins and ligands at higher concentrations than for larger, micrometer emitters. Submicron emitters can also greatly reduce nonspecific adduction, because the initial droplets inherently contain fewer salts and other co-solutes than those generated with larger emitters. This can enable acquisition of mass spectra of proteins electrosprayed out of widely-used biological buffers containing high concentrations of salts (e.g., HEPES, Tris, and phosphate buffers) under some conditions.[173] This expands the range of proteins mass spectrometry can investigate to include those which are unstable in volatile aqueous solutions and buffers.

Reproducibility

nESI is a powerful platform for preparation of native-like protein ions and has been used to prepare intact, native, and denatured biological ions for study by mass spectrometry with great success.[49,50,174,175] Many aspects of native mass spectrometry are highly reproducible, and considerable effort has been dedicated to ensuring this. For unactivated ions, charge state distributions consistently overlap when using "soft" ionization conditions,[52] collision cross sections are highly consistent across instruments,[65,67] and solvent identity and pH impact samples reproducibly.[145,154,163,176,177] For activated ions, the same products are typically generated for dissociation of a given analyte, with product ratios varying on different instruments or under different conditions.[84] In some cases, drastically different activation time-scales, such as those between CID and SID, result in alternate dissociation pathways.[178,179] Collision induced unfolding and surface induced unfolding are sufficiently reproducible to identify scaling between the two techniques[69,70] and perform triplicate measurements with very low deviations. For CIU/SIU the qualitative features (CCS value visited, shapes of the transitions and features) are recognizably different between different proteins and visibly share features between similar proteins.[13,33,35]

However, nESI, and its macroscale counterpart ESI, can also display variable results and variable stability.[75,126,177,180–183] Some of these have previously been attributed rather nebulously to user "touch" (e.g., measuring different extents of ligand binding despite following “identical” experimental protocols), emitter position, and emitter-instrument entrance angle.[180,184] During my training in this PhD, the observed variability has been anecdotally, and sometimes humorously, attributed to humidity, day of the week, mood of the user, nESI emitter opening, previous capillary voltages, the nESI user, how close a deadline is, placement of a platinum wire within an emitter, quality of electrical contact, length of platinum wire, potentials deeper into the instrument, temperature, weather, age of buffer solutions, quality of the emitter, amount of salts present, and empirically attributed to emitter position on some nESI sources. This is of value to note as nESI techniques are passed on during mentorship and training during academic experiences (undergraduate, graduate, and postdoctoral research), and in that process information and methods which are not necessarily published or quantitatively validated are also passed on. In some cases a single user or a single lab or lineage can achieve highly reproducible results from nESI-(IM)-MS experiments,[185,186] while in other cases results may vary.[180] Some studies have aimed to characterize reproducibility,[90] but there is much left to understand in both the empirical causes of "good" nESI spray and the physical models needed to describe and predict "good" and "bad" nESI.

nESI’s sensitivity to parameters and ability to maintain native-like structure on many different instrument source designs and across many different samples and solvents can be valuable and to maintain high reproducibility it is important to characterize and report this as low reproducibility and repeatability pose a challenge to both quantitation and comparison. Some evidence suggests that ions nESI may impart sufficient internal energy to impact energetic quantitation,[181,182] but energetic calibration standards for energetics in protein dissociation and unfolding and nESI “softness” are not routinely employed. Other calibration standards such as those for mass calibration, collision cross section and ion mobility calibration,[65,67] are regularly used. Though thermometer ions have been used as an energetic calibrant,[81,85,97,187] they are not typically employed in studies of protein unfolding and dissociation to calibrate energy deposition. A further discussion on the impacts of reproducibility and repeatability of nESI as applied to structural disruption of proteins is presented in Chapter III.

Activation of Proteins and Peptides

Thermodynamic barrier values for protein and peptide dissociation in gas phase have been determined for dissociation events of proteins and peptides using BIRD, GIBMS, and SID.[58,71,79,128,178,188–190] These efforts have resulted in a small catalog of thermodynamic measurements on a number of small molecules, clusters, petides, and small to moderately sized proteins, which can be used in benchmarking new techniques, as well as in their original purposes. These efforts have also resulted in models representing physical understandings of internal energy deposition and subsequent dissociation (or decomposition) in the gas-phase. In general these models operate based on two distinct steps: 1) activation or internal energy deposition to generate an ion with high internal energy and 2) a unimolecular dissociation (decomposition) event.[79] The extent of dissociation can be readily measured, but clarity on the internal energy deposition from multiple subsequent collisions and the resulting statistics is needed to evaluate energetic barriers in modern, moderate pressure, commercially available collision cells.

One model proposed for describing this collisional activation is the Impulsive Collision Model (ICM).[191] In this model the gas particle has an inelastic collision with a small subdivided portion of the ion referred to as the pseudo-atom. A small amount of energy from the collision is transferred into kinetic energy of the pseudo-atom, which is in turn internal energy of the overall protein. This model was tuned to collisional activation of peptides and found a pseudo-atom mass of 32 Da using argon as a collision partner. On modern commercially available instruments, due to their higher pressure operation generating many collisions which both heat and cool any analyte, so the ICM could not be applied accurately without modification to include analyte collisional cooling.

In BIRD experiments a massive copper “jacket” surrounding the ion cell of the instrument is heated to the desired analysis temperature, and the ions are rapidly equilibrated with that temperature through exchange of blackbody photons between the ions and the copper jacket. The dissociation of the ions is measured at multiple temperatures to determine the rate of decay and in turn the thermodynamic barrier information. BIRD has been used a heating method for taking accurate and precise thermochemical measurements of native-like ions as large as ubiquitin. Price and coworkers justify their work theoretically and experimentally,[72] suggesting BIRD values as the gold-standard of quantitative thermodynamic barrier information. While values from BIRD are considered the best available from gas-phase dissociation of proteins, the experiment is time intensive, taking days to weeks to collect the data to determine a single value and requires the use of an FT-ICR instrument fitted with a copper jacket. To our knowledge, both the BIRD instrument originally developed in the Williams group and a latter one developed by the Klassen group have been decommissioned, and no other BIRD-capable instruments have been recently reported in the literature, thus BIRD-capable instruments are no longer available at present anywhere in the world.

In guided ion beam mass spectrometry (GIBMS), a beam of ions is collided with a beam of neutral gas in a single collision and the reaction cross section is determined.[79,192–194] This reaction cross section is determined by converting the raw ion intensities based on the pressure and length of the collision cell. The cross section is a function of the excitation energy, i.e., center-of-mass frame collision, E. This information is obtained through careful consideration of observables such as scattering angle from the beam and lab-frame kinetic energies before and after the collision. This technique typically requires both specialized equipment (currently only in use in the Armentrout group) and a sufficiently high vacuum to generate products of a single high energy collision. These requires make this technique challenging to employ on commercially available mass spectrometers[192] and challenging to scale to intact and native proteins and protein complexes.

SID, which is much more widely available now as a vendor-supported modification to commercial MS instrumentation,[195,196] was applied alongside rigorous modeling to describe the kinetics of gas phase fragmentation of leucine enkephalin.[178] In this study a model was identified in advance for the reaction pathways of leucine enkephalin, and experimental data were fit to determine the activation energy (Ea), the Arrhenius prefactor (A), and the entropy barrier to dissociation for each pathway.

Ion Mobility

In modern commercially available instruments, native mass spectrometry is often coupled with ion mobility mass spectrometry (nIM-MS or nESI-IM-MS). Initially and today, drift tube ion mobility (DTIMS) were coupled to mass spectrometers.[197,198] In DTIMS, ions are pulled through a tube filled with neutral buffer gas at a moderate to "high" pressure (i.e., a few mbar) using an potential difference. Ions with a large rotationally averaged surface area (collision cross section, CCS), i.e., those with lower charge states or a more "extended" structure, travel more slowly than those with smaller CCS. This is similar to how a crumped piece of paper, a unfolded sheet of paper, and a paper airplane drop to the earth at different speeds though the same mass and acted upon by the same gravity. In low-field DTIMS, the time an ion takes to travel through the cell depends directly on its collision cross section charge state through the Mason-Schamp equation.

To increase the separation achievable over a relatively short length ion mobility cell, "traveling-wave" ion mobility cells were developed; by applying a varying potential across electrodes over time to move the analyte ions through the tube of buffer gas, similar resolution to drift tube ion mobility can be achieved using a significantly shorter tube.[199,200] In TWIMS, unlike DTIMS, the time the ion takes to travel through the cell is dependent on more factors and lacks a closed-form expression in terms of collision cross section. Consequently, determining CCS using TWIMS requires careful calibration. Multiple calibration approached have been proposed with a set of well-behaved proteins with well-defined CCS values,[65] theoretical calibration based on mathematical insights and computational modeling,[68,201] and an empirical calibration using polyalanines.[66]

Modeling efforts have provided two additional important insights into IMS. First, modeling of the TWIMS cell in both SIMION, a program which models ion trajectories through user-input ion optics, to study ion trajectories and mathematically has provided insights into TWIMS mechanics. These insights have been applied to generate a mathematical CCS calibration.[66] Additional mechanistic study was dedicated to ensuring the absence of ion heating or structural disruption in TWIMS cells,[85] which were theorized to arise due to the higher electric potentials constituting the traveling wave as compared to the electric potentials in the drift cell.

In biological structure determination in addition to accurate measurement of CCS, the relationship between measured CCS and native structure is important. Extensive study into the gas-phase effects referred to as gas phase compaction or collapse has recently permitted direct quantitative comparison of ion mobility data to proposed solution phase structures where previously only relative comparisons were accessible.[100,202]

Collision Induced Unfolding and Dissociation (CIU/D)

In characterization and identification of small biological molecules a fragmentation pattern can differentiate between two very similar molecules and is routinely used for complete determination of ion structure.[203,204] In modern applications many strategies for fragmentation can be employed including electron capture dissociation,[118–120,185] where an electron is added to an ion to generate an unstable radical which then dissociates to a more stable form; surface induced dissociation,[28,71,178,205] in which an analyte is collided at high kinetic energy with a stationary surface rapidly increasing its internal energy; ultraviolet photodissociation (UVPD),[1,206,207] where ions are excited by an ultraviolet laser to increase their internal energy and cause dissociation; or collision induced dissociation (CID)[29,56,191,208–211] where an ion has many collisions with a buffer gas (relatively) slowly increasing its internal energy. These techniques have all generated many structural insights about biological samples including oxidation of heme in proteins,[24,212] sequence identification[111,125,213,214] (and recently attempts at assigning internal fragment ions),[62,63] ligand binding partners,[31,34,180,207,215–220] and protein complexes quaternary structure among others.[3,25,221,222]

Coupling these structural disruption techniques with ion mobility, in which ions are separated by shape/charge, gives rise to a common technique in IM-MS for studying the structure of proteins and protein complexes: collision induced unfolding (CIU).[12,14] In CIU, like CID, protein ions are heated by many energetic inelastic collisions between the ion and a neutral collision gas. Proteins activated in this way often unfold (collision induced unfolding (CIU)) due to breaking of non-covalent bonds and, at higher energies, may dissociate (collision induced dissociation (CID)) as covalent bonds are broken.

Dissociation and unfolding in this method of activation have been proposed to proceed by the "mobile proton model", where a proton moves from one basic site on the protein to another under activating conditions. This can lead to proton-assisted dissociation of covalent bonds in CID or of non-covalent bond in CIU.[26,56,60,223,224]

One strategy for representing and analyzing these data is as a "CIU fingerprint". In this representation a temperature plot of the CCS or drift time (y-axis) over collision energy or voltage (x-axis) is plotted.[12,86] Typically a protein has an initial, well-defined, native-like initial cross section which expands to multiple subsequent well-defined distributions, though in some cases compaction or multiple concurrent stable states are observed. CIU fingerprints for significantly different proteins can look significantly different, visiting a different number of states, remaining in those states through different levels of energy, and different shapes of states. For subtly different proteins the CIU fingerprints often look qualitatively similar with distinct differences in some features or transition energies.[32–35] Using CIU in nIM-MS, a number of new methods have been developed to utilize mass spectrometry as a biochemical and biophysical tool to probe structural differences in secondary and tertiary structure. Recently CIU has been used in wide variety of protein structure applications.[12,32,33,35,207,225]

Historically, structural disruption techniques have been used in solution to infer structural patterns of behavior from the shape of transitions between initial, intermediate (if stable enough to be observed), and unfolded structures.[226] In principle, the same kinds of inferences should be possible in the gas phase with a strong understanding of the mechanisms relating gas-phase behavior to structure. Where unfolding studies in solution typically observe proteins visiting 0 or 1 intermediate (1-2 transitions), CIU often observes 3 or more transitions for sufficiently large protein ions. The number of transitions has been correlated with the number of domains in a variety of protein ions.[227] And, like in the solution phase unfolding experiments, the slope of a decay curve representing the transition may be able to inform structural assessments of stability, cooperativity, and potentially local structure assignments. In order to identify the slopes and midpoints of decay curves associated with gas phase structural transitions in an absolute sense (i.e., in terms of internal energy) it is necessary to determine an instrument-independent quantity that can be associated with the x-axis rather than with respect to an instrument-specific parameter (i.e., the nominal voltage entered into the instrument control software). Currently the denaturant axis is typically defined as the nominal voltage of the collision cell in a given instrument or, alternatively, as the nominal voltage multiplied by the charge (i.e., the approximate initial lab-frame kinetic energy of the ion as it enters the collision region of the instrument). Because instrument settings and instrument designs can differ significantly between experiments, between models, and between labs, the nominal voltages reported may not have any or an immediately clear relation to each other quantitatively or qualitatively.

Given the frequency with which users vary parameters and different labs use one of many commercially available instrument designs or in some cases homebuilt instruments, an assessment of the microscopic physical characteristics of the ion, such as internal energy, can be substituted for macroscopic instrument parameters, such as acceleration voltage, to determine thermodynamic barriers. Prior work from our lab pursued this same goal with considerable success for the Waters Synapt G2-Si using a simple collision model based on a 90% transfer of lab-frame kinetic energy into internal modes of the ion.[186,228]

Despite the gap in quantitation of the energy axis in CIU, significant effort has been applied to understanding the implications of protein and peptide size in the gas phase and their increasing CCS upon activation.[65–67,69,100,229–232] To generate a quantitative understanding of the energy axis, we can draw on this long history of modeling of ion behavior as a strategy for instrument and experimental design;[69] quantitative understanding of other methods of activation[28,71,72,79,85,191,233,234] and deepening mechanistic understanding of gas phase processes;[26,57,85,91,224,233,235–240] and inferring relevant solution and biochemical behavior[6,32,51,216,241,242] in native mass spectrometry.

In this dissertation…

In Chapter II, I empirically characterize the binding energies of non-specific adduction of lipid head group analogues using a moderate complexity model (proto-IonSPA). Work in this chapter was published in the *International Journal of Mass Spectrometry* and co-authored with Micah Donor, Jesse Wilson, and James Prell. In Chapter III I use an analytical approach to characterize the repeatability and reproducibility of nESI-CIU and nESI-CID as a function of nESI emitter position in relation to the entrance to the instrument. Material in this chapter was published in the *Journal of the American Society of Mass Spectrometry* and coauthored by Elizabeth Resendiz, Austin Green, Kenneth Newton, Ruwan Kurulugama, and James Prell. In Chapter IV I describe the benchmarking and validation of a model (IonSPA) simulating the physics of activation due to collisional activation, where I use the previous reproducibility results to inform the uncertainty of these measurements. A manuscript based on this work is in preparation and will be coauthored by Austin Green, Kenneth Newton, Jody May, John McLean, Ruwan Kurulugama, and James Prell.

II. LIPID HEAD GROUP ADDUCTION TO SOLUBLE PROTEINS FOLLOWS GAS-PHASE BASICITY PREDICTIONS: DISSOCIATION BARRIERS AND CHARGE ABSTRACTION

This chapter includes previously published co-authored material with co-authors Micah Donor, Jesse Wilson, and James Prell. Data collection, data analysis, and project conceptualization were performed by all parties. Replicate data collection and analysis were performed by Samantha Shepherd. A first draft of this manuscript was written by Micah Donor and Jesse Wilson, subsequent draft were rewritten to include new data and framing by Samantha Shepherd and James Prell resulting in the final published manuscript.

Abstract

Native mass spectrometry analysis of membrane proteins has yielded many useful insights in recent years with respect to membrane protein-lipid interactions, including identifying specific interactions and even measuring binding affinities based on observed abundances of lipid-bound ions after collision-induced dissociation (CID). However, the behavior of non-covalent complexes subjected to extensive CID can in principle be affected by numerous factors related to gas-phase chemistry, including gas-phase basicity (GB) and acidity, shared-proton bonds, and other factors. A recent report from our group showed that common lipids span a wide range of GB values. Notably, phosphatidylcholine (PC) and sphingomyelin lipids are more basic than arginine, suggesting they may strip charge upon dissociation in positive ion mode, while phosphoserine lipids are slightly less basic than arginine and may form especially strong shared-proton bonds. Here, we use CID to probe the strength of non-specific gas-phase interactions between lipid head groups and several *soluble* proteins, used to deliberately avoid possible

physiological protein-lipid interactions. The strengths of the protein-head group interactions follow the trend predicted based solely on lipid and amino acid GBs: phosphoserine (PS) head group forms the strongest bonds with these proteins and out-competes the other head groups studied, while glycerophosphocholine (GPC) head groups form the weakest interactions and dissociate carrying away a positive charge. These results indicate that gas-phase thermochemistry can play an important role in determining which head groups remain bound to protein ions with native-like structures and charge states in positive ion mode upon extensive collisional activation.

Introduction

Native mass spectrometry can be a powerful tool in determining the composition, stoichiometry, and structure of biochemical analytes, many of which can be challenging to accurately and precisely characterize using other techniques. As native mass spectrometry (MS) instrumentation and sample preparation methods have improved, a wider range of biochemical targets have come under investigation,[243,244] including native membrane protein-lipid and protein-drug interactions.[245–253] Many membrane proteins can be solubilized using local environments that mimic the lipid membrane, such as detergent micelles,[254–256] or lipoprotein Nanodiscs,[255,257,258] and are amenable to native electrospray ionization (ESI). [142,244] In parallel, many protein-drug complexes are stable to electrospray ionization, and their stoichiometry and structure can be probed by native ion mobility-mass spectrometry (IM-MS), Collision-Induced Unfolding, and other gas-phase methods. Seminal work from the Robinson, [248,250,256,259–261]Laganowsky,[216,217,262–265] Klassen,[31,266–268] and Ruotolo[219,269,270] groups and many others has demonstrated the power and utility of these approaches.

Ideally, the stoichiometry, binding sites, and apparent binding strengths of protein-lipid, protein-drug, and other biochemical interactions studied using native (IM-)MS are a direct reflection of the condensed phase. However, because the dielectric permittivity of the vacuum environment is much lower than in solution, and water molecules and other co-solutes that contribute to biomolecular structure and stability are largely absent in the biomolecular ions produced by electrospray ionization (ESI), care must be taken to ensure that the observed ions do not undergo unwanted changes in structure during the native (IM-)MS experiment.[100,101,271] Numerous experiments and computations have shown that biomolecular ions can become kinetically trapped (see Figure 1) in native-like conformations during ESI under carefully controlled instrumental conditions.[51–53,100,272,273] Typically, micron- or submicron-sized ESI emitters (nanoelectrospray ionization, “nESI”) and low-micromolar (or lower) concentrations of analytes and non-specific cosolutes (such as metal ions or other potential adducts) are used as well to limit condensation of unwanted adducts onto and evaporation-induced oligomerization of biomolecules during the ESI process.[274–278]

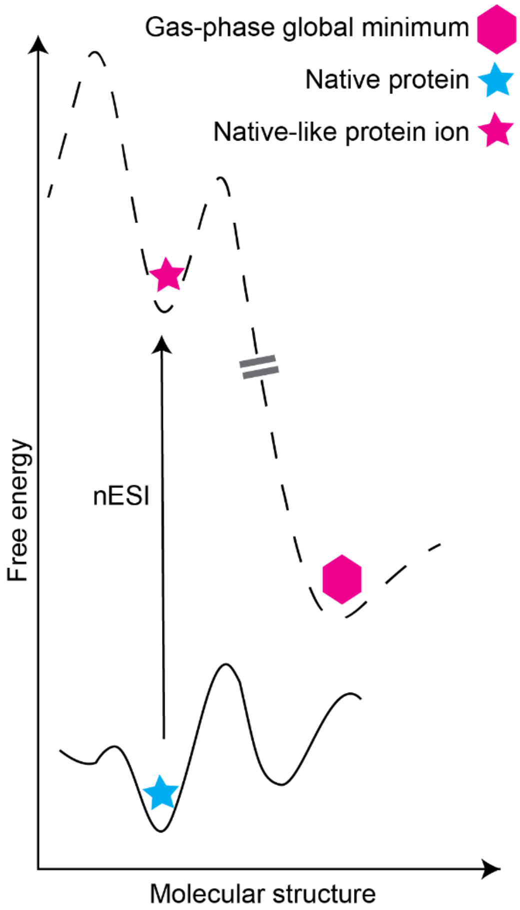
Gas-phase global minimum
Native protein
Native-like protein ion
Free energy
nESI
Molecular structure

Figure II-1. *Schematic potential energy surface for native protein-adduct complex in aqueous solution (bottom; blue star represents global minimum-energy structure) and after transfer to the gas phase environment using nESI, in which energy is imparted to desolvate the protein ion (top). Note that relative energy barrier heights for adduct migration, protein unfolding, and other processes can differ between the solution and gas phase due to the absence of water and other cosolutes in the latter environment. Double-dashed line indicates variety of possible pathways to the gas-phase global minimum structure (pink hexagon), which may differ substantially from the kinetically trapped native-like protein ion (pink star).*

In the past decade, several groups have demonstrated excellent agreement between binding behavior in solution and results inferred from native (IM-)MS experiments.[216,252,256,264,265,279] For example, Klassen's "Catch-and-Release" native MS experiments[266,267,280] have indicated similar ganglioside preferences of peripheral bacterial toxin proteins to those known from condensed-phase techniques. The Robinson and Laganowsky groups and others have also determined phospholipid binding preferences of both bacterial and human transmembrane proteins and found them to agree very well with condensed-phase results.[250,252,256,259,261,262,264,265,279,281–283] Laganowsky has developed instrumentation for studying protein-lipid interactions as a function of solution temperature and demonstrated that lipid binding thermodynamics inferred from abundances of gas-phase protein-lipid complex ions are in agreement with those determined in the condensed phase.[216,217,264]

Crucial to the accuracy of these types of experiments are the preservation of condensed-phase structures and interactions during the nanoESI process without introducing new, artifactual ones. Two ways in which these artifacts can in principle be introduced are: 1) adduction of non-specific cosolutes to the biomolecular ion during the nanoESI process due to droplet condensation ("non-specific adduction")[169] and 2) changes in the structure or location of a specific binding site due to heating and relaxation of the complex ion in the gas-phase environment, where the potential energy surface may be different from that in solution ("adduct migration"). Evidence for non-specific adduction is readily observed as formation of oligomers and complexes known to be absent in solution, often as a result of using large ESI emitters and/or high biomolecule concentrations that statistically place multiple analytes within each initial electrospray droplet.[274,276] This effect can even be exploited to displace metal cations from proteins during the nanoESI process in methods such as "buffer loading"[169] or to produce salt cluster ions for mass calibration.[284] Much less studied is the phenomenon of adduct migration, although much evidence supports the lability of charged species such as protons to migrate on the surface of native-like protein ions, which can result in unfolding and/or dissociation of the ions upon gas-phase activation.[22,60,223,285–288] Infrared photodissociation spectroscopy studies further indicate that protons can move from basic sites on organic ions that are favorable in solution to other basic sites that are more favorable in the gas phase during the ESI process.[54,223,289–291] Because hydrogen bonds, shared-proton bonds, and other polar interactions can have very different relative stabilities in the gas phase versus in solution,[54,292] thermochemical barriers for disruption of non-covalent interactions can be dramatically different in the aqueous and gas-phase environment as illustrated in Figure 1.[287] For example, hydrochloric acid is a much stronger acid in aqueous solution than phosphoric acid, but their relative acidities are reversed in the gas phase.[293] Similarly, carboxylic acid groups are poor bases in aqueous solution but relatively strong bases in the gas phase.[54,292]

The method most commonly used to dissociate unwanted adducts, such as detergent molecules, from protein-lipid complexes in native (IM-)MS studies, Collision-Induced Dissociation (CID), is a “slow heating” method.[294–296] Dissociation in CID occurs on the many-microsecond to millisecond timescale.[186,240] It is plausible that, under some experimental conditions, lipids initially bound at the surface of a membrane protein can undergo a change in binding geometry or migrate along the protein surface prior to complete dissociation. Whether these processes occur under a given set of experimental conditions inherently depends on the gas-phase potential energy surface for the protein-lipid interaction and the timescale of the dissociation process.

Here, we use a recently-demonstrated method for experimentally measuring gas-phase binding entropy and enthalpy barriers to determine gas-phase dissociation barrier thermochemistry of several common lipid head groups non-specifically bound to ions of soluble proteins in positive ion mode.[186] Relative gas-phase binding affinities to these protein ions are found to agree very well with expectations based on measured and computed gas-phase basicities of the lipid head groups.[57] This strategy is intended to circumvent ambiguities in interpretation that could arise from the presence of competing specific interactions and is used as a benchmark for evidence of non-specific lipid binding. Finally, we discuss implications of these results for identifying and determining the strength of physiologically relevant protein-lipid interactions using existing native (IM-)MS strategies.

Materials and Methods

Sample preparation. Glycerophosphorylcholine, phosphorylcholine, phosphorylethanolamine, glycerol 1-phosphate, phosphoserine, ubiquitin, lysozyme, and transferrin were purchased from Millipore Sigma (Saint Louis, MO, USA). Lyophilized proteins were reconstituted in ultrapure 18 MΩ cm water and buffer-exchanged into 200 mM ammonium acetate, pH 7-7.5. Lipid head groups were dissolved in 200 mM ammonium acetate, pH 7-7.5. For experiments with ubiquitin and lysozyme, protein and lipid head group solutions were combined such that the final concentrations of protein and head group were 10 μM and 100 μM, respectively, while for experiments with transferrin the final concentrations were 5 μM protein and either 500 μM head group or, for competitive binding experiments, 500 μM of each head group under investigation.

Native IM-MS and CID. All mass spectrometry experiments were performed in triplicate (transferrin experiments) or quadruplicate (all other experiments) on separate days in “Sensitivity” mode using a Synapt G2-S*i* (Waters Corp., Milford, MA, USA) with a nESI source. nESI emitters were pulled from 0.78 mm i.d. borosilicate capillaries to a final i.d. of ~1 μm using a Flaming-Brown P-97 micropipette puller (Sutter Instrument, Novato, CA, USA). Emitters were loaded with 3-5 μL of sample, and 0.7-1.1 kV was applied to a platinum wire in electrical contact with the solution to initiate electrospray. The source was held at ambient temperature, the sampling cone voltage was set to 25 V, and nitrogen, helium, and argon gas flow rates were 50, 100, and 5 mL/min, respectively. An ion mobility traveling wave velocity of 500 m/s was used for experiments with ubiquitin and lysozyme, a velocity of 400 m/s was used for experiments with transferrin, and a wave height of 20 V was used for all experiments. For CID experiments with ubiquitin and lysozyme, the singly-adducted state was isolated for a given charge state using a 32k quadrupole with the LM resolution set to 12. Dissociation was achieved by increasing the Trap CE in 1 V increments, beginning at the threshold for observable dissociation and continuing until the precursor was fully dissociated or significant covalent bond fragmentation was observed. For transferrin, due to the higher charge states present, there was insufficient resolution to completely isolate the singly-adducted state. Instead, an entire charge state was isolated with the LM resolution set to 4 and CID performed by increasing the Trap CE in 10 V increments from 10 V to 100 V. Additional mass spectra for transferrin were acquired without isolation at Trap CE values of 10, 50, 70, and 100 V.

Data analysis. CID data for lipid head group-bound ubiquitin and lysozyme were analyzed in a similar manner to that described in our previous publication,[186] (see also Supp. Info. for a brief description). Briefly, arrival time distributions for precursor and product ions were extracted using TwimExtract[297] and integrated in Igor Pro v. 6.3 (WaveMetrics, Portland, OR, USA).

For experiments with transferrin, native mass spectra were deconvolved using UniDec,[171] and the Gabor Transform method in iFAMS (for “Double FT” analysis),[298,299] to determine mass and charge state distributions as well as total lipid head group adduction. UniDec input parameters were: charge state range 10-25+, mass range 78-84 kDa, and peak full-width-at-half-maximum (fwhm) 3.0. Deconvolved mass spectra were analyzed further using Igor Pro v. 6.3 and iFAMS v. 5.3.[298,300]

Results and Discussion

By probing the energetics of non-specific lipid head group binding, a baseline for what might be expected in the case of lipid-protein interactions governed by gas-phase, as opposed to condensed-phase, chemistry can be determined. To do this, we employ our recently introduced method for determining activation energies for protein and protein complex CID to determine dissociation barrier thermochemistry of lipid head groups non-specifically adducted to soluble proteins.

Several lipid head groups representing common phospholipids were studied. Structures of phosphorylethanolamine (PE), sodium glycerol 1-phosphate (PG), phosphoserine (PS), phosphorylcholine (PC), and glycerophosphorylcholine (GPC) are shown in Figure 2. GPC was studied in addition to PC due to the prevalence of calcium as a contaminant in PC solutions; calcium adduction was found to decrease spectral quality and complicate analysis. Ubiquitin (Ubq, 8.6 kDa) and lysozyme (LZ, 14 kDa) were used as model soluble proteins with no known native phospholipid interactions. Native mass spectra of each protein with no head group present were acquired and are shown in Figure S1. The most abundant native-like charge state was chosen for subsequent CID experiments; 5+ for Ubq and 7+ for LZ. Additional solutions of each lipid head group with Ubq or LZ protein were prepared in 10:1 head group:protein molar ratios. Statistically, at these lipid head group concentrations, multiple lipid head groups are present in each electrospray droplet, resulting in evaporation-induced, non-specific adduction of one or more lipid head groups onto protein ions present in the same droplet. The singly-adducted state of each target ion complex was isolated and subsequently dissociated in the Trap using CID over a range of collision energies.

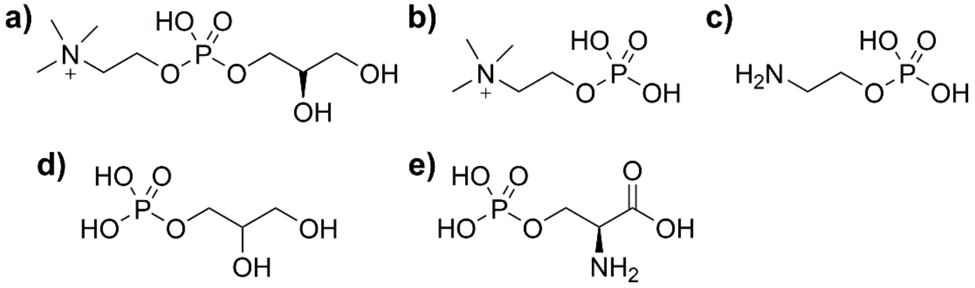

Figure II-2. *Structures of lipid head groups* ***(a)*** *glycerophosphorylcholine, GPC;* ***(b)*** *phosphorylcholine, PC;* ***(c)*** *phosphorylethanolamine, PE;* ***(d)*** *glycerol 1-phosphate, PG; and* ***(e)*** *phosphoserine, PS. Protonation states shown indicate those observed upon gas-phase dissociation from complexes with proteins in positive ion mode.*

Mass spectra of lipid head group binding. For Ubq, representative mass spectra for GPC, PS, PC, PE, and PG head groups, are shown in Figure 3. (A nESI spectrum of Ubq with no lipid head group present is shown in Figure S1 for comparison. Replicate data with lipid head groups are shown in Figures S2-S6, illustrating the level of reproducibility of the experiments on different days using different nESI capillaries.) Despite the apparent variability in the extent of head group binding between replicates, which is attributed to the use of different nESI capillaries, GPC and PC consistently display the lowest extent of binding, with up to two bound to Ubq^{5+} (Figures 3a, 3d, S2, and S3, respectively); PS exhibits the greatest extent of binding, with up to twelve bound to Ubq^{5+} (Figures 3m, and S4); and PE and PG fall between these extremes (Figures 3g, 3j, S5, and S6). Interestingly, GPC acts as a mild charge reducing reagent under the same instrumental conditions, increasing the relative abundance of Ubq^{4+} in the raw nESI spectrum as compared to all other head groups studied.

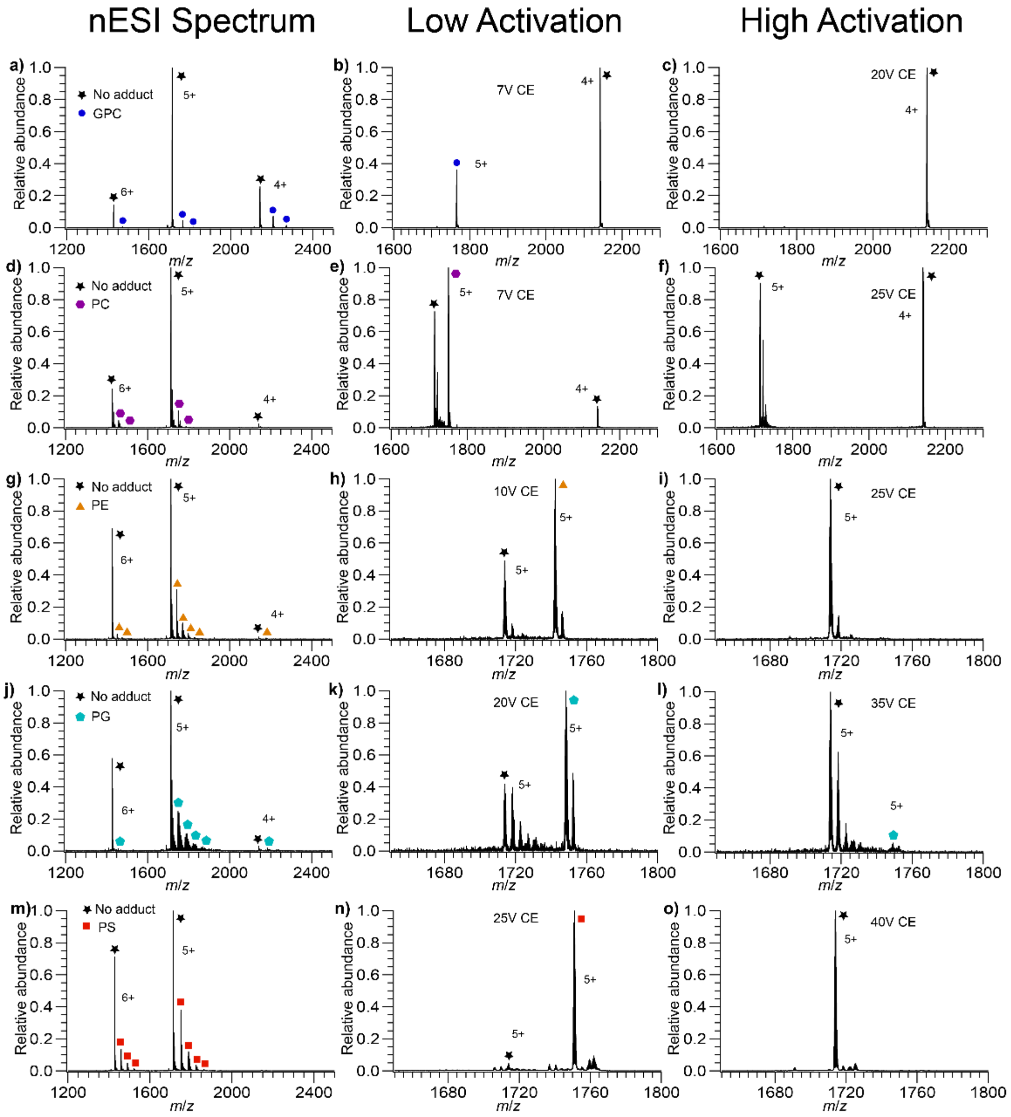

Figure II-3. *Mass spectra of GPC, PS, PC, PG, and PE bound to Ubq.* ***(a)*** *Ubq with GPC bound,* ***(b)*** *isolated Ubq^{5+} with one GPC bound at low activation,* ***(c)*** *isolated Ubq^{5+} with one GPC bound at high activation,* ***(d)*** *Ubq with PC bound,* ***(e)*** *isolated Ubq^{5+} with one PC bound at low activation,* ***(f)*** *isolated Ubq^{5+} with one PC bound at high activation,* ***(g)*** *Ubq with PE bound,* ***(h)*** *isolated Ubq^{5+} with one PE bound at low activation,* ***(i)*** *isolated Ubq^{5+} with one PE bound at high activation,* ***(j)*** *Ubq with PG bound,* ***(k)*** *isolated Ubq^{5+} with one PG bound at low activation,* ***(l)*** *isolated Ubq^{5+} with one PG bound at high activation,* ***(m)*** *Ubq with PS bound,* ***(n)*** *isolated Ubq^{5+} with one PS bound at low activation,* ***(o)*** *isolated Ubq^{5+} with one PS bound at high*

activation. In the isolated spectra at low activation there is a small amount of Ubq with no adducts present, due to a combination of imperfect mass selection (most prominent in the PC spectra) as well as dissociation due to the isolation (most prevalent in the PE and PG spectra). Data from three other replicates for each head group, acquired using different nESI capillaries, are shown in the Supporting Information (Figures S2-S6).

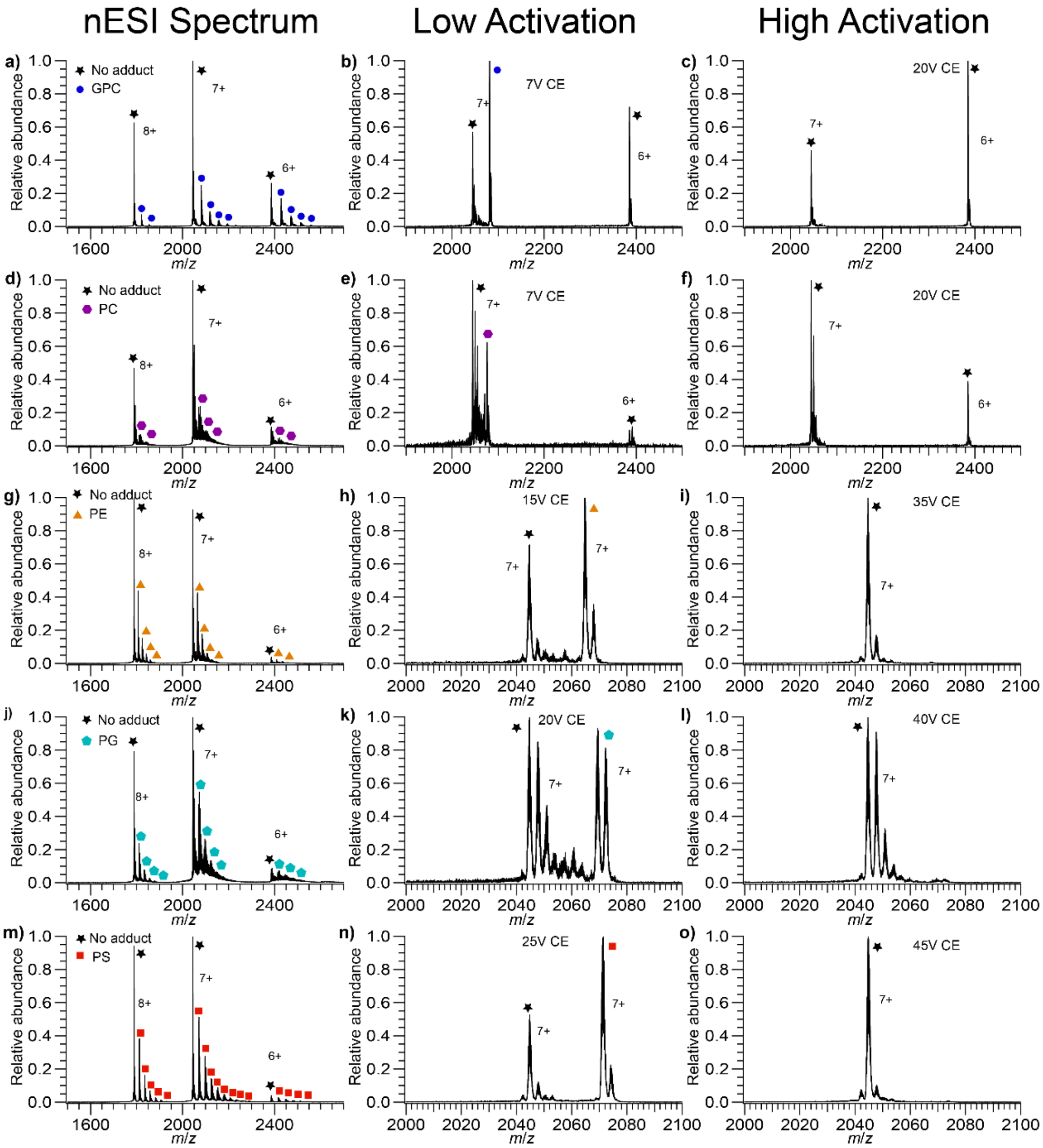

Figure II-4. *Mass spectra of GPC, PC, PE, PG, and PS bound to LZ.* ***(a)*** *LZ with GPC bound* ***(b)*** *isolated LZ^{7+} with GPC bound at low activation* ***(c)*** *isolated LZ^{7+} with GPC bound at high activation* ***(d)*** *LZ with PC bound* ***(e)*** *isolated LZ^{7+} with PC bound at low activation* ***(f)*** *isolated LZ^{7+} with PC bound at high activation* ***(g)*** *LZ with PE bound* ***(h)*** *isolated LZ^{7+} with PE bound at low activation* ***(i)*** *isolated LZ^{7+} with PE bound at high activation* ***(j)*** *LZ with PG bound* ***(k)*** *isolated LZ^{7+} with PG bound at low activation* ***(l)*** *isolated LZ^{7+} with PG bound at high*

activation ***(m)*** *LZ with PS bound* ***(n)*** *isolated LZ^{7+} with PS bound at low activation* ***(o)*** *isolated LZ^{7+} with PS bound at high activation. PS binds the most extensively, PC the least, with GPC, PE, and PG falling in between. In the isolated spectra at low activation there is some LZ with no adducts, due to a combination of imperfect isolation and dissociation due to the isolation.*

Analogous mass spectra for LZ with each head group are shown in Figures 4 and S7-S11. (A nESI spectrum of LZ with no lipid head group present is shown in Figure S1 for comparison.) Overall, the level of adduction of head group and the ease with which they can be dissociated from LZ follows the same trends as for Ubq. PS, PG, and PE typically adduct to a greater extent than do PC and GPC, and GPC has a slight charge-reducing effect, in this case increasing the relative abundance of LZ^{6+} in the raw nESI mass spectra. Given the variation in the extent of lipid head group binding observed between the replicates, this overall agreement between the Ubq and LZ data suggests that these trends are relatively robust toward differences in the nESI process (such as initial droplet size or heating experienced during the nESI process) occurring between different nESI capillaries.

CID of protein-head group complexes: proton abstraction. Thermochemistry of the protein-lipid head group interactions was probed using CID and compared to expectations based on the gas-phase basicity ($-\Delta G°$ of protonation at 298 K) of each head group. Our hypothesis was that PC and GPC should be most likely to abstract a proton from Ubq or LZ ions due to the very high GB of the PC head group (exceeding that of the most basic amino acid, arginine), whereas less proton abstraction should be observed for the other, lower-basicity head groups. For each protein and head group combination, CID was performed by scanning the collision voltage in 1 V increments from a minimally-activating voltage to one sufficient to cause complete head group dissociation but not observable covalent bond fragmentation. Isolation mass spectra for the singly-adducted state of each protein are shown in the middle column of Figures 3 (Ubq), 4 (LZ), and S2-S11 (both Ubq and LZ). To account for the presence of some non-adducted Ubq and LZ observed after isolation, the raw fraction of observed precursor in subsequent CID kinetics experiments was divided by this initial fraction of dissociated precursor observed upon isolation. The right-hand columns of Figures 3, 4, and S2-S11 show isolated mass spectra at high activation, indicating that there is a single CID product in all cases except PC. While PE, PG, and PS all dissociate exclusively as neutral species, GPC dissociates as a cation, and PC dissociates predominantly as a cation and to a lesser extent as a neutral. These results agree with those predicted by comparison of GB values of the lipid head groups and basic amino acids.[57]

CID of protein-head group complexes: dissociation energies. In addition to the charge-abstraction capabilities of each head group, the fraction of lipid head group-bound protein ions surviving activation was also studied as a function of CID voltage and compared to predictions based on GB. Seminal experimental and computational results from Johnson and coworkers[301] showed that gas-phase bases with similar GB tend to form stronger shared-proton bonds than do those with very different proton binding energies. Arginine residues are highly basic in the gas phase (GB 1006.6 kJ/mol[292]) and are plentiful at the surface of many native proteins. Thus, it is expected that these residues will carry the majority of positive charges upon nESI. Because PC and GPC have quaternary ammonium groups, they cannot share a proton via these functional groups with residues on the protein surface, thus any shared-proton interactions involving these head groups and a protonated amino acid likely involve the phosphate group. Such an interaction should be neutral, because the positive charge is held by the quaternary ammonium group, in these cases. By contrast, PE and PS have highly basic primary amine groups that can form strong shared-proton interactions with protonated amino acids, and the charge in such interactions is localized there. PG has relatively low basicity phosphoric acid and glycerol groups, thus it can form either neutral or net positively-charged interactions with protonated amino acids. Based on their relative GB and these chemical constraints, we therefore hypothesized that PC and GPC should form relatively weak interactions with protonated protein ions, because the interaction site is likely neutral, whereas PE, PS, and PG can form stronger, net positively-charged, shared-proton bonds with the protein. We further expected that PE and PS should form stronger interactions than PG, based on the higher computed GB of these two head groups (~950 kJ/mol, much closer to that of arginine) as compared to PG (~906 kJ/mol).[57]

For both Ubq and LZ, in each set of trials, the same ranking of interaction strength is observed experimentally, that is, GPC dissociates at the lowest CID voltage, followed closely by PC, then PE, PG, and finally PS (Figures 5 and 6). This ordering is almost identical to the ordering expected based on the above arguments, except that PG binds more tightly than expected. For both proteins, PC and PG adduct mass spectra indicate more concomitant sodium adduction than observed for the other head groups. Increased salt adduction can lead to increases in measured CID energies,[302] but the degree of sodiation in the nESI mass spectra did not appear to affect the dissociation behavior of the lipid head groups studied here for either protein, indicating that any effect of increased sodium adduction is likely small. Instead, since the non-specific interactions studied here are formed in the latter stages of the ESI process and may be concurrent with charging of the protein, it is possible that the presence of a significant amount of PG causes alternative charge configurations, i.e., protonation at sites other than arginine, to become favored. This possibility of solution additives affecting the location but not the number of charge sites is intriguing; further studies are necessary to confirm this possibility but are beyond the scope of this report.

Activation energies for protein-head group CID. Activation energies were determined using our previously-introduced method for each protein and head group. Kinetic plots as a function of reciprocal effective temperature for Ubq and LZ are shown in Figures S12 and S13, respectively. $\Delta G^{\ddagger}$ for each head group and protein are illustrated in Figure 6, and $\Delta G^{\ddagger}$, $\Delta H^{\ddagger}$, and $\Delta S^{\ddagger}$ values are shown in Table S1. (For precursor ions that exhibited some dissociation upon isolation, this dissociation was subtracted from that produced by subsequent CID activation in deriving barrier thermochemistry values.) Despite variability in the extent of lipid head group binding between replicates in the nESI mass spectra, $\Delta G^{\ddagger}$ values fall between 65 and 81 kJ/mol for all head groups and both proteins and follow the same trend as the midpoint CID voltages of the breakdown curves, i.e., PS > PG > PE > PC > GPC. Good reproducibility was observed between all 4 trials, with a standard deviation of ~1-3 kJ/mol (Figure 6; and Table S1). The highest $\Delta H^{\ddagger}$ measured for both proteins are for GPC and PC (Table S1), likely due to the presence of a reverse Coulomb barrier, as these two lipid head groups dissociate bearing a positive charge.

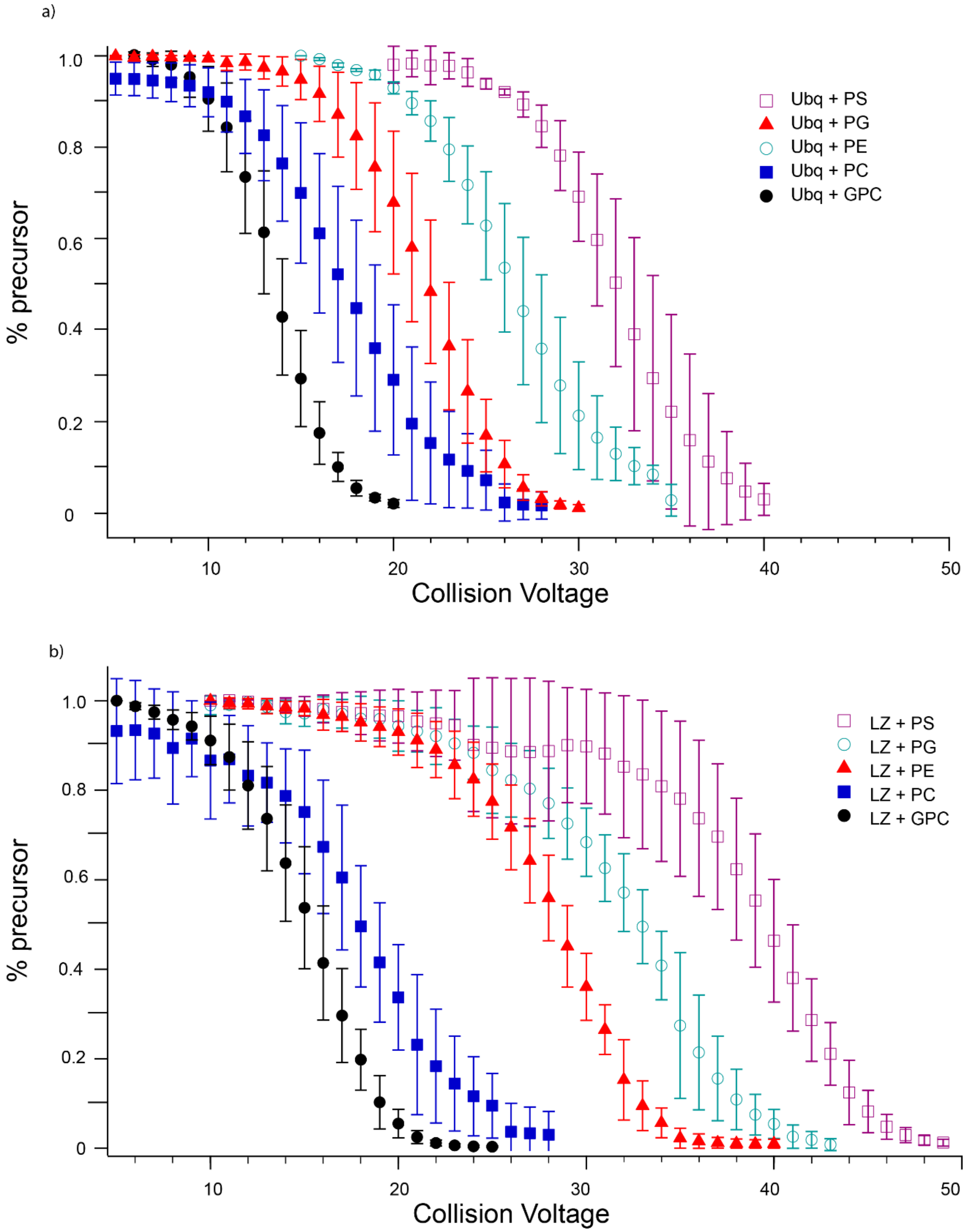

Figure II-5. Breakdown curves for dissociation of lipid head groups from ***(a)*** *Ubq*$^{5+}$ ***(b)*** *LZ*$^{7+}$*. For both proteins, the same trend in lipid head group binding strength is observed, namely PS >*

PG > PE > PC > GPC. Some dissociation of GPC from Ubq was observed upon isolation, as shown in ***(a)****; this was subtracted from CID-induced dissociation in determining barrier thermochemistry values.*

GPC and PC also have the highest $\Delta S^{\ddagger}$ values, which may be indicative of rearrangement to a relatively large ensemble of conformations following abstraction of charge by GPC/PC. Thus, activation energetics measured by this method agree with trends inferred from breakdown curve data and have the unique further advantage of uncovering subtle differences in the CID process for different head groups, as indicated by differences in $\Delta S^{\ddagger}$ and $\Delta H^{\ddagger}$ that may not be obvious from the appearance of the breakdown curves or the 50% dissociation voltage alone.

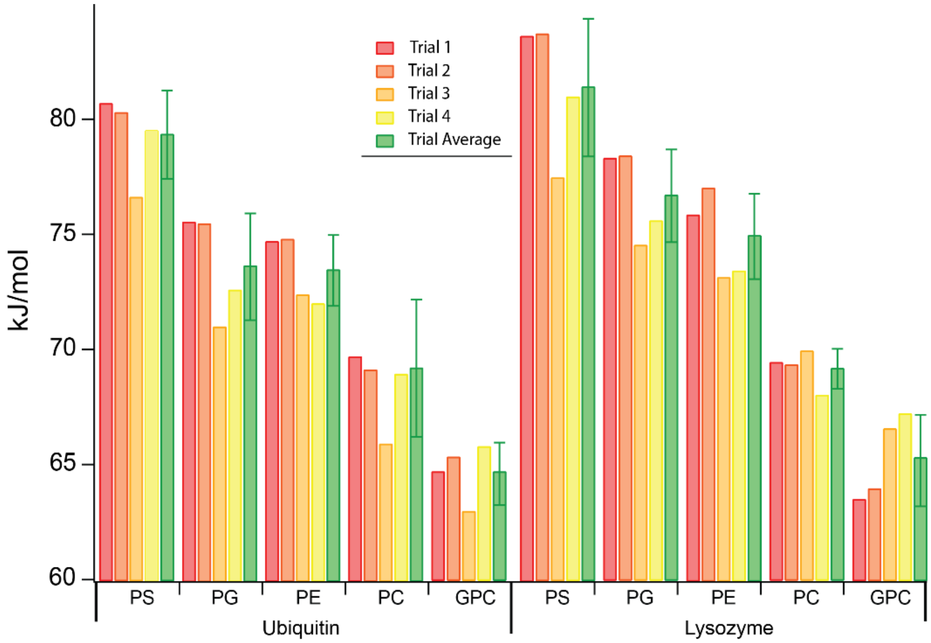

Figure II-6. *Gibbs free energies of dissociation for lipid head groups bound to Ubq and LZ in CID experiments, along with their average and standard deviation across four replicate experiments performed on different days with different nESI capillaries.*

Non-specific binding to a larger soluble protein: transferrin. We also investigated non-specific lipid head group binding to a much larger soluble protein, transferrin (TF, 80 kDa), chosen for its homogenous mass distribution, which facilitates assignment of mass spectral peaks in comparison to other large proteins with multiple isoforms (Figure S14). Mass spectra were first collected under identical instrumental conditions without isolation to assess the overall extent of lipid head group adduction. Figure 7 shows mass spectra for TF with either PS, PE, PG, or GPC head groups bound. (Extensive calcium binding was observed for this protein with PC head group due to the presence of calcium in the PC reagent; PC binding to TF was not explored further due to the very low mass spectral resolution obtained due to this calcium interference.) At a low level of activation (Figure 7a), individual adducts were not resolved for any of the head groups. Increasing the Trap CE to 70 V clearly resolves adducts for all head groups except PG, which is partially resolved (Figure 7c-f). PG is anionic, and sodium counter-ions present in the PG sample adduct to this protein and decrease mass spectral resolution. The extent of binding under these conditions follows the order PS > PE ~ PG > GPC, in agreement with that observed for Ubq and LZ. In addition, at 70 V Trap CE, GPC strips charge from TF, shifting the charge state distribution lower (Figure 7b and S17). This, again, agrees with predictions based solely on the GB of this head group and is in line with the above observations of GPC dissociating with a charge from Ubq and LZ.

Deconvolved mass spectra at several Trap CE values reveal the relative strength of binding of the lipid head groups to TF (Figure S16), confirming that PS requires the most activation to dissociate. Interestingly, while GPC dissociates readily, the overall number of GPC adducts remains equal to or perhaps slightly higher than the number of PE or PG adducts when the whole charge state distribution is examined (Figure S16b-d). This is attributed to the charge stripping effect of GPC, that is, as GPC adducts dissociate and lower the charge of the remaining protein ion, the Coulombic contribution to the barrier for further dissociation of GPC adducts decreases, allowing some GPC adduction to persist even at high levels of activation. Overall, the results for TF are in excellent agreement with those for Ubq and LZ and further confirm the essential role of GB in lipid head group binding energetics for these proteins.

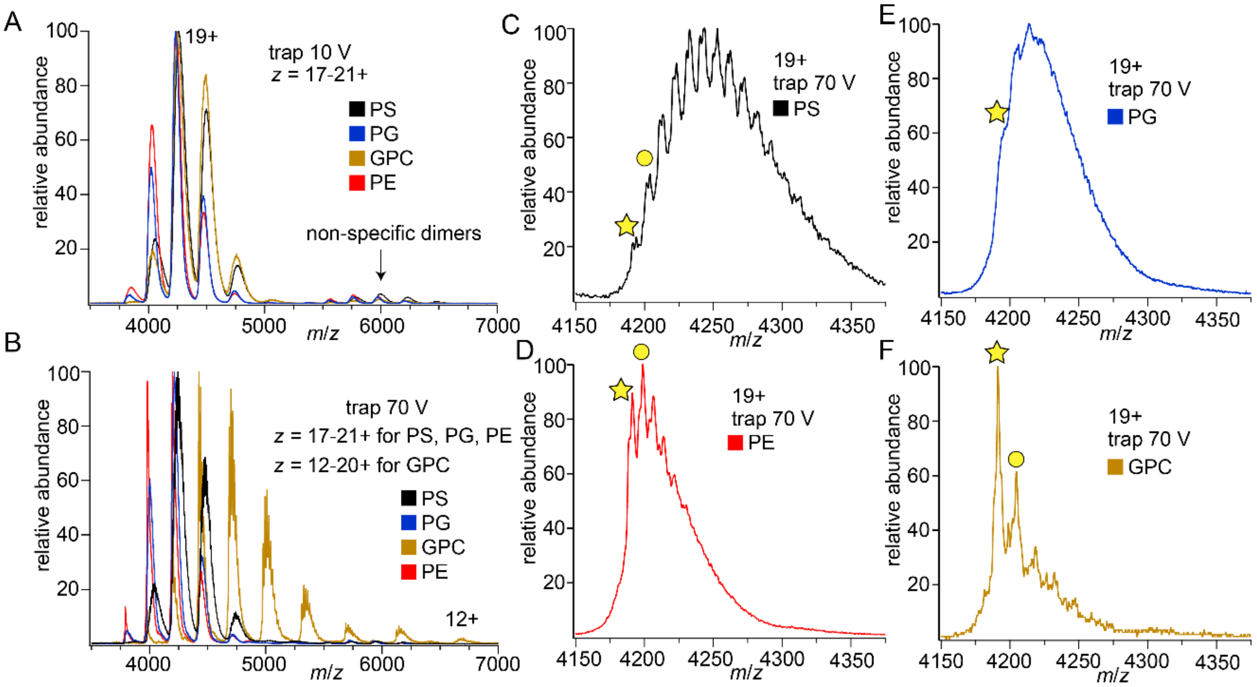

Figure II-7. *Mass spectra showing lipid head group adduction to TF at* ***(a)*** *low, 10 V and* ***(b)*** *moderate, 70 V levels of Trap CE. With moderate activation GPC has extensively stripped charge from TF. The other panel show TF*$^{19+}$ *at 70 V Trap CE for each head group:* ***(c)*** *PS* ***(d)*** *PE* ***(e)*** *PG* ***(f)*** *GPC. Stars identify TF*$^{19+}$ *with no adducts, while circles mark the first resolvable head group adduct. Significantly more PS adducts are observed than for the other head groups.*

Competitive head group binding to transferrin. Ideally, native MS can be used to accurately determine the relative binding strength of lipids to membrane proteins based on the relative abundances observed of different lipid adducts in native mass spectra. In most cases, this is currently done by embedding membrane proteins in detergent micelles or Nanodiscs with at least two different lipid types, and inferring from CID experiments which lipids remain bound after most are dissociated from the initial complexes.[144,216,254,261,303] Based on the above results for Ubq and LZ, we hypothesized that, for non-specific complexes of TF with adducted lipid head groups formed by nESI from mixtures of the above head groups, PS would form the strongest interactions with TF and survive the greatest level of collisional activation. Figure 8 illustrates competitive head group binding experiments in which identical concentrations (500 μM) of PS and another head group (GPC, PE, and PG) were mixed with TF in ammonium acetate solution and ionized using nESI. At the lowest level of gas-phase activation (Trap potential 20 V), deconvolved mass spectra exhibited a broad, poorly-resolved "hump" for each head group combination, consistent with extensive adduction.

Because the resolution of these low-activation TF-adduct mass spectra was poor, the breadth of the deconvolved mass spectra (defined at 10% of maximum intensity) was instead used to characterize the maximum possible extent of binding of each different head group. For PS alone, the deconvolved mass spectrum is ~2,000 Da wide (indicating a maximum of ~11 PS head groups adducted), whereas each of the PS/GPC, PS/PE, and PS/PG mixed head group spectra is ~2,500 Da wide. For each of these competing head group mass spectra, this spectral width indicates a maximum of ~13.5 PS or ~10 GPC, ~21 PE, or ~16 PG adducts, respectively, or combinations of these head groups with fewer of each than these maximal numbers. Upon more extensive collisional activation, the observed width of the deconvolved mass spectra decreases in each case, until at 100 V, moderately well-resolved adduct peaks with a spacing consistent with PS (measured spacing 184 ± 2 Da, as compared to molecular weight 185.07 Da), as well as a spectral width of ~1,500 Da, are observed in each case. This width is consistent with a maximum of ~8 PS, ~6 GPC, 12.5 PE, or ~9 PG adducts. Due to the large mass difference between the PS and GPC head groups (185 and 257 Da, respectively), all of the moderately-well resolved peaks in the PS and PS/GPC spectra at 100 V collisional activation could be unambiguously assigned to PS adducts, and no distinct GPC adduct complexes were clearly resolved. This result indicates that PS binds more strongly to TF than does GPC, consistent with expectations based on the Ubq and LZ experiments described above. The lower mass spectral resolution obtained with PS/PE and PS/PG at 100 V activation, by contrast, likely indicates the presence of both head group types, due to the smaller mass differences between these head groups. For PS/PE, mass spacings consistent with both PS (measured spacing 180 Da ± 10 Da) and PE (measured spacing 144 ± 4 Da, as compared to PE molecular weight 141.06 Da) were both identified by "Double Fourier Transform" of the mass spectrum,[298,300] with the PS peak larger than the PE peak. For PS/PG, mass spacings of 183 ± 4 Da and 175 ± 4 Da were observed by Double Fourier Transform of the mass spectrum, similar to the molecular weights of PS and PG (185.07 Da and 172.07 Da, respectively), with both peaks having similar intensities. Overall, these results are highly consistent with expectations based on the Ubq and LZ results described above as well as head group GB values, indicating a level of adduction after 100 V activation in the order PS ~ PG > PE > GPC. These results illustrate that, at high levels of activation used to remove most head groups, gas-phase binding thermochemistry can play a large role in determining which head groups are robust to dissociation.

Figure II-8. *Deconvolved mass spectra of lipid head group binding to transferrin at different levels of collisional activation.* ***(a)*** *PS only* ***(b)*** *competitive binding between PS and GPC* ***(c)*** *competitive binding between PS and PE* ***(d)*** *competitive binding between PS and PG.*

Conclusions

Non-specific binding of several model lipid head groups to soluble proteins in positive ion mode was investigated with native MS and CID, including the propensity of these head groups to remove charge upon dissociation and dissociation barrier thermochemistry. PC and GPC head groups have the greatest tendency to remove charge from the proteins studied upon CID, and PS, PE, and PG head groups dissociate exclusively as neutral molecules, in agreement with expectations based solely on the relative gas-phase basicities (GB) of these head groups and those of amino acid residues.[57,292] PS head group has the highest barrier for dissociation from the proteins studied, followed by PG, PE, PC, and GPC, and these results are robust to variability in the overall extent of head group binding across replicates due to use of different nESI capillaries. These results are largely in agreement with expectations based on relative GB values, in combination with the fact that PC and GPC cannot participate in shared-proton interactions at their permanent charge sites due to the presence of the quaternary ammonium group. However, PG, which might not be expected to form a strong interaction based on its relatively low GB, in fact forms the second strongest interaction.

$\Delta G^{\ddagger}$ values for dissociation of each head group are remarkably similar for Ubq and LZ (<4% difference for the same head group, as compared to a difference of ~20% between the most tightly and most weakly bound head groups) and follow identical trends. Intriguingly, the range of $\Delta G^{\ddagger}$ is relatively narrow (~65-82 kJ/mol) despite a wider range of $\Delta H^{\ddagger}$ (105-159 kJ/mol for Ubq and 84-117 kJ/mol for LZ), indicating a large degree of enthalpy-entropy compensation. In agreement with results for Ubq and LZ, competitive binding experiments for the same lipid head groups to TF, a much larger protein, show that PS forms the strongest non-specific bonds to TF and that the presence of GPC adducts on TF leads to significant charge stripping upon CID.

Together, the above results suggest a signature for non-specific binding of lipids to proteins with native-like structures and charge states in positive ion mode: prevalent charge stripping by lipids with phosphocholine head groups (such as phosphatidylcholines and sphingomyelins) upon CID and lipid binding strengths in the order PS > PG > PE > PC.

Adduct migration and evaporation-induced non-specific adduction are both phenomena that must be considered in designing and interpreting native MS experiments to identify physiologically relevant protein adducts such as drug targets, lipids, or cofactors. Because the potential energy surface in the gas phase can be very different from that in solution, slow-heating methods such as CID can in principle result in dissociation behavior that reflects the gas-phase potential energy surface more than that in solution, especially when activation is very extensive. Whether this occurs inherently depends on relative barriers for dissociation as well as the internal temperature of the ions achieved during CID and the timescale of the experiment. The above results provide a benchmark for assessing whether signatures of dissociation behavior dominated by gas-phase thermochemical properties, possibly after adduct migration, may be present in native MS-based lipid binding experiments. In combination with the ion heating/cooling and CID kinetics modeling described here, these results also provide a model for examining effects of gas-phase enthalpy and entropy in protein-ligand interactions using native MS. Furthermore, PC and GPC head groups behave similarly to other reagents used for charge reduction in native MS experiments in positive ion mode,[304–306] suggesting they could be useful in this capacity. PS head group, in contrast, may adduct strongly to many native protein ions, potentially enabling deliberate alteration of gas-phase unfolding and dissociation pathways, as observed recently for some covalent protein adducts.[307]

III. EFFECTS OF NANO-ELECTROSPRAY IONIZATION EMITTER POSITION ON UNINTENTIONAL IN-SOURCE ACTIVATION OF PEPTIDE AND PROTEIN IONS

This chapter includes previously published co-authored material with co-authors Austin Green, Elizabeth Resendiz, Kenneth Newton, Ruwan Kurulugama, and James Prell. Project conceptualization and design were performed by Samantha Shepherd with advice and input from Kenneth Newton, Ruwan Kurulugama, and James Prell. Data collection and analysis were performed by Samantha Shepherd, Austin Green, and Elizabeth Resendiz. The manuscript was written by Samantha Shepherd and edited by James Prell.

Abstract

Native ion mobility-mass spectrometry (IM-MS) typically introduces protein ions into the gas phase through nano-electrospray ionization (nESI). Many nESI setups have mobile stages for tuning ion signal and extent of co-solute and salt adduction. However, tuning the position of the emitter capillary in nESI can have unintended downstream consequences for Collision Induced Unfolding or Collision Induced Dissociation (CIU/D) experiments. Here, we show that relatively small variations in nESI emitter position can shift the mid-point (commonly called the “CID50” or “CIU50”) potential of CID breakdown curves and CIU transitions by as much as 8 V on commercial instruments. A spatial “map” of the shift in CID50 for loss of heme from holomyoglobin onto emitter position on a Waters Synapt G2-S*i* mass spectrometer shows that emitter positions closer to the instrument inlet can result in significantly greater in-source activation, whereas different effects are found on an Agilent 6545XT instrument for the ions studied. A similar effect is observed for CID of singly protonated leucine enkephalin peptide and

Shiga toxin 1 subunit B homopentamer on the Synapt G2-S*i*. In-source activation effects on a Synapt G2-S*i* are also investigated by examining RMSD between CIU fingerprints acquired at different emitter positions and shifts in CIU50 for structural transitions of bovine serum albumin and NIST monoclonal antibody.

Introduction

Native mass spectrometry (and its variant coupled to ion mobility spectrometry, IM-MS) can be a powerful tool to probe protein structures and interactions. Nano-electrospray ionization (nESI) is widely used for native IM-MS because it can transfer kinetically trapped native-like structures to the gas phase for structure analysis. nESI has been shown to be capable of retaining secondary, tertiary, and quaternary structure in many protein complexes both experimentally[10,13,49,50] and computationally.[43,100,101] By deliberately adding internal energy to native-like ions in the gas phase, collision induced unfolding (CIU) and/or dissociation (CID) can be used to identify differences in biomolecule structure, augmenting the capabilities of native IM-MS.[3–5,7,138] These structural differences range from relatively large, such as those in high-order structure or ligand binding sites,[215,217,219,227,308] to much more subtle, such as those due to differences in proteins with nearly identical collision cross section distributions in the absence of deliberate activation.[32] Structural information determined by native IM-MS often agrees very well with results from more traditional biophysical and biochemical techniques.[8–10,13,33,138,139,142,216,217,219,255,309–312]

Although nESI can kinetically trap biomolecular complexes in native-like structures, it is also known that the chemical and physical properties of the nESI droplet are dynamic.[76,149,156,158,159,180,309] For example, even with the use of volatile buffer salts such as ammonium acetate, the effective pH of droplets can change by as much as 2 pH units as the droplets evaporate,[313,314] and, over time, nESI may acidify neutral ammonium acetate solutions in positive ion mode nESI.[177] Other examples of protein disruption in nESI include redox reactions associated with nESI,[212,315] intrinsic native ECD,[24] annealing of the nascent analyte ion,[152] electrothermal supercharging,[152] and nozzle-skimmer dissociation[123–125] (a type of in-source CID).

Collisional activation (i.e., nozzle-skimmer dissociation) has long been used to deliberately activate and fragment nascent biomolecular ions in MS as they enter the instrument, but collisional activation (CID and CIU) inside the instrument is more commonly used in modern instruments due to more precise control of energy deposition and the ability to first isolate ions of interest.[1] In CIU/D, modern instruments typically use an adjustable electric potential (the "injection potential") to accelerate the analyte ion into a region filled with buffer gas. Collisions between the analyte ion and the gas heat the analyte, causing dissociation and/or unfolding. The fraction of remaining precursor ion can be plotted as a function of injection potential to produce a breakdown curve. A common metric to compare breakdown curves generated by these methods are CID50 and CIU50 values, i.e., the injection potential at which 50% of the precursor ion has undergone a measurable dissociation or change in collision cross section, respectively.[186,316,317] Because collision gas and pressures, collision cell design, and other properties can differ greatly between instruments and may be user-controlled, CIU50 and CID50 values can be challenging to compare between instruments or experimental conditions. For example, within a single instrument, activation early on in the ion path, e.g., in the StepWave of a Waters Synapt G2-S*i* instrument, can shift breakdown curves and CIU fingerprints along the injection potential axis.[13,69] This shift can be "additive" in the sense that CIU50 values for successive structural transitions are all shifted to higher voltage by approximately the same amount on this instrument, but it is not generally known whether this is the case for other instruments, where ions may experience very different buffer gas pressure profiles and electric fields.

A handful of previous studies have shown that the position and orientation of the emitter in conventional electrospray ionization and nESI can affect the observed mass spectrum and in-source activation of protein-ligand complexes,[180,184,318] and other studies have investigated the internal energy distribution of ions in ESI.[73–76,181,182] These studies show that emitter position, emitter orientation, and electrospray potential can individually help desolvate and desalt ions and increase mass accuracy, but some combinations of them can lead to dissociation. These studies also demonstrate that greater desalting can occur when there are larger distances between the emitter opening and the instrument inlet.

Control and reproducibility of ion charge state distributions[145] and structures using nESI can be a hurdle to obtaining highly consistent CIU and CID data, both over time and between laboratories. nESI emitters, which can vary in both material and physical dimensions, are often pulled to different opening diameters by different methods in different laboratories,[166,168,319] likely resulting in different initial nESI droplet sizes. Laboratories often further optimize source temperature and emitter position to optimize signal strength and reduce the degree of unwanted co-solute or salt adduction, though the precise position of the emitter is rarely reported in publications and may vary from user to user or even spectrum to spectrum. A small number of reports in the literature examine variability in CID/U data and explore design principles to increase reproducibility. Loo and coworkers attributed variation in mass spectra and ion behavior between users without a clear explanation to different users having a different “touch” for ESI.[180] They reported that each user, even on the same day, observed differences in mass spectra of protein and protein complex analytes generated from ESI. In contrast, a collaborative effort between three laboratories showed that an “in-source CIU” modification for Agilent Technologies 6560C IM-MS instruments can reduce CIU fingerprint RMSD values for the same analyte between source hardware to less than 5%.[90]

Here, effects of nESI emitter position on in-source ion activation in CID and CIU experiments are systematically studied on two different commercial instruments (a Waters Synapt G2-Si quadrupole–IM–time-of-flight, Q-IM-TOF, instrument and an Agilent 6545XT Q-TOF instrument) for several protein and peptide ions. Based on these results, strategies are provided for use in nESI-(IM)-MS experiments to minimize unintentional in-source activation and increase reproducibility.

Methods

All peptide and protein samples were obtained from Sigma Aldrich (St. Louis, MO, USA) as lyophilized proteins and used without further purification. Equine heart myoglobin (SKU: M1882), leucine enkephalin acetate salt (SKU: L9133), bovine serum albumin (BSA, SKU: 05470), Shiga toxin 1 subunit B (SKU: SML0562), and NIST IgG1κ monoclonal antibody (NIST mAb, SKU: 8671) were reconstituted in water and buffer swapped using Micro Bio-spin 6 columns (Bio-Rad, Hercules, CA) into pH 7.4, 200 mM ammonium acetate solution to generate native protein solutions. Partially denatured myoglobin solution, as described elsewhere,[51] was also prepared to yield a myoglobin sample with a single dominant CID loss channel. For this sample, reconstituted holomyoglobin was buffer swapped into 18 MΩ·cm water and diluted with methanol (Thermo Scientific, Waltham, MA) to yield an 80/20 vol/vol water/methanol solution. All final sample concentrations ranged from 5-15 µM with the exception of a high-concentration native myoglobin sample prepared as 35 µM. The nESI source on both instruments was operated in positive ion mode under static-nESI conditions using 1.0/0.78 mm o.d./i.d. borosilicate glass nESI emitters pulled to ~2-micrometer i.d. openings using a P97 Flaming-Brown micropipette puller (Sutter Instrument, Novato, CA, USA) without further modification. nESI was initiated by applying a 0.9-1.5 kV potential to a platinum wire inserted into the solution inside the emitter without use of an external syringe pump. Throughout the manuscript the term "close" refers to the emitter position in which the tip of the emitter is as close to the entrance of the instrument as possible without breaking the tip of the emitter on the instrument inlet cone (an xyz position of 0 ± 0.2, 0.5 ± 0.5, 0 ± 1 mm relative to the center of the inlet, where x, y, and z represent the vertical [above/below the center of the inlet cone], horizontal along inlet axis, and horizontal perpendicular to inlet axis distances relative to the inlet). "Far" positions varied. A complete description of all positions used in included in Table S1.

To assess variability in nESI emitter dimensions, a field-emission, variable-pressure scanning electron microscope (Thermo Fisher Apreo 2S Lo, Thermo Scientific, Waltham, MA) was used. The i.d. of the pulled emitter openings overall was 2.2 ± 0.6 µm, and the distance from the onset of the taper at the end of the emitter to the emitter opening was 3.3 ± 0.1 mm. Further information on emitter reproducibility and settings is included in the SI (see Appendix S1 and Figure S1).

All (IM-)MS data were analyzed using Unidec,[171] Python, and CIUSuite 2 (using settings listed in Table S2).[86] For CIU experiments, RMSD "average of pairwise root mean square deviation" ($\text{RMSD}_{\text{AofP}}$) is used to refer to the average of two or more experiment-to-experiment pairwise RMSD values and $\text{RMSD}_{\text{PofA}}$ is used to refer to the pairwise RMSD of two averaged CIU fingerprints. Further discussion of the differences between these metrics is included in the supporting information (Appendix S2). Data for CIU experiments were collected in quintuplicate at each position with 3 of the 5 trials collected using the self-same emitter without moving it.

Results and Discussion

Choice of samples. CID can be used to fragment covalent bonds in both peptides (e.g., in bottom-up and middle-down proteomics) and proteins (e.g., in top-down proteomics) as well as noncovalent bonds in native MS. In order to survey effects of nESI emitter position in both CID and CIU, we used the common MS standard peptide leucine enkephalin (amino acid sequence YGGFL) and the proteins equine holomyoglobin (which dissociates by loss of a non-covalently bound heme ligand), Shiga toxin 1 subunit B pentamer (as an example of a homooligomer), bovine serum albumin (BSA, which has multiple accessible CIU transitions), and NIST humanized IgG1κ monoclonal antibody (NIST mAb, as a representative of this class of mAb that is of major current interest in CIU applications).[32] Holomyoglobin, notably, is known to exhibit two competitive CID channels (loss of positively charged heme and loss of neutral heme)[212] when prepared by nESI from aqueous ammonium acetate, whereas it dissociates almost exclusively by loss of charged heme when prepared by ESI from 80/20 water/methanol solution. The latter behavior is attributed to partial denaturation of the protein in the water/methanol solution, consistent with its slightly shifted charge state distribution in positive ion mode (see Figure 1). However, the extent of denaturation is not sufficient to lose the heme in solution, and the precise BIRD values obtained for the partially denatured ions in studies by the Williams group indicates that the ions' structures are still relatively homogeneous.[128] Furthermore, it is known that the oxidation state of native holomyoglobin and the relative prevalence of the neutral vs. charged heme loss channels upon CID are correlated.[212] Loss of heme^{0} from holomyoglobin upon CID has been associated with precursor holomyoglobin containing Fe(II), and loss of a heme^{1+} is associated with precursor holomyoglobin containing Fe(III). The latter oxidation state can result from oxidation of the nESI solution after many minutes of continuous spray, but it has been shown that other heme-containing proteins can undergo intrinsic native ECD at high concentrations to produce monomers containing Fe(III).[24]

Figure III-1. *Mass spectra for myoglobin ions from 80/20 water/methanol (a) and aqueous ammonium acetate (b). The primary dissociation channels for each solution condition are shown in (c) water/methanol (loss of heme*$^{1+}$*) and (d) ammonium acetate (competitive loss of heme*^{0} *and heme*$^{1+}$*).*

Figure 1 shows example mass spectra for CID of holomyoglobin ions prepared by nESI from 80/20 water/methanol (partially denatured, Figure 1a) and from neutral 100 mM aqueous ammonium acetate (native-like, Figure 1b). CID of holomyoglobin from water/methanol is strongly dominated by a single dissociation channel via loss of heme^{1+} (Figure 1c), while CID of holomyoglobin from ammonium acetate exhibits both this loss channel and loss of heme^{0} (Figure 1d). The single CID channel for holomyglobin from 80/20 water/methanol solution facilitated determination of CID50 values when using different nESI emitter positions in many of the experiments described below.

Assessment of protein CIU and CID repeatability using a single nESI emitter and fixed emitter position. In both CID and CIU experiments on native-like proteins, it is often necessary to repeat measurements with different nESI emitters, and, as described in the Introduction, the emitter position is often tuned to some extent to maximize signal and remove salt adducts. To assess the contributions of using different emitters and emitter positions to variability in CID and CIU, it was necessary to first characterize variability associated with the case in which a single emitter is used without changing its position. For CIU, we used metrics commonly used in comparing CIU fingerprints. CIU fingerprints are often acquired in triplicate, and the triplicate-average root mean square deviation (RMSD) between each pair of maximum-intensity-normalized fingerprints is reported as a percentage (“average pairwise RMSD”, hereafter $\mathrm{RMSD}_{\mathrm{AofP}}$) to assess variability. Here, CIU fingerprints of NIST mAb^{25+} were acquired in triplicate (Figure 2 a-c) using a single nESI emitter in a fixed position and TWIMS settings of 650 m/s and 30 V. When averaged (Figure 2d), these fingerprints show a very low $\mathrm{RMSD}_{\mathrm{AofP}}$ (1.19%, Figure 2e and 2f).

A similar set of CIU experiments was performed for BSA^{16+}, and a very low $\mathrm{RMSD}_{\mathrm{AofP}}$ (0.98%, data not shown) was measured. Additional single-emitter $\mathrm{RMSD}_{\mathrm{AofP}}$ values for NIST $\mathrm{mAb}^{22\text{-}26+}$ and $\mathrm{BSA}^{14\text{-}16+}$, averaged over all charge states, are shown in Figure 2f, alongside values for the most abundant charge state of each protein. These results show that CIU fingerprints collected sequentially using a single emitter can be highly repeatable ($\mathrm{RMSD}_{\mathrm{AofP}}$ ~4%), especially for high abundance charge states ($\mathrm{RMSD}_{\mathrm{AofP}}$ ~3%).

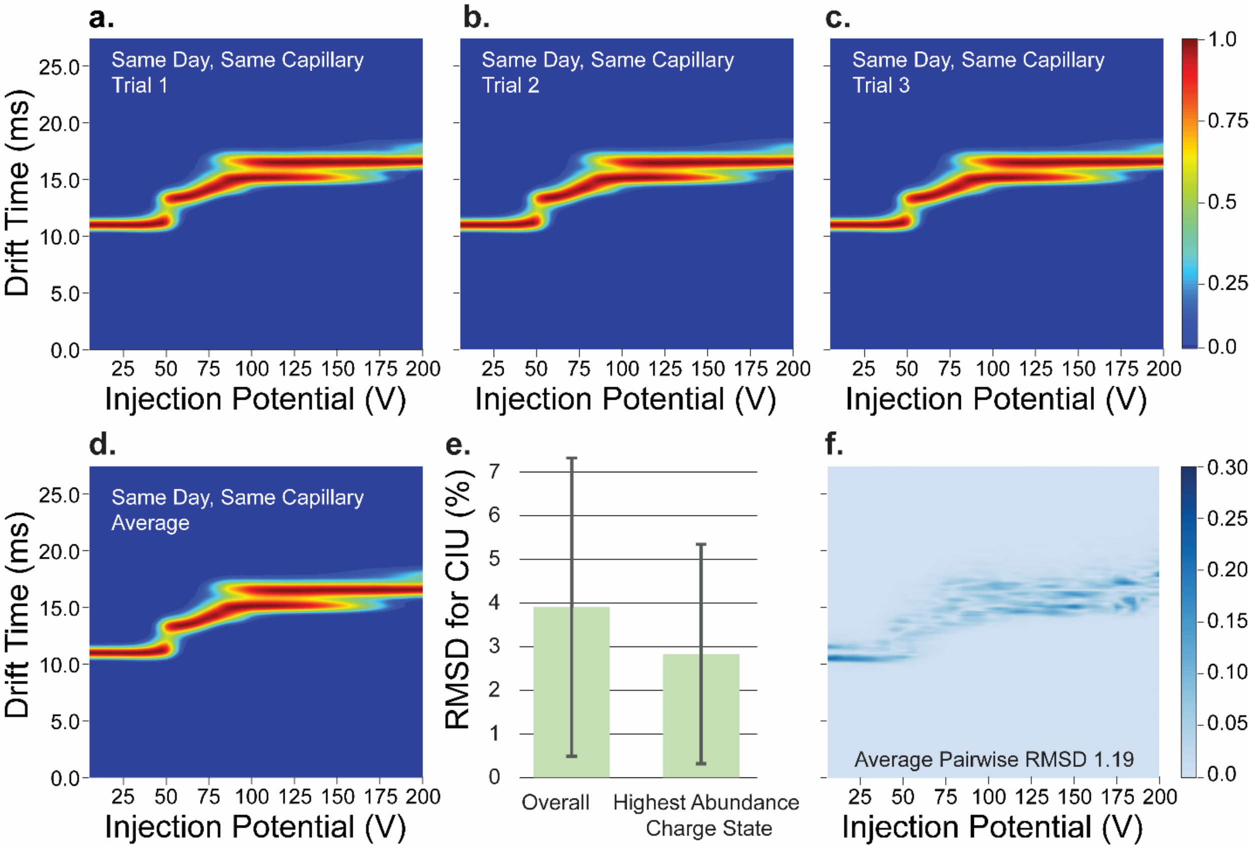

Figure III-2. *CIU fingerprints of NIST mAb25+ collected in triplicate (a,b,c) using a single nESI emitter in a fixed position. The average of these fingerprints is shown in (d). Average (green bar) and single standard deviation (error bars) in pairwise RMSD of CIU fingerprints for all native charge states of NIST mAb (22-26+) and BSA (12-14+) and for only the most abundant charge state (NIST mAb^{25+} and BSA^{16+}) (e). Average CIU difference plot for the fingerprints shown in (a,b,c) for NIST mAb^{25+} (f).*

Reproducibility of CID and CIU using fixed vs. uncontrolled nESI emitter position. CID of singly protonated leucine enkephalin peptide (555 Da) generated by nESI from a solution of pH 7 aqueous ammonium acetate was performed on the Synapt G2-Si using injection potentials between 5 and 35 V. CID of holomyoglobin$^{7\text{-}10+}$ ions (17,549 Da) generated by nESI from a solution of 80/20 water/methanol (vol/vol) was performed with injection potentials between 5 V and 65 V. Figure 3 shows CID breakdown curves for leucine enkephalin (Figures 3a and 3e) and holomyoglobin$^{9,10+}$ in water/methanol (Figures 3b, 3c, 3f, and 3g) in uncontrolled (Figures 3a-c) and fixed (Figures 3e-g) emitter positions across multiple days.

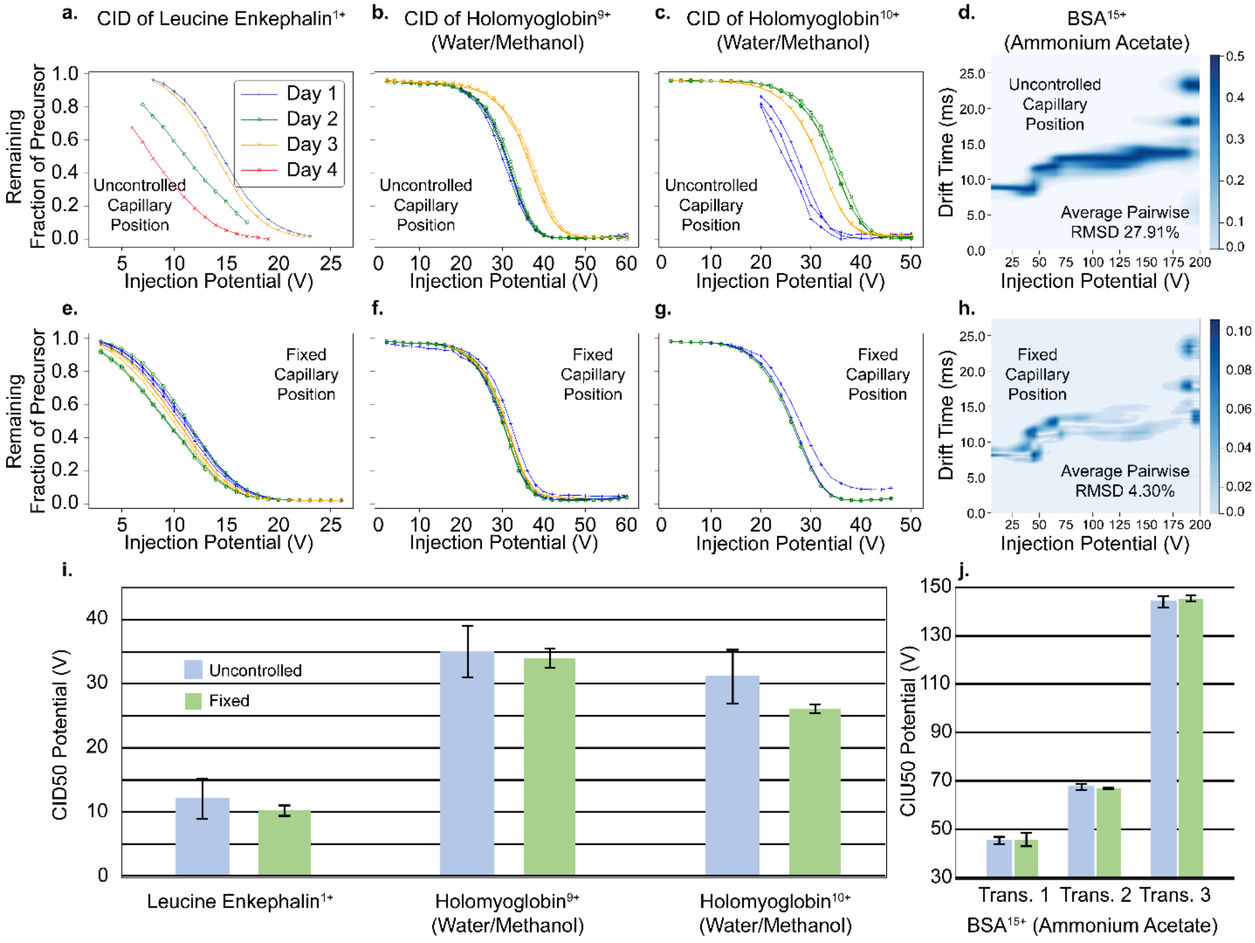

Figure III-3. *CID breakdown curves (a-c, e-g) and CIU fingerprint differences (d,h) in uncontrolled (a-d) and fixed (e-h) nESI emitter positions on a Waters Synapt G2-Si are shown for leucine enkephalin (a,e), holomyoglobin^{9+} (b,f), holomyoglobin^{10+} (c,g), and BSA^{15+} (d,h). Statistics for CID50 are summarized in (i), with error bars representing the standard deviation of CID50 value across all trials. Statistics for CIU50 of BSA^{15+} are summarized in (j), with error bars representing the standard deviation in CIU50 value across three trials.*

In uncontrolled nESI emitter position experiments, the position of the nESI emitter was coarsely tuned by a single user for high precursor signal while minimizing sodium adduction. The CID50 for all three ions (leucine enkephalin and holomyoglobin$^{9,10+}$) had a roughly inverse correlation with the signal strength. (Figure S2 shows example data for holomyoglobin^{9+} from 80/20 water/methanol solution.) That is, higher precursor signal corresponded to greater in-source activation (lower CID50), and positions with lower signal corresponded to less in-source activation (higher CID50; see Figure S2). In contrast, controlling emitter position by using identical nESI stage micrometer settings between days and emitters significantly reduces variability of the replicate-average CID50 for these ions (Figure 3i). The standard deviation in the CID50 for the fixed emitter position experiments was lower by a factor of ~3-6 for all three analytes as compared to that for the uncontrolled emitter experiments. Thus, as for CIU (see above), repeatability in CID experiments can be very high when using a fixed emitter position. These results show that controlling emitter position can improve reproducibility of CID experiments. In principle, use of controlled emitter position can thus increase confidence in interpreting CID50 differences between proteins as structural or stability differences, especially if emitter position is recorded and reported alongside other experimental parameters.

An analogous set of experiments was used to assess effects of nESI emitter position on CIU of BSA^{15+} on a Waters Synapt G2-S*i* using injection potentials from 5-200 V. RMSD values were calculated for uncontrolled emitter positions across multiple days (Figure 3d) and for a fixed emitter position using multiple capillaries (three on the same day; Figure 3h). For BSA^{15+}, the RMSD$_{\mathrm{AofP}}$ for the uncontrolled emitter position experiments (27.91%) is far higher than the accepted standard for reproducibility (< 5%).[90] In sharp contrast, the RMSD$_{\mathrm{AofP}}$ for the fixed emitter position triplicate collected on the same day is 4.30%, which falls within this standard and is clearly higher than that obtained for the triplicate using a single emitter (see above). An effect of similar magnitude of exchanging emitters was observed for all charge states of BSA (14-16+) and NIST mAb (22-26+) that were investigated. The overall $\mathrm{RMSD}_{\mathrm{AofP}}$ for both proteins was determined to be 6 ± 3% across all charge states and 4 ± 2% for the most abundant charge states. Because variation in CIU fingerprints acquired using different emitters in the same position can be larger than that using a single emitter, it is therefore recommended to use multiple emitters to accurately survey CIU variability for a fixed emitter position. In contrast to the CID experiments described above, use of uncontrolled emitter position to optimize for high signal and low salt adduction in CIU resulted in a similar amount of variation (as measured by $\mathrm{RMSD}_{\mathrm{AofP}}$) as did exchanging emitters in a fixed position (Figure 3j).

Taken together, the above results show that controlling nESI emitter position can significantly reduce variability in CID50 and reduce CIU RMSD. Noting and reporting emitter position (e.g., the nESI stage micrometer positions and stand-off of the nESI emitter tip from the stage) can thus facilitate reproducibility between laboratories and improve traceability, as well provide crucial information for literature meta-analysis.

Spatial map of extent of in-source activation due to emitter position in CID experiments. Motivated by the above-described influence of nESI emitter position on variability of CID and CIU data, we investigated whether there was a spatial mapping of this effect onto emitter position and to what extent this effect may vary between different instruments and analytes. Figure 4a shows a spatial map of CID50 onto nESI emitter position for partially denatured holomyoglobin^{9+} on the Waters Synapt G2-S*i*. (An analogous map for holomyoglobin^{10+} is shown in Figure S3.) Representative CID breakdown curves in three emitter positions (“far”, “below”, and “close”; see Figure 4b) show shifts of the entire breakdown curve along the injection potential axis. On the spatial map, emitter positions for which the CID50 is shifted to lower values indicate greater in-source activation for this ion. As can be seen in the spatial map, emitter positions that cause higher in-source activation are located roughly along the inlet axis out to ~3 mm in front of the inlet and then follow a roughly 90° turn toward the axis of the emitter holder. The most activating of these are positions closest to the inlet. Other, more “peripheral” emitter positions cause less in-source activation.

Figure III-4. *(a) A map of the effect of position on CID50 of holomygolobin in water/methanol on a Waters Synapt G2-Si. Blue cubes show the highest CID50 potential required while red cubes show the lowest. (b) CID breakdown curves of holomyoglobin water/methanol at the “close” (red; 0, 0.5, 0.5 mm), “far” (blue; 0, 3, 5 mm), and “below” (black; −3, 1, 1 mm) positions. These positions are shown with arrows in (a). (c) CID breakdown curves of holomyoglobin in ammonium acetate on the Waters Synapt G2-Si at the close (red) and far (blue) positions. (d) CID breakdown curves of holomyoglobin in ammonium acetate on the Agilent 6545XT Q-TOF Mass Spectrometer at a “close” (red; 0.5, 2 mm) and “far” (blue; 2, 5 mm) position. See Methods section for explanation of emitter position coordinates.*

Based on this map, CID was also performed at “high” and “low” activation positions for singly-protonated leucine enkephalin (Figure S4a-d, representative mass spectra Figure S5), native Shiga toxin 1 subunit B pentamer (Figure S4e), and native holomyoglobin^{9+} (Figure 4c) to determine whether a similar spatial pattern holds for other analytes. Differences of ~3 and 4 V were observed for leucine enkephalin and Shiga toxin 1 subunit B pentamer, respectively, with greater in-source activation at the emitter position close to the inlet (Figure S4). A smaller difference of 0.8 V was observed for native myoglobin^{9+} (Figure 4c). Results for all three of these analytes qualitatively agree with the map for partially denatured holomyoglobin^{9+}.

To ascertain whether a similar spatial dependence applies to a different instrument source, the influence of position on an Agilent 6545XT Q-TOF mass spectrometer was studied using native myoglobin and leucine enkephalin with the nESI emitter located close (~1-3 mm) and far (~4-7 mm) from the instrument inlet. On this instrument, no significant difference in CID50 was observed for leucine enkephalin (Figure S6) or moderate concentration (8 μM) myoglobin (Figure 4d) between the two emitter positions. However, when using a high concentration (35 μM) native myoglobin sample on the Agilent 6545XT mass spectrometer (located on axis with the instrument inlet on the other side of the nESI emitter), use of the far emitter position resulted in greater competition between the heme$^{0/1+}$ loss channels upon CID. Almost all CID occurred by loss of heme^{1+} in the close position (see Figure S7). These results illustrate that effects of nESI emitter position on CID can be instrument dependent. While, for the Waters Synapt G2-S*i*, measurably different amounts of in-source activation occurred at close vs far positions for all three analytes, only small (average of < 0.5 V) differences were observed for the Agilent 6545XT for a similar distance between emitter positions for two of the three tested analytes.

Intriguingly, a large difference in CID branching ratio (heme^0 vs. heme^{1+} loss channels) on the 6545XT was observed for high- (but not low-) concentration holomyoglobin solutions with a large (~7 V) concomitant shift in CID50 (see Figure S7). This effect may be due to electrochemical oxidation in solution[212] due to the higher electric fields present in the closer emitter position, or it may be due to redox activity within weakly bound dimers at the high concentration. Brandner et al. recently reported "intrinsic native electron capture dissociation" of (heme-containing) cytochrome c, that only occurs at high (≥ 37.5 μM) concentrations and requires no deliberate collisional activation.[24] They attributed this to inter-monomer electron transfer in cytochrome c dimers somewhere within the instrument source region. Here, it appears that emitter-position-dependent activation differences on the Agilent 6545XT are insufficient to significantly affect CID of either leucine enkephalin or native holomyoglobin monomers but are sufficient to cause observable differences for holomyoglobin at high concentration. CID50 values for these experiments are summarized in Figure S8.

The Waters Synapt G2-S*i* and the Agilent 6545XT mass spectrometer (see photographs and schematics in Figure S9) have significantly different source designs, which may explain the observed differences in nESI emitter position-dependent activation. One major difference is that, inside the Synapt

G2-S*i* source, ions travel through a relatively high-conductance (~15 mm diameter) ion guide into the "Stepwave", whereas, for the Agilent 6545XT, they pass through a narrow (0.55 mm diameter, 19 cm long) inlet capillary followed by a supersonic expansion into the 4-Torr Front Funnel. The nESI potential needed for stable spray across all emitter positions on the Agilent 6545XT (1.2-1.5 kV) was slightly higher than that used on the Waters Synapt G2-S*i* (0.9-1.3 kV). Nitrogen drying gas is used in the Agilent 6545XT source, whereas no drying gas is used in these Waters Synapt G2-S*i* experiments. The range of emitter-to-inlet distances and the source temperatures (24-31 °C) used in the two sources are similar. Together, these design differences suggest that the above-described differences in CID behavior arise primarily from differences in the sharpness of the transition from atmospheric to low pressure and the amount of time ions spend beyond the source inlet at relatively high pressure in the two instruments.

Variation of protein CIU fingerprints at fixed emitter positions as measured using RMSD.

Above, it was shown that using a fixed emitter position with a single emitter can result in very low variability in CID50, CIU50, and CIU RMSD between replicates. To determine whether different emitter positions also cause different measurable in-source activation in CIU experiments, we first investigated whether RMSD for replicates using a single emitter at a fixed position varied with emitter position. Generating CIU fingerprints with low RMSD is a widely accepted criterion for high reproducibility/repeatability and is necessary to confidently distinguish structures of ions based on differences in their CIU fingerprints.

RMSD for CIU fingerprints acquired at different emitter positions were calculated to assess whether these data meet the < 5% acceptance criterion and quantify their variability. These data were collected in a same-day quintuplicate using BSA and NIST mAb (mass spectra Figures S10 and S11) as described in the Methods section. BSA fingerprints were collected in this way on 3 separate days, and NIST mAb fingerprints were collected on one day (representative data shown in Figures S12-14). Results in this section for BSA are reported as the average across those 3 days. Figure 5 summarizes the measured effects of different capillaries at positions close to and far from the instrument inlet. nESI emitter position effects on the repeatability (using a single emitter) and reproducibility (between different emitters) of CIU fingerprint replicates are measured by the RMSD calculated in CIUSuite2 for BSA (Figure 5a) and NIST mAb (Figure 5b). The average RMSD across 3 days and all 5 fixed-position replicates for BSA is less than 6% (and less than 5% for the highly-abundant 15 and 16+ charge states; see Figure 5a). The average RMSD for NIST mAb exceeds 10% for two of the low-abundance abundant native charge states (22 and 23+) under some conditions, which is outside the acceptance criterion established by Ruotolo and coworkers. However, for high-abundance charge states (25 and 26+) at both close and far positions it is less than 7% overall and for most fingerprints is less than 5% (Figure 5b).

Figure III-5. *Statistics for RMSD of quintuplicates of BSA collected on three separate days (a) and quintuplicates of NIST mAb collected on a single day (b). In (a) colored bars represent average, and error bars represent the combination of triplicate and day to day variation. In (b) colored bars represent average, and error bars represent the triplicate variation.*

Loo and coworkers observed that results from native MS experiments can to some extent depend on the “touch” of the user,[180] including tuning of emitter position and other user-tuned source conditions. Comparison of the RMSD at different emitter positions in the above experiments sheds some light on the origins of this user-dependent “touch” for nESI-IM-MS. Figure 5a shows that variability (as measured by RMSD) for BSA CIU fingerprints collected using a single emitter in each position is higher in the “close” position than in the “far” position. For NIST mAb, CIU fingerprints collected in the close position have a higher RMSD than those collected in the far position when the same emitter is used (Figure 5b). Using a single emitter in a "far" position rather than a "close" position led to more stable spray and a lower (< 2%) RMSD value for these ions in most replicates.

However, whereas single-emitter experiments show a clear influence of emitter position on CIU fingerprint repeatability, assessment of reproducibility using different emitters is more meaningful in characterizing expected variation of CIU over time within a single lab or between laboratories using the same type of instrument. For the ions studied here, exchanging nESI emitters increased the RMSD by a factor of 1-3 with respect to single emitter experiments and largely masked any differences in CIU fingerprint variability (RMSD) between the close and far positions (Figure 5). As a caution, it was observed that 1 of 8 emitters tested had an unusually large RMSD of 8.7%, while the others consistently had RMSDs below 4% (analysis with this trial excluded shown in Figure S15).

Differences in CIU fingerprints collected at different emitter positions as measured by RMSD. In addition to its uses as a metric of variability for a single analyte under a single set of experimental conditions, RMSD is also used as a metric to assess structural differences of ions prepared under different experimental conditions or differences between analytes with similar structures. Here, we apply $\mathrm{RMSD}_{\mathrm{AofP}}$ (average of all pairwise RMSD values between fingerprints in each trial acquired under different experimental conditions) and $\mathrm{RMSD}_{\mathrm{PofA}}$ (the pairwise RMSD between the average of all trials for each condition, commonly used to assess structural differences between analytes), to assess the differences between fingerprints of the same charge state collected at a close and a far position. For BSA, the $\mathrm{RMSD}_{\mathrm{PofA}}$ and $\mathrm{RMSD}_{\mathrm{AofP}}$ between the fingerprints acquired at the close and far positions are roughly twice those for data acquired at fixed positions (Figure 5a), indicating a clear effect of emitter position on CIU behavior for this ion. In contrast, due to the high RMSD between different capillaries in the far position for NIST mAb, it is less clear whether the same effect occurs for this ion (Figure 5b).

Differences in CIU fingerprints at different emitter positions as measured using CIU50. Instead of RMSD, it might seem that the more intuitive property in CIU experiments to compare to the above CID50 results for CID experiments would be the CIU50. The BSA and NIST mAb data described above were analyzed using CIUSuite2 to identify features and CIU50 of transitions for each individual trial (fit parameters in Table S2). The results of this analysis are summarized in Figure 6 for both BSA (Figure 6a) and NIST mAb (Figure 6b). For both NIST mAb and BSA a small (~2 V average, ~1 V median) shift in CIU50 is observed at a close position. This indicates the close emitter position causes more in-source activation than does the far position, in agreement with the CID results. However, the same-day standard deviation in the CIU50 due to exchanging nESI emitters was found to be 1-2 V for these replicates, and the day-to-day standard deviation was ~2 V. Thus, the shift in CIU50 between the two emitter positions was similar in magnitude to realistic variability of CIU50 caused by exchanging emitters and/or day-to-day instrument drift for the Waters Synapt G2-S*i*.

Figure III-6. *Statistics for CIU50 transitions in far (blue) and close (red) positions for BSA collected on three separate days (a) and NIST mAb collected on a single day (b). In (a) error bars represent day-to-day variation. In (b) error bars represent variation across the triplicate. Insets show box-and-whiskers plots for differences in average CIU50 measured at close and far positions for all charge states and all observed transitions. The unusually high CIU50 difference value in the inset of (a) represents data for one replicate of BSA*$^{14+}$ *with very low signal.*

One explanation for the apparently greater sensitivity of RMSD to emitter position relative to CIU50 is that the latter are determined by integrating IM-MS data over ranges of drift times corresponding to each CIU feature. This integration may average out differences in the shape of drift time distributions that explicitly increase the RMSD. Thus, RMSD (or other similar metrics that directly account for drift time distribution differences)[230] may be a more sensitive tool than CIU50 for assessing variability of in-source activation for different experimental conditions when these differences are small. There may also be a kinetic contribution, i.e., energy barriers for the observed structural transitions for these ions and internal energy required to observe them on the experimental timescale may differ.

Conclusions

The data presented here indicate that tuning emitter position between experiments can be a significant source of day-to-day and emitter-to-emitter differences between CID breakdown curves and CIU fingerprints. However, recording and using identical, micrometer-adjusted nESI emitter positions on a Waters Synapt G2-S*i* instrument can increase repeatability and reproducibility of CIU/D data. Systematically mapping the emitter-position-dependent shift in CID50 values for holomyoglobin provided a straightforward way to assess which emitter positions lead to greater in-source activation, with positions close to the instrument inlet typically exhibiting greater activation (and variability in activation) than far and peripheral positions. In contrast, emitter position was shown to have a very small influence on CID50 for most analytes on an Agilent 6545XT Q-TOF instrument. This difference between the two instruments likely arises from differences in collisional heating and cooling experienced by the ions as they pass into and through the source regions, which have significantly different pressure profiles and gas dynamics. Modeling this ion heating and cooling as a function of source design, nESI potential, and gas dynamics is the subject of future investigation.

For CIU fingerprints on the Waters Synapt G2-S*i*, RMSD values indicate that use of close vs. far emitter positions can result in measurable differences in BSA CIU fingerprints. CIU50 values, by contrast, were less useful for characterizing emitter position effects due to high variability in these values when exchanging emitters and due to instrument drift from day to day. For NIST mAb, RMSD and CIU50 differences between close and far emitter positions were both similar in magnitude to the those at fixed position between emitters and days. These results illustrate that it can be important to characterize emitter position effects on CIU/D for an analyte of interest before choosing which emitter position to use, and that acquiring replicates at a fixed position as well as recording emitter position can be useful in increasing reproducibility. To support reproducibility and traceability within and between laboratories for native IM-MS experiments, including CID/U experiments, an example table reporting nESI emitter positions and other relevant experimental settings for these data is included in the SI (see Table S1), and an associated table template is available for download on the Prell group Github website (*https://github.com/prellgroup*).

IV. AN IMPROVED IMPULSIVE COLLISION THEORY FOR DETERMINING THERMOCHEMICAL BARRIERS OF NATIVE PROTEIN COMPLEX DISSOCIATION WITH MODERN MASS SPECTROMETERS

This chapter includes co-authored material which is intended to be published with co-authors Austin Green, Kenneth Newton, Jody May, John McLean, Ruwan Kurulugama, and James Prell. Data collection, data analysis, and project conceptualization were performed by Samantha Shepherd, Austin Green, and Jody May. Development, validation, modifications, and revalidation of the command line software program IonSPA was pursued over a period of 4 years by Samantha Shepherd, James Prell, Kenneth Newton, Ruwan Kurulugama, and Austin Green. Figures were created by Samantha Shepherd and Austin Green.

Abstract

Native ion mobility-mass spectrometry (nIM-MS) can measure the dissociation and unfolding of protein ions in the gas phase to determine structural information about biological samples at all structural levels. In collision induced unfolding and dissociation (CIU and CID), the energy required for a structural change is often reported as the voltage at which 50 percent of the precursor ion has been depleted, i.e., the "CID50" ("CIU50" for unfolding transitions). The CID50 can differ between instruments due to differences in collision cell design or when collected using different settings (such as collision cell pressure) on the same instrument. Here we show that IonSPA, in-house software based inspired by Uggerud and Derrick's Impulsive Collision Theory, may be able to account for differences in CID50 caused by different pressures and between collision cell designs on different commercial instruments. Agreement with enthalpy and entropy values calculated from measured Arrhenius parameters for loss of heme from partially denatured myoglobin and for monomer loss from Shiga toxin 1 subunit B pentamer dissociation was typically about 30%, positioning IonSPA as a promising model within the context of the limited number of standards available for comparison.

Introduction

In recent decades native ion mobility-mass spectrometry (nIM-MS) has emerged as a useful tool to study the structure and behavior of many biomolecules and their complexes. Native mass spectrometry is used to transfer intact, kinetically-trapped, natively folded proteins or protein complexes[49–51,100] into the gas phase through a variety of methods, commonly via nano-electrospray ionization (nESI).[14]

Some study of these native-like protein ions can be performed without disrupting their native-like structure. However, much additional structural information can often be determined using adjuvant methods in which the native-like ions are deliberately unfolded or dissociated.[8,36,320] This includes investigation of dissociation products to determine quaternary structure[3,4,222,321] or primary structure,[111] unfolding of protein ions to evaluate tertiary structure and identify domains,[227,322] dissociation of ligands for their identification or binding location,[173,206,207,215–217,310,321,323] ion reactions,[6,9,24,102] and unfolding of protein ions to test for structural differences between highly similar proteins.[12,32–34]

These disruptions to native-like structure in order to make inferences about native protein structure are reminiscent of strategies used in the solution phase prior to the development of high-resolution biophysical techniques such as protein nuclear magnetic resonance (NMR) spectroscopy, x-ray crystallography and cryo-electron microscopy (cryo-EM). In these cases, application of a chemical or thermal denaturant to proteins in solution is used to determine the Gibbs free energy, the extent of cooperativity, and/or the relative stability by considering the amount of folded protein remaining as a function of denaturant applied.[226] Proteins ions unfolded by collision induced unfolding (CIU) often unfold via three or more states,[86] unlike in these solution phase techniques, in which often zero or only one stable intermediate state is observed. Consequently, if each transition between states can be well characterized there is a potential wealth of structural information in CIU data. Furthermore, because the gas-phase potential energy surface differs from that in solution, the observed intermediate unfolded structures are likely different from those accessed in solution, potentially yielding information about the native structure that is partly orthogonal to condensed-phase unfolding methods. These differences are due factors such as the absence of solvent, the increased strength of charge-charge and charge-dipole interactions in vacuum, and the lack of a hydrophobic driving force in the gas phase.

Extensive prior work has considered the deposition of internal energy into protein ions for the purpose of quantitating the gas-phase stability of ions, including in collisional activation (collision induced unfolding and dissociation (CIU/D)),[186,324–326] surface induced activation (SIU/D),[3] Electron Capture/Transfer Dissociation (EC/TD),[118,119,185] Blackbody Infrared Radiative Dissociation (BIRD),[99,188] and Guided Ion Beam Mass Spectrometry (GIBMS).[79,93,95]

Some techniques and some studies[71,178,327] especially those using BIRD or GIBMS, mechanisms of internal energy deposition, internal energy distributions, and reaction time of protein dissociation events have been carefully characterized to determine the enthalpy, entropy, and free energy barriers to dissociation. These methods are computationally expensive enough that they are infeasible for determining vibrational energies of moderate-sized proteins, especially over the hundreds to thousands of collisions common in modern, commercially available collision cells. In these collision cells operation pressures allow ion-buffer gas collisions to either deposit or remove energy from the ion, resulting in an ion internal energy that changes dynamically as the ion traverses the collision region. Consequently, new strategies are necessary for the evaluation of internal energy of moderate sized proteins through their reaction time within a typical modern collisional activation experiment. The Impulsive Collision Theory (ICT), developed by Uggerud and Derrick and modified by Douglas to study peptide dissociation at high collision energies, is an attractive theory to help overcome the computational bottleneck of atomistic simulations. In the ICT, only the buffer gas particle and a small region of the ion directly interacting with the gas particle need be modeled for each collision. However, the ICT does not include mechanisms for internal energy loss from the ion to the buffer gas, which is expected to occur as the hot ion begins to slow down, while continuing to undergo collisions.

In this manuscript a Monte-Carlo version of an Improved Impulsive Collision Theory (IICT), based on the ICT of Uggerud and Derrick,[191] is presented as an extension of more simplistic modeling.[186] This model is implemented in Python (Ion Simulations of the Physics of Activation, IonSPA). IonSPA is used to determine the thermodynamic dissociation barriers of two protein standards (partially denatured myoglobin and native Shiga toxin pentamer), previously studied with BIRD, using multiple collision induced dissociation on two commercially available instruments (an Agilent 6545XT quadrupole-time-of-flight, Q-TOF, and a Waters Synapt G2-S*i* Q-IM-TOF).

Methods

All peptide and protein samples were obtained from Sigma Aldrich (St. Louis, MO, USA) and used without further purification. Equine heart myoglobin (SKU: M1882) was buffer swapped using Micro Bio-spin 6 columns (Bio-Rad, Hercules, CA, USA) into 18 MΩ·cm water, which was then mixed with 20 percent methanol by volume to generate partially denatured myoglobin solutions matching solvent conditions in BIRD experiments.[128] This solution was also initially prepared at a high concentration (~100 micromolar) then diluted to a concentration more suited for nESI-MS (~10 micromolar) to reduce the prevalence of heme0 loss upon collision induced dissociation and increase that of heme^{1+} loss (to ≥ 95%). Shiga toxin 1 subunit B (SKU: SML0562) was buffer swapped into pH 7, 200 mM ammonium acetate solution and sprayed as a native (primarily pentameric) protein solution. Sample concentrations ranged from 1-25 micromolar.

Data were collected using an Agilent Collision Cell (Agilent 6545XT and 6560 Q-TOF Mass Spectrometers), a Waters Synapt G2-S*i*, and an Agilent In-Source CIU Cell (Agilent 6560 Q-TOF Mass Spectrometer). These cells use nitrogen, argon, and nitrogen mixed with ambient air and/or SF_6 as collision gases, respectively. In the Agilent Collision Cell and Waters Synapt G2-S*i* (Waters Trap) ions are accelerated by a potential difference into a collision cell (18 cm and 12.5 cm respectively) with a moderate (10^{-5} barr) pressure with the inclusion of a potential distributed across the cell (Agilent Collision Cell) and a traveling wave (T-wave) potential (Waters Trap). The Agilent In-Source CIU cell, ions are accelerated by a potential into a high (for vacuum) pressure region. The potential is placed to coincide with a supersonic expansion as the beam changes pressures dramatically entering the vacuum region of the instrument. Various specific components of these cells had to be considered to model them accurately including the potentials as a function of distance and time, pressure as a function of distance, and gas-flow dynamics. Potentials were modeled only as a function of distance for both Agilent cells which use static potentials, and as a function of both distance and time using a modified sin wave for the Waters Synapt G2-S*i*. Pressure was modeled as constant in the Agilent Collision Cell and as a constant followed by decay to a second constant in the Waters Trap due to the open region at the end of the cell. Pressures and gas-flow dynamics were explicitly calculated using Fluent for the Agilent In-Source Collision Cell. Agilent instruments are known to have a heated quadrupole region and may be more activating; consequently internal energy of ions on these instruments is modeled with a starting temperature of 400 K, rather than 298 K. Further discussion of the differences and designs of these instruments can be found discussed in prior work.[90,328]

The nESI source on both instruments was operated in positive ion mode under static nESI conditions using 1.0/0.78 mm o.d/i.d. borosilicate glass nESI emitters with filament pulled to ~2 micrometer i.d. openings using a P97 Flaming-Brown micropipette puller (Sutter Instrument, Novato, CA, USA) without further modification. nESI was initiated by applying a 0.9-1.5 kV potential to a platinum wire inserted into the solution inside of the emitter without use of an external syringe pump. Emitters were placed in “far” and “peripheral” positions relative to the inlet of the instrument,[328] as detailed in the Supporting Information (Table S1). Data for CID breakdown curves collected for thermodynamic barrier quantification were acquired by first isolating the precursor of interest, then adjusting the “CE” potential of the instrument “Trap” region (hereafter, the Injection Potential) over a range from which negligible to nearly complete dissociation is observed. The fraction of precursor remaining is calculated as the observed abundance of the precursor after CID divided by the sum of the precursor and all observed product ion abundances.

As an additional consideration to develop a more accurate model, temperature is defined as a Boltzmann distribution of internal energies centered around a particular energy. Ions that are rapidly heated through collisions would not necessarily follow a Boltzmann or Boltzmann-like distribution and therefor may not be able to be defined as at a particular ’temperature’. Prior work in determining the impact of heat capacity values also showed that ion populations follow Boltzmann-like distributions throughout their heating and cooling. Those results are used a justification for considering the ions to be 'at a temperature' in this work.

Data were analyzed using Unidec,[171] Python, MassHunter, and MHDAC (a software development kit from Agilent Technologies for reading mass spectrometry data files) to generate CID breakdown curves. These decay curves were then analyzed in IonSPA, a Python based command line entry program. Pre-analysis scripts to generate decay curves and IonSPA code are available on the Prell group Github: https://github.com/prellgroup.

The "pseudo-atom mass"[191] used in the IICT computations in IonSPA was determined computationally using molecular dynamic (MD) simulations. In each of 2000 MD simulations for each combination of ion and gas particle, a collision of a single gas particle with a single charge state of a protein was simulated in the center-of-mass frame of the ion using the all-atom AMBER99 forcefield. In total, all combinations of three gas types (helium, argon, and diatomic nitrogen modeled as a spherical particle),[329,330] three proteins (ubiquitin 5/6+, apomyoglobin 7/9+, Shiga toxin 1 B pentamer12/13+), 7 ion velocities corresponding to 5-60 V Injection Potentials for a ubiquitin 5+ ion, and three internal ion temperatures (298, 600, and 900 K) were simulated. Charges were placed on the proteins in a low-energy configuration using Collidoscope. Initial gas particle velocities was sampled from a shifted Maxwell-Boltzmann distribution to account for the asymmetry of collision velocities experience by the ion due to its lab-frame velocity. The pseudo-atom mass was calculated for each simulation based on the kinetic energies of the participants before and after the collision.

CID breakdown curves were normalized using a best-fit logistic curve to identify the asymptotes, then rescaled to set those asymptotes equal to one and zero. The fits of decay curves were weighted by a function to more heavily weight points along the slope of the decay curve and reduce influence of noise and inaccuracies along the asymtotes. When temperature is assumed to be constant, the thermodynamic barrier values can be determined through linearization of a breakdown curve using the Eyring or Arrhenius equations.[58,128,186,189] Without a constant temperature, it is necessary to use a fitting algorithm to accurately estimate the fraction of ions dissociated (or probability that ions have undergone dissociation by a given time cut-off). To determine thermodynamic barrier values, IonSPA is used to simulate breakdown curves using trial values of $\Delta H^\ddagger$ and $\Delta S^\ddagger$, and the total square error between the resulting curve and the experimental breakdown curve (weighted toward values closer to 50% dissociation) is used as a goodness-of-fit metric. This total square error is optimized over the space of $\Delta H^\ddagger$ and $\Delta S^\ddagger$ to determine a pair best-fit of values. The correlation between $\Delta H^\ddagger$ and $\Delta S^\ddagger$ generates a “fit temperature” (slope of the correlation), which is consistently similar to the maximum temperature reached at the equivalent of one lifetime (e) of dissociation or 63% dissociation. This “lifetime temperature” is used to determine a Gibbs free energy value for each dissociation reaction measured by IonSPA.

Results and discussion

Choice of standards

High-quality BIRD barrier thermochemistry values have been reported in the literature for a total of 3 noncovalent protein complex analytes (with multiple charge states): partially denatured holomyoglobin, Shiga toxin 1 B subunit pentamer (Stx1), and streptavidin. Although covalent bond dissociation thermochemistry values have been obtained with BIRD for some peptide standards, with the most studied being leucine enkephalin,[84] these typically dissociate through multiple pathways in the range of effective temperatures reached in modern commercially available collision cells,[178] considerably complicating any analysis by requiring consideration of multiple concurrent reactions. In this manuscript, partially denatured holomyoglobin and Stx1, both at multiple charge states, were ultimately chosen as targets based on the stability of these samples in neutral pH solutions on the timescale of nESI-CID-MS experiments.

To compare structural disruption between laboratories and over time a standardized, internally referenced energy metric is needed

Figure IV-1. *CID breakdown curves for dissociation of heme from holomyoglobin*$^{9+}$ *(a) shows CID breakdown curves for the dissociation of heme*$^{1+}$ *from partially denatured holomyoglobin*$^{9+}$ *on*

3 different mass spectrometers (circles), using the in-source CIU region of a modified Agilent 6560c instrument (blue), 4 different gas settings on a Waters Synapt G2-Si Trap (black), two different gas settings in an Agilent 6545XT Collision Cell (green). (b) zoomed-in data from (a) excluding the breakdown curve collected using the Agilent 6560c In-Source CIU modification.

CIU50 or CID50, the nominal Injection Potential at which 50 percent of a precursor ion has undergone a structural change, is commonly used as a metric to compare the stability of different proteins or peptides. This metric allows for comparison of samples across a single instrument operating under a single set of parameters.[12,33,219]

Figure 1 shows CID breakdown curves for dissociation of heme^{1+} from partially denatured holomyoglobin 9+ on three different instruments: a Waters Synapt G2-S*i* Trap cell, an Agilent 6560c with an in-source CIU modification, and an Agilent 6545XT/6560 Collision Cell described in the methods section. The figure also depicts breakdown curves from different pressures on the Synapt and two different IMS gas conditions: low (2 mL/min), medium (5 mL/min), and high (10 mL/min) gas flow rates with the IMS gas off, as well as a medium gas flow rate (5 mL/min) with the IMS gas on. The majority of these changes in pressures and collision cells result in changes in CID50. The Waters Synapt G2-S*i* Trap and Agilent 6545XT Collision Cell yield similar CID50s for this precursor ion despite differences in length and design. In contrast, the Agilent In-Source CIU cell operates at much higher pressure, and ions are dissociated by accelerating them over a very short distance through a supersonic expansion. The considerable differences in temperature reached and time spent offer a potential explanation of the different CID50 values (Figure 1a, blue vs green and black curves) measured with this instrument.

An ideal development in CIU/D standardization would allow for comparison of the stability of proteins, peptides, protein complexes, and protein-ligand complexes between instruments, pressure and Injection Potential settings, laboratories, and to future values and literature standards. As new CID and CIU cells are developed and more widely used, resulting in an even greater variation in measured CID50 values,[90] there is a growing need to model ion internal energy (an intrinsic value with a direct connection to dissociation/unfolding kinetics) as a function of time, rather than relying on Injection Potential (or nominal initial lab-frame kinetic energy, $z\ ^{\text{x}}$Injection Potential).[35,90,186] Given the complex relationships between thermodynamic barriers for dissociation/unfolding, nominal Injection Potential, gas temperature, ion internal energy, and observable kinetic window influencing the observed extent of reaction, it is useful to develop and validate a “universal” method for determining the thermodynamic barriers by accurately describing the internal energy and dissociation/unfolding of precursor ions as a function of instrument design and experimental parameters. Because, for a given internal energy, the thermodynamic barrier an ion must overcome in CID/U to undergo a given structural change should be the same on any instrument. The utility of measuring thermodynamic barriers has been recognized within mass spectrometry; barriers have been measured for a small number of proteins and protein complexes using BIRD,[58,128,189,235,331] a number of peptides and metal-ligand complexes using GIBMS,[93,332] and some peptides using SID.[29,71,178,209] However, these measurements have typically required computationally expensive *ab initio* modeling of ion structures and vibrational states as well as Rice-Ramsperger-Kassel-Marcus (RRKM) modeling of observed dissociation kinetics, both of which can be prohibitively expensive to apply to large ions, such as proteins and protein complexes.

The Improved Impulsive Collision Theory (IICT) reasonably models ion internal energy through ion activation in modern commercially available instruments

To overcome much computational expense in modeling ion heating, cooling, and dissociation, we use an Improved Impulsive Collision Theory (IICT) based on the Impulsive Collision Theory introduced by Uggerud and Derrick and developed further by Douglas for small molecular ions and peptides.[191,228] In both models, it is assumed that each collision between an ion and a buffer gas particle can be treated as a locally elastic collision of the gas particle with a small portion of a peptide (the "pseudo-atom", Figure 2a-c). This may cause the pseudo-atom’s kinetic energy with respect to the center of mass of the whole protein ion (i.e., its vibrational energy) to increase, decrease (IICT only), or stay the same. If the pseudo-atom’s vibrational energy does increase or decrease, some of the kinetic energy of the gas particle-pseudo-atom collision is thus transferred into (Figure 2c) or out of (Figure 2g), respectively, the pseudo-atom. After the collision, it is assumed that vibrational energy of the pseudo-atom is redistributed throughout the whole ion according as a microcanonical ensemble before the next collision occurs (Figure 2d). This is justified by the typical timescale between collisions in typical CIU/D experiments (nanoseconds) as compared to the very fast internal vibrational energy redistribution timescale of proteins (picoseconds or less).

It is further assumed that, because the protein is large compared to the pseudo-atom, the statistics of vibrational energy associated with the region of the ion involved in the rate-limiting step for dissociation/unfolding (Figure 2e) follow an approximately canonical ensemble at an effective temperature identical to that at which the ion would have an average internal energy equal to the microcanonical energy. Because the rate-limiting step likely involves making and/or breaking a small number of bonds, this should be justified for protein-sized ions, which contain many thousands of bonds. The ion's kinetic energy also changes due to the momentum transferred in the collision and applied external electric fields. This process continues for each collision (typically hundreds to thousands in CIU/D experiments) until the ion exits the collision region. It should be noted that the mass of the pseudo-atom, assumed to be constant for a given ion-gas particle relative velocity and ion internal energy before the collision, is mathematically related to, and can be thought of as determining, the average “efficiency” of collisional energy transfer.

Emphatically, the IICT does not require assigning a specific location on the ion for each collision with buffer gas; instead, only the ion and gas particle masses and velocities, ion internal energy, and a random collision geometry are used to model the collision. In this manner, many thousands of sequential collisions for each of a large population of ions can be efficiently simulated without the very high cost of atomistic MD simulations. Although it is likely that many collisions transfer energy in and out of rotational modes of the ion, these are typically expected to play a weak role in dissociation/unfolding of protein-sized ions, and the total rotational energy of the ion after its translational energy should be much smaller (by a factor of $\sim 3/(6n) = 1/(2n)$, where n is the number of atoms in the ion) than the total vibrational energy of the ion. The IICT therefore ignores ion rotational energy, which would add significantly to computational complexity with little effect on dissociation/unfolding kinetics.

Importantly, in modern commercially available collision cells, a sufficient number of collisions occur that it is likely ions are not only heated by collisions (as in the original ICT), but also cooled to varying extents (Figure 2f-h). This occurs via super-elastic collisions when the ion’s internal energy is well above the thermal kinetic energy of the gas. Additionally, the pseudo-atom mass, which was modeled in the original ICT to be roughly 32 Da for peptides in argon gas, differs for larger proteins and varies as a function of both temperature and kinetic energy (Figure 3).

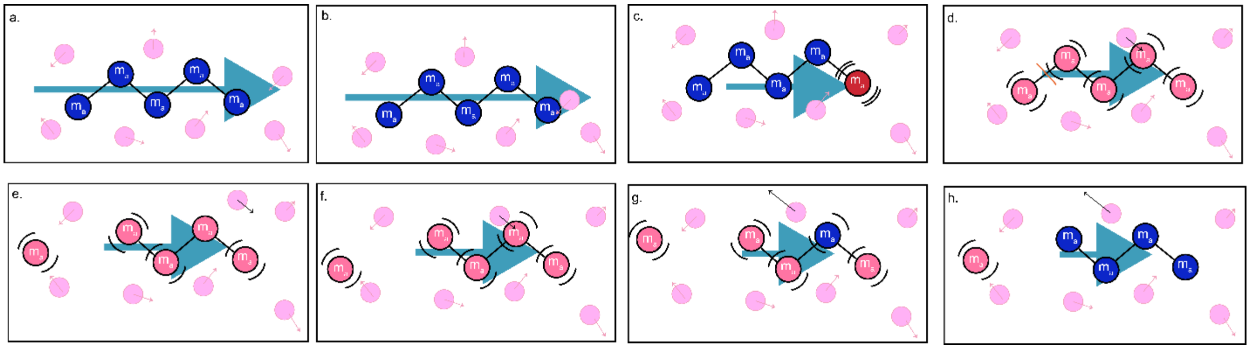

Figure IV-2. Schematic cartoon representing key steps in the IICT (Improved Impulsive Collision Theory). (a) shows an ion traveling at a high velocity into a collision cell with buffer gas (pink), (b) shows a gas molecule colliding with a portion of the ion, i.e., a pseudo-atom (with mass m_a*), (c) shows the energy from the collision being transferred to internal (vibrational) modes of the ion or the elastic collision between the pseudo-atom and gas molecule, (d) the increased vibrational energy is distributed through the analyte, potentially causing dissociation/unfolding (e). (f) After many such collisions, after the ion’s laboratory-frame kinetic energy has substantially decrease and it has high vibrational energy, an additional collision also occurs. (g) This collision removes vibrational energy from the pseudo-atom participating in the collision, and (h) the vibrational energy is again redistributed through the analyte now resulting in overall reduced vibrational energy.*

Figure IV-3. Fits of pseudo-atom mass based on MD simulations. (a) shows a linear piecewise fit of the average pseudo-atom mass at varying temperatures along the x-axis (b) show a linear

piecewise fit of the average pseudo-atom mass at varying ion velocities, and (c) shows a planar piecewise fit of ion velocity along the x-axis and ion temperature along the y-axis.

The pseudo-atom mass appropriate for protein ions was fit in the IICT using atomistic molecular dynamics simulations. Initial relative velocities between the gas particle and ion were selected randomly from a skewed Maxwell-Boltzmann distribution to account for the lab-frame kinetic energy of the ion, and collision geometries were selected isotropically. (A representative simulation "movie" of a gas-ion collision and associated screenshots are included in the Supporting Information.) The velocities of the gas and ion before and after the collision, as well as the change in vibrational energy of the ion, were determined from each simulated collision to determine the single-collision energy transfer efficiency factor, χ, which is related to the pseudo-atom mass (m_a) and gas particle mass (m_g) according to the following equation:

$$\chi = 4\frac{m_a m_g}{(m_a + m_g)^2}$$

The resulting trajectory-specific m_a values were averaged over all simulated collisions to yield a final, optimized m_a value for each combination of protein ion and gas identity, initial ion lab-frame kinetic energy, and initial ion vibrational temperature. Figure 3 summarizes a piecewise fit of pseudo-atom mass using argon as a collision gas found to provide the strongest agreement. The projection of the fit on the effective temperature (Figure 3a) and ion velocity axes (Figure 3b) are shown in Figure 3. A piecewise, planar fit is shown in Figure 3c. In two previous reports describing determination of thermodynamic barriers from CIU/D experiments, barrier values were calculated under the assumption that the ion quickly reached a maximum temperature and cooled very little, permitting the application of constant temperature Eyring and Arrhenius equations.[102,186]

In the more detailed IICT, ion cooling beyond the internal temperature maximum is explicitly included to more realistically represent ion temperature in modern CIU/D instrumentation (Figure 4). The IICT predicts that the gas pressure and cell design (e.g., use of traveling waves (Waters Trap, Figure 4c,d) vs. static electric fields (Agilent Collision Cell, Figure 4a,b)) can influence the maximum internal temperature of the ion, the time the ion spend close to its maximum internal temperature, and the time the ion takes to traverse the cell.

Using the IICT and models for the Waters Synapt G2-S*i* Trap cell, the Agilent 6545XT Collision Cell, and the Agilent 6560c In-Source CIU region, the effective temperature of the analytes over time align with qualitative observations (Figure 4). The Agilent 6560c In-Source CIU region, which requires very high Injection Potentials (up to ~450 V) to observe unfolding and/or dissociation of protein ions, heats protein ions to very high temperatures (in excess of 1000 K for holomyoglobin^{9+}, Figure 4e) for a short amount of time (on the order of 10 microseconds). Due to the short time spent above the reaction threshold temperature the kinetic shift is exceptionally high, thus the ions must be accelerated very forcefully to reach much higher temperatures in order to observe structural changes within the kinetic window. For example, for holomyoglobin^{9+}, the CID50 for heme^{1+} loss is approximately 200 V, corresponding to a nominal initial ion kinetic energy of ~1800 eV in the lab frame, whereas the activation energy near 400 K of this CID pathway has been measured by BIRD to be 0.8 eV. CID50 for the same analyte on both the Synapt G2-S*i* Trap cell and Agilent 6545XT Collision Cell are much lower (10-45 V, corresponding to nominal initial kinetic energies of ~90-400 V, depending cell type and gas pressure), due to the much longer time for which the ion internal energy remains high for these cell designs. Additionally, ion internal temperature vs. time curves modeled in IonSPA for the Agilent Collision Cell as compared to the Waters Trap are much more similar to each other than they are to the Agilent In-Source CIU region. These results illustrate the utility of IonSPA for understanding the underlying causes of similarities and differences in CID breakdown curves for the same ions on different instrumentation.

Figure IV-4. *Temperature vs. time curves showing the effective temperature of the holomyglobin 9+ ions throughout their trajectory under 5 different conditions: high pressure (gas flow rate 22 psi) on an Agilent 6545XT collision cell (a), low pressure (gas flow rate 15 psi) on an Agilent 6545XT collision cell (b), high pressure (gas flow rate 10 mL/min) on Synapt G2-Si (c), low pressure (gas*

flow rate 2 mL/min) on Synapt G2-Si (d), and a single trajectory of a holomyoglobin 9+ ion on an Agilent In-Source Collision Cell (e). The traveling wave has a wave velocity of 300 m/s and a wave height of 4 V.

Enthalpy and entropy values calculated with IonSPA can show moderate to high precision in determination across pressures and instruments.

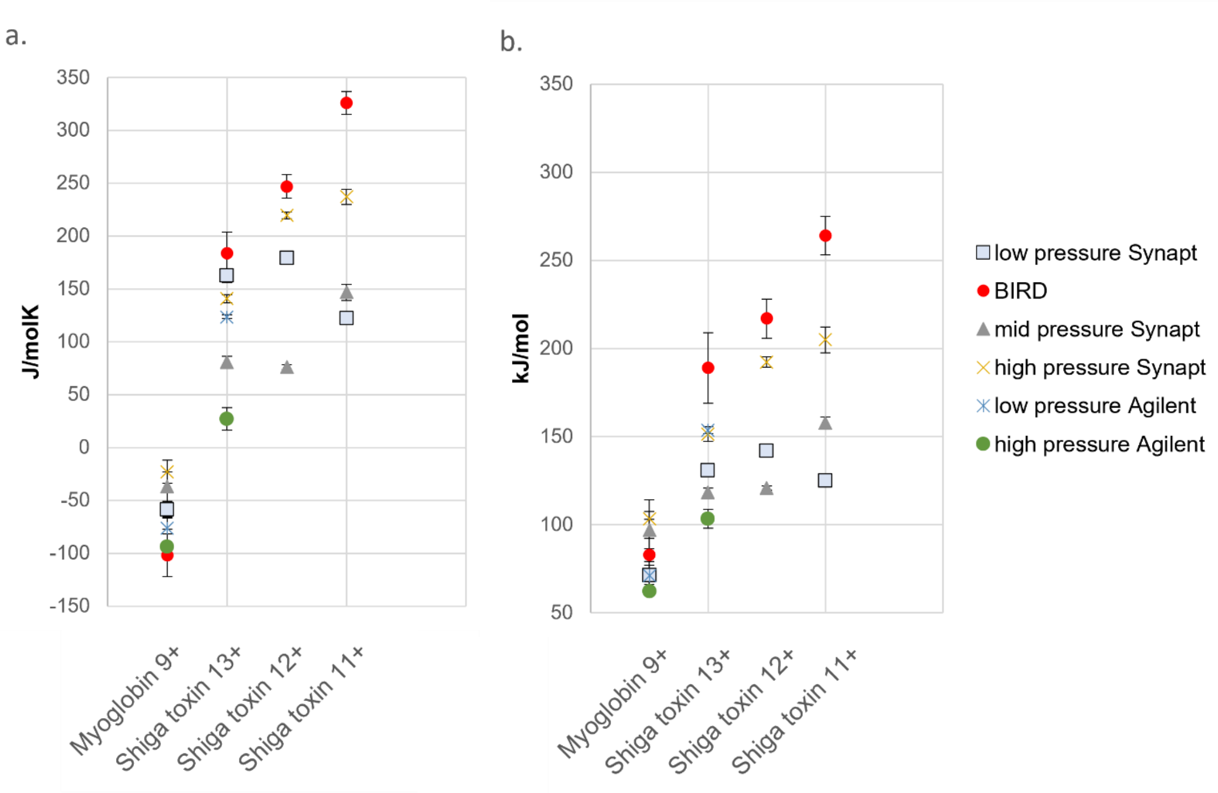

Figure IV-5. Thermodynamic barriers determined by IonSPA. Entropy (a) and enthalpy (b) of heme dissociation from mygolobin 9+ and monomer dissociation from Shiga toxin 11-13+ determined by IonSPA for low, medium, and high gas flow rates in a Waters Synapt G2-Si Trap cell and for low and high gas flow rates in an Agilent 6545XT Collision Cell.

To assess the precision and flexibility of the IonSPA model across different experimental conditions and instrument designs, data were collected and analyzed using IonSPA on both the Water Synapt G2-S*i* and the Agilent 6545XT Q-Tof Mass Spectrometer at multiple pressures (Figure 5) for the characterized standards of holomyoglobin and Shiga toxin pentamer.[58,128,186] If the models of the cells are an accurate reflection of experimental conditions, data collected under different experimental conditions should result in the same determination of enthalpy and entropy barriers.

Enthalpy and entropy values calculated with IonSPA show moderate agreement with BIRD values.

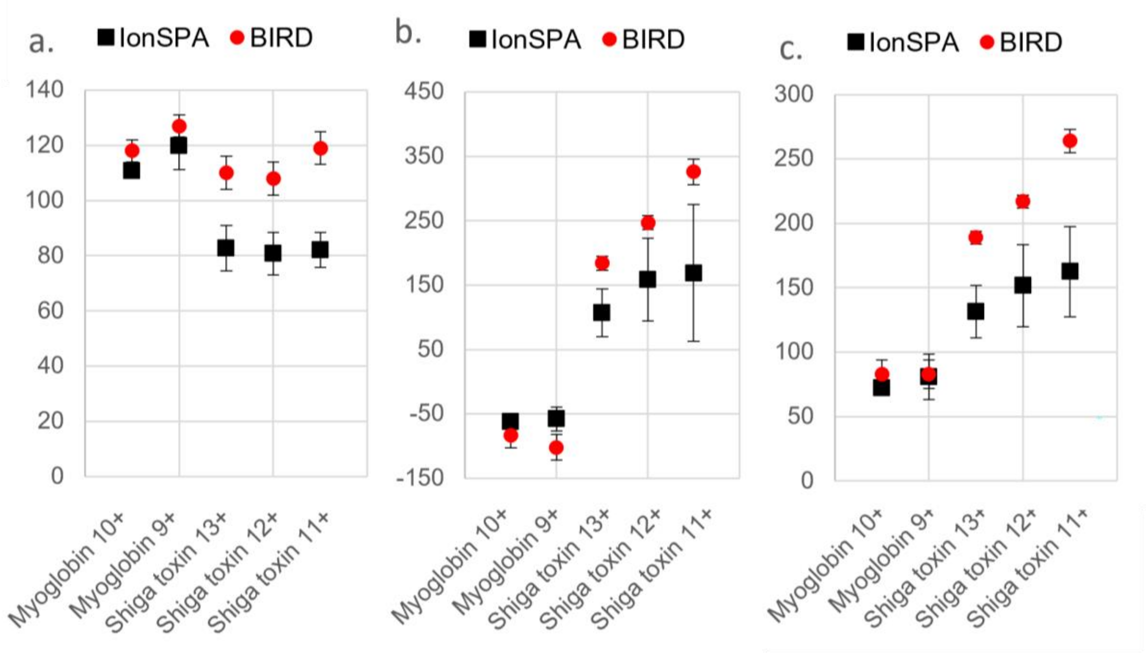

Figure IV-6. *Overall thermodynamic barriers determined by IonSPA. The enthalpy (a) and entropy (b) agreement between BIRD, Synapt, and Agilent Collision Cell experiments and modeling. Myoglobin 10+ Synapt and Shiga toxin 11+ Synapt are triplicate measurements collected at a single pressure on single day. All other measurements are the averages of multiple pressures and/or measurements made on multiple days. Error bars represent one standard deviation of each datasets determined barrier values.*

The data presented in Figure 5 was averaged to determine an overall agreement between IonSPA and BIRD data. The Gibbs free energy (Figure 6A) was calculated using the "lifetime temperature" (described in methods) for IonSPA barriers and using the median reported temperature for BIRD data. Best-fit values are shown in Figure 6A-C for CID of holomyoglobin$^{9\text{-}10+}$ and Stx$^{11\text{-}13+}$. Qualitatively, the fitted values (i.e., all entropy (Figure 6B), and enthalpy (Figure 6C) barriers are of the same sign as the previously reported BIRD values. Quantitatively, all enthalpy and entropy barriers determined using

IonSPA are systematically low from the BIRD values by 14-50% (14-30% myoglobin; 22-50% Shiga toxin, mean: 30%).

Despite the difference in their magnitude, the values determined in this study follow similar trends as a function of charge state and ion identity. This underestimation as compared to BIRD may be due to a variety of factors, including underestimation of ion temperature in IonSPA; overestimation of ion temperature in BIRD experiments; inaccurate pressure estimation; ion pre-activation or post-activation before or after the Trap region;[13,69,333] or assumptions within the Eyring equation. In the case of overestimates in BIRD, this could be assessed in a future work by shifting the data presented in the BIRD studies to a lower temperature by 20-50 K, which would reduce both the enthalpy and entropy barrier values determined from those data. Pre- and post-activation can also be studied in future work by expanding the model to explicitly include cells before and after the collision cell or, for pre-activation, increasing the initial temperature of the ion.

	Enthalpy	Entropy	T_{max} at 1/e	T_{fit}
myoglobin 9+ Synapt	91 ± 16	-40 ± 18	636	604
myoglobin 9+ Agilent	67 ± 7	-85 ± 12	710	720
myoglobin 9+ BIRD	87± 10	-102± 20	429^	--
Myoglobin 10+ Synapt	72 ± 2*	-62 ± 3*	614	578
myoglobin 10+ BIRD	83 ± 11	-84 ± 20	429^	--
Shiga toxin 11+ Synapt	163 ± 35	169 ± 53	468	454
Shiga toxin 11+ BIRD	264 ± 9	326 ± 20	135^	--
Shiga toxin 12+ Synapt	152 ± 32	158 ± 64	450	443
Shiga toxin 12+ BIRD	217 ± 5	247 ± 11	135^	--
Shiga toxin 13+ Synapt	134 ± 15	128 ± 37	440	426
Shiga toxin 13+ Agilent	128 ± 28	75 ± 53	508	497
Shiga toxin 13+ BIRD	193 ± 5	184 ± 11	135^	--

*data collected at a single pressure and on a single day in triplicate

^middle temperature used for BIRD

Table IV-1. *Enthalpy, entropy, Gibbs Free Energy, and Temperature determined by IonSPA* for *holomyoglobin and Shiga toxin protein standards on a Waters Synapt G2-Si and Agilent 6545XT mass spectrometer compared to enthalpy and entropy values calculated from BIRD activation energies and Arrhenius prefactors.*

Consideration of Uncertainty.

The primary contribution to uncertainty comes from the experimental measurements themselves, which can vary in CID50 due to insufficiently soft ionization conditions, due to instrument drift, due to emitter identity, unstable nESI spray, or by as much as 8 V due to emitter position. These data also suggest the precision of the model is heavily influenced by the signal-to-noise ratio of the mass spectra and the resulting noise along the breakdown curve. This is likely due to at least two aspects of fitting influenced by noise in the breakdown curve: 1) challenges fitting noisy sigmoids (noise at the 1 and 0 asymptotes) and 2) slight shifts in the sigmoid due to noise in the points along the slope. Based on triplicate measurements taken from these low signal to noise data the standard deviation reaches as high as 40 kJ/mol (J/molK for entropy).

The model itself is very precise with tuning of the parameters, random noise in a moderate sample size, and fit error contributing uncertainties of ~3 kJ/mol to enthalpy barriers. As is also typically the case when fitting experimental dissociation rates measured at different temperatures to an Arrhenius plot, errors in fitting $\Delta H^{\ddagger}$ and $\Delta S^{\ddagger}$ to data with noise are strongly correlated. This is illustrated in Fig. 7 by ellipses centered around the best-fit values. Uncertainty along the major axis of the ellipse is high, and uncertainty along the minor axis is much lower. A second major source of uncertainty is introduced comes from inaccuracies in modeling the physical characteristics of the collision cells and buffer gas. We also estimate that combined uncertainty in buffer gas pressure, inaccuracies in modeling pressure gradients and flow, effective collision cell length, and electric fields is ~10 kJ/mol (respectively, ~10 J/mol K) for the modeled enthalpy (entropy) barriers. . Adding this in quadrature to the estimated fitting uncertainty yields a combined uncertainty estimate of ~11 kJ/mol (respectively, ~11 J/mol K) for the IonSPA-determined enthalpy (entropy) barriers from these sources. Combination of these uncertainties results in a total uncertainty of 43 (k)J/mol(K) across all three (IICT and fitting, collision cell model, experimental) layers.

Conclusion

To summarize these results, IonSPA software, which uses an Improved Impulsive Collision Theory, can be used to model ion internal vibrational energy (and temperature) as a function of experiment time and distance in common, commercially available instruments using a python based command line software (IonSPA) available on github. Using IonSPA to model CID of partially denatured holomyglobin and native Shiga toxin 1 subunit B pentamer resulted in determined enthalpy and entropy barriers with a precision of 15-50%, as measured by agreement between different pressures. Overall, these values agree with values for literature standards measured by BIRD on FT/ICR mass spectrometers within 50% (mean including 3 charge states of Shiga toxin and 2 charge states of partially denatured myoglobin: 30%). This agreement is remarkable, considering the very different kinetic shifts and timescales of BIRD (seconds, determined as a function of time and a constant temperature) and CID (microseconds, determined primarily as a function of acceleration voltage generating a nonlinear response of temperature over reaction time) experiments on these instruments. These data are systematically shifted, most obviously for Shiga toxin, with the relationship between charge states retained, but the values considerably lower as compared to BIRD measurements. The extent of this can be assessed in a future work through study of pre- and post-activation alongside assessment of the impact of shifted temperatures in BIRD data on determined enthalpy and entropy barrier values.

The IICT and its implementation in IonSPA software are poised to be effective tools to facilitate comparison and interpret intentional structural disruption via CIU/D on different instruments and between laboratories. Major remaining challenges for the accuracy and precision of the model include accurate modeling of instrumentation and gas properties, especially in cases where detailed design specifications are unavailable. Benchmarking against data collected on homebuilt instrumentation with known design specifications or on commercial instrumentation with vendor-provided specifications may mitigate some of these uncertainties. Tuning of the IICT model is also limited by the very small number of BIRD standards available for protein ions and other large ions. This paper also introduces the IICT and this models precision and accuracy support that the IICT is a somewhat realistic set of assumptions to describe multiple sequential collisions, which may be able to be further improved upon.

The current implementation of the IICT in IonSPA exhibits relatively good precision, including across two instruments with different collision cell designs, but poorer accuracy. This makes IonSPA primarily useful for comparing modern CID data to other modern CID data. As an example: myoglobin 9+ at low pressure and Shiga toxin 11+ at high pressure have similar CID50 values, but when modeled significantly different thermodynamic barriers are determined. However, acquisition of additional high-quality CID data for a much broader variety of protein ions, as well as in different laboratories and on different instruments, will facilitate global optimization of temperature correction factors (which will have a similar effect to pseudo-atom mass correction factors).

V. OUTLOOK

In this dissertation I expand on previous efforts[186] from the Prell group to quantitate the internal energy of time of reaction of ions in modern commercially available mass spectrometers. This work is also an extension of efforts to quantify internal energy in mass spectrometry over the past 50 years in various specialized instruments and simulations. Native mass spectrometry has emerged as a valuable tool for the identification of, behavior of and differentiation between biological structures in the last 20 years. However, the data analysis methods available without quantitation of the internal energy and thermodynamic barriers of protein unfolding and dissociation are limited and cannot access the potential wealth of information contained in the shape of these reactions nor compare these reactions across time, instrument conditions, or labs. This effort provides a tool capable of comparison between results under different instrument parameters and with tuning of the Agilent collision cell model is likely to allow comparison of reactions on different collision cell designs providing a considerable update to standardization of protein activation energetics in native mass spectrometry.

In this dissertation I cover application of our previous quantitation effort to the nonspecific binding of lipid head group analogues in an attempt to build an understanding of gas-phase artefacts as compared to specific binding of lipids to proteins in characterization by mass spectrometry (Chapter II). I then turn to characterization of reproducibility of energetics of ions prepared by nESI as a function of emitter position to understand the uncertainty present in “best case” and “worst case” energetics measurements using the standard quantitation metric of CIU/D50 (Chapter III). Finally, I present an improved impulsive collision theory (IICT) as applied to internal energy deposition from hundreds collisions between buffer gas and protein ions to show that a viable model (IonSPA) has been produced (Chapter IV).

Moving forward off of these efforts there are a few broad next steps: 1) Characterize fundamentals (of pseudo-atom mass, instrument design, and nESI), 2) develop and expand collision cell models (including new cells, sequential cells, and updated cells), 3) characterize pre-activation or activation shifts, 4) further validation and benchmarking of the model alongside generation of a database of standards, and 5) application of IonSPA to interesting biological systems. Most of efforts could be pursued concurrently and some are already underway within the Prell group. Of particular interest to me is the application of this model to interesting biological systems. As the slope of a transition relates to the cooperativity of that transition in condensed phase unfolding the same may be true in the gas phase and could be used to understand the relationship between folded structures. The energy of unfolding is likely related to the number of hydrogen bonds and other noncovalent interactions disrupted by unfolding and may therefor be related to the interface area between two structures. Determination of this interface area could provide a constraint for molecular dynamics simulations. Additionally these energetics measurements could be applied to protein-ligand interactions to characterize the strength (as has been done by CID) in a way which can be compared across laboratories and across time, as well as potentially providing structural insights from the thermodynamic barrier values. Further analysis of this model and its capabilities will be necessary to implement these applications, but this model suggests exciting potential for the understanding of and comparison between energetic measurements in native (ion mobility)-mass spectrometry.

APPENDICES

A. SUPPORTING INFORMATION FOR LIPID HEAD GROUP ADDUCTION TO SOLUBLE PROTEINS FOLLOWS GAS-PHASE BASICITY PREDICTIONS: DISSOCIATION BARRIERS AND CHARGE ABSTRACTION

Theory and Data Analysis

A linearized form of the Eyring equation was used to determine activation enthalpies and entropies:

$$\ln\left(\frac{-\ln\frac{[R]}{[R+P]}}{T}\right) = -\frac{\Delta H^{\ddagger}}{k_B T} + \ln\frac{k_B}{h} + \ln t + \frac{\Delta S^{\ddagger}}{k_B} \tag{1}$$

where R denotes the precursor ion, and P denotes the product ion, T is the effective temperature of the precursor ion, k_B is the Boltzmann constant, h is Planck's constant, t is the reaction time, $\Delta H^{\ddagger}$ is the activation enthalpy, and $\Delta S^{\ddagger}$ is the activation entropy.

These values were used to compute the left-hand side of Equation 1, which was plotted against the reciprocal of effective temperature multiplied by the Boltzmann constant. The slope and intercept were then used to determine $\Delta H^{\ddagger}$ and $\Delta S^{\ddagger}$, respectively, using Equation 1. $\Delta G^{\ddagger}$ was determined from $\Delta H^{\ddagger}$, $\Delta S^{\ddagger}$, and the average effective temperature over the range of data included in the fit.

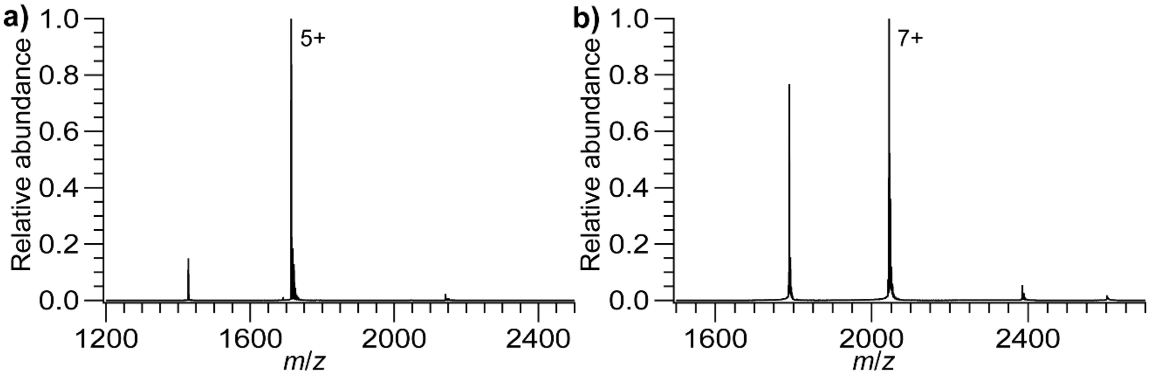

Figure A-S1. Mass spectra of (a) ubiquitin (Ubq) and (b) lysozyme (LZ). For both proteins, the most abundant charge state, which was used for CID experiments, is labeled.

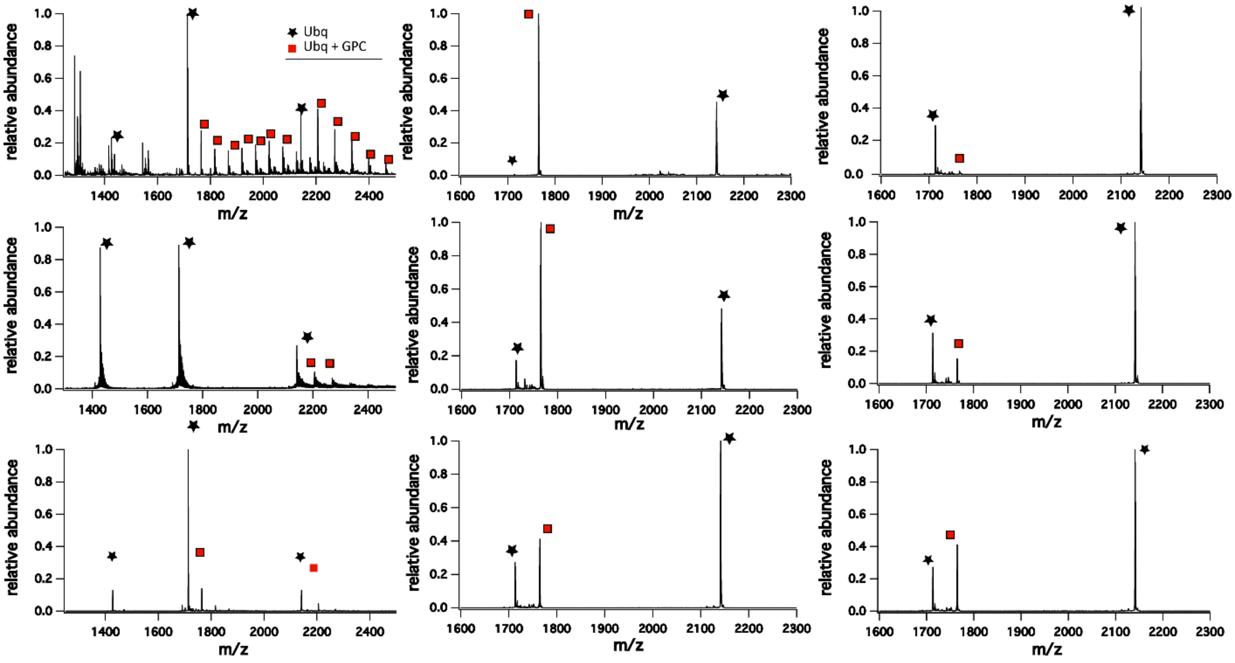

Figure A-S2: Mass spectra of Ubiquitin and GPC, left column is no isolation, middle column is isolation and low activation, right column is isolation and high activation.

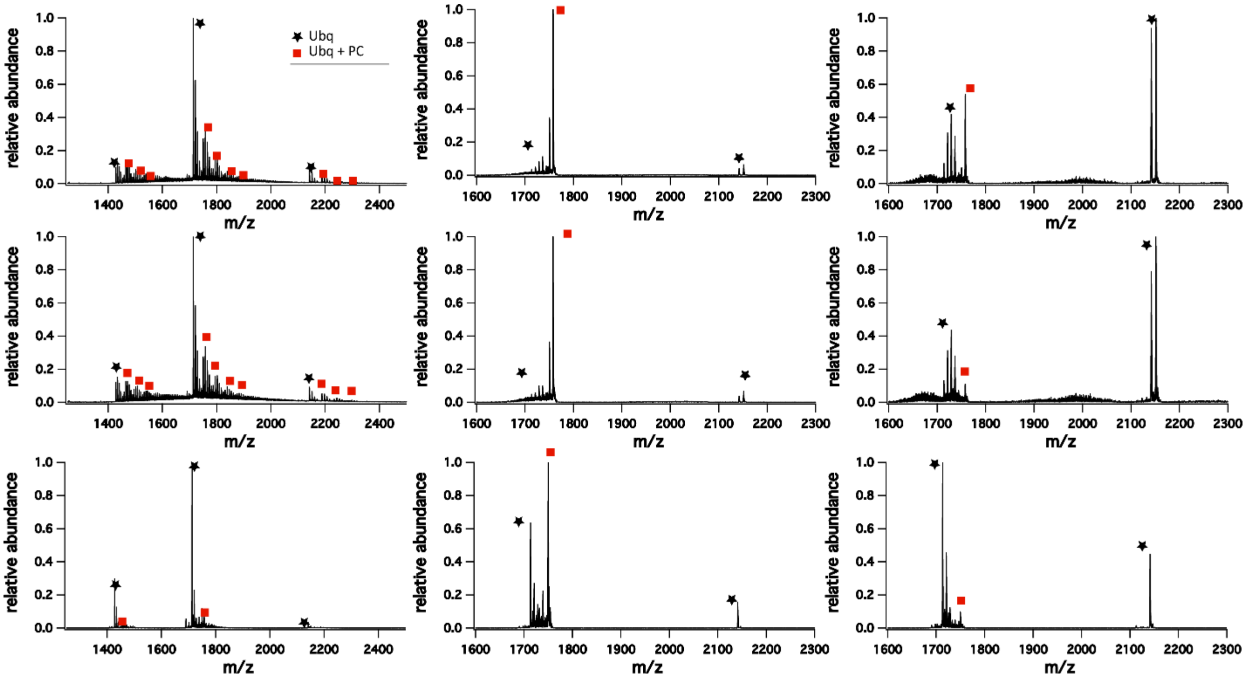

Figure A-S3: Mass spectra of Ubiquitin and PC, left column is no isolation, middle column is isolation and low activation, right column is isolation and high activation.

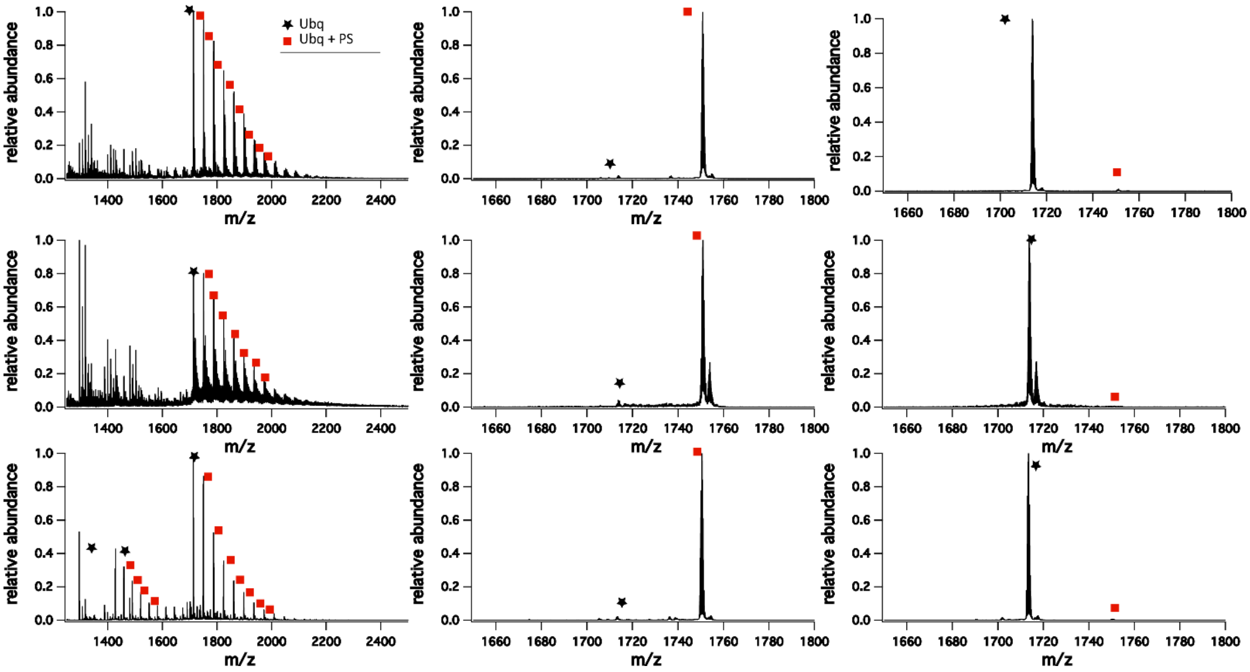

Figure A-S4: Mass spectra of Ubiquitin and PS, left column is no isolation, middle column is isolation and low activation, right column is isolation and high activation.

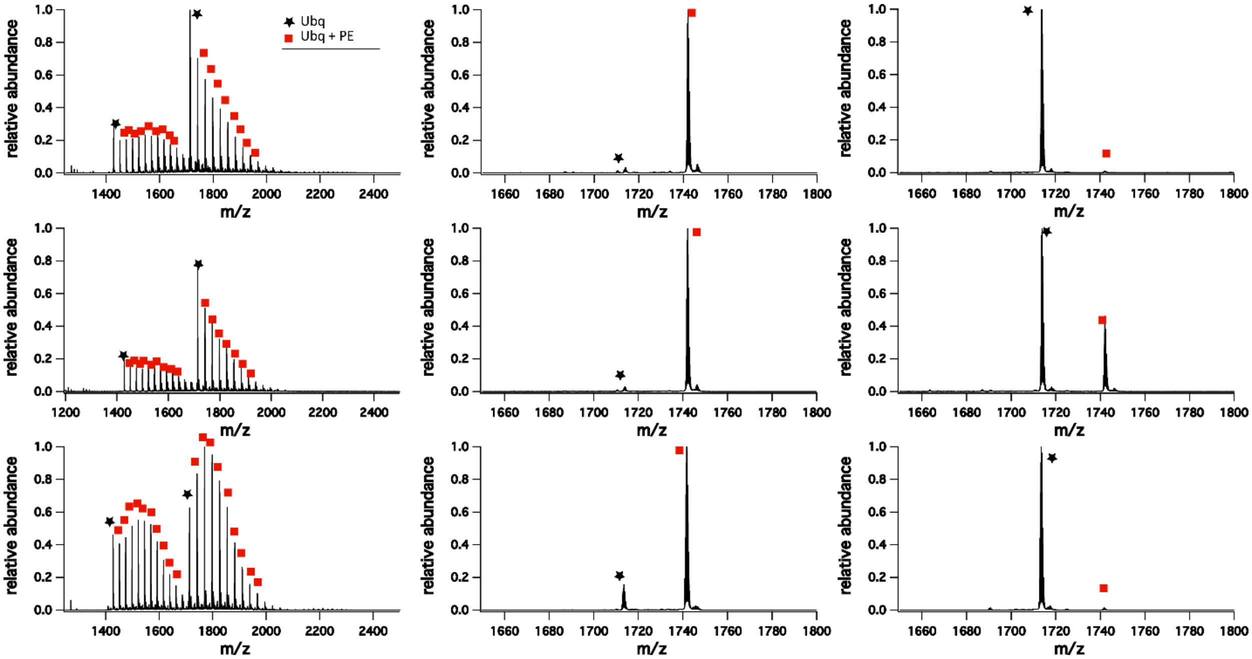

Figure A-S5: Mass spectra of Ubiquitin and PE, left column is no isolation, middle column is isolation and low activation, right column is isolation and high activation.

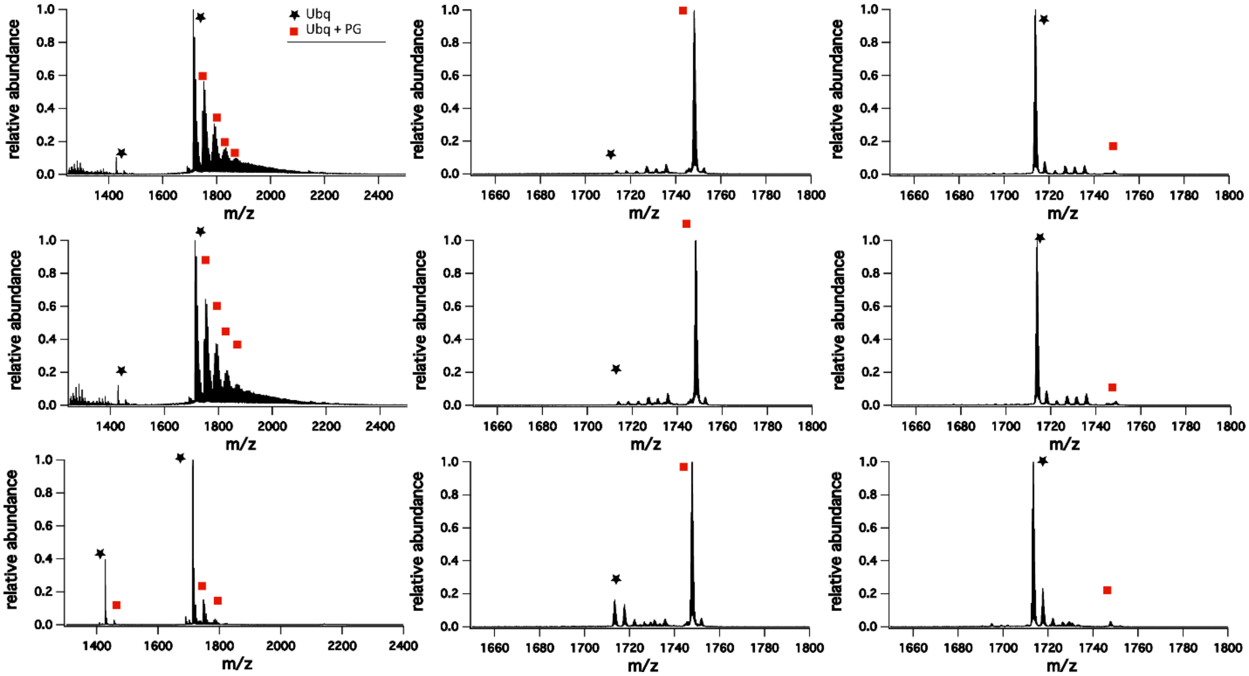

Figure A-S6: Mass spectra of Ubiquitin and PG, left column is no isolation, middle column is isolation and low activation, right column is isolation and high activation.

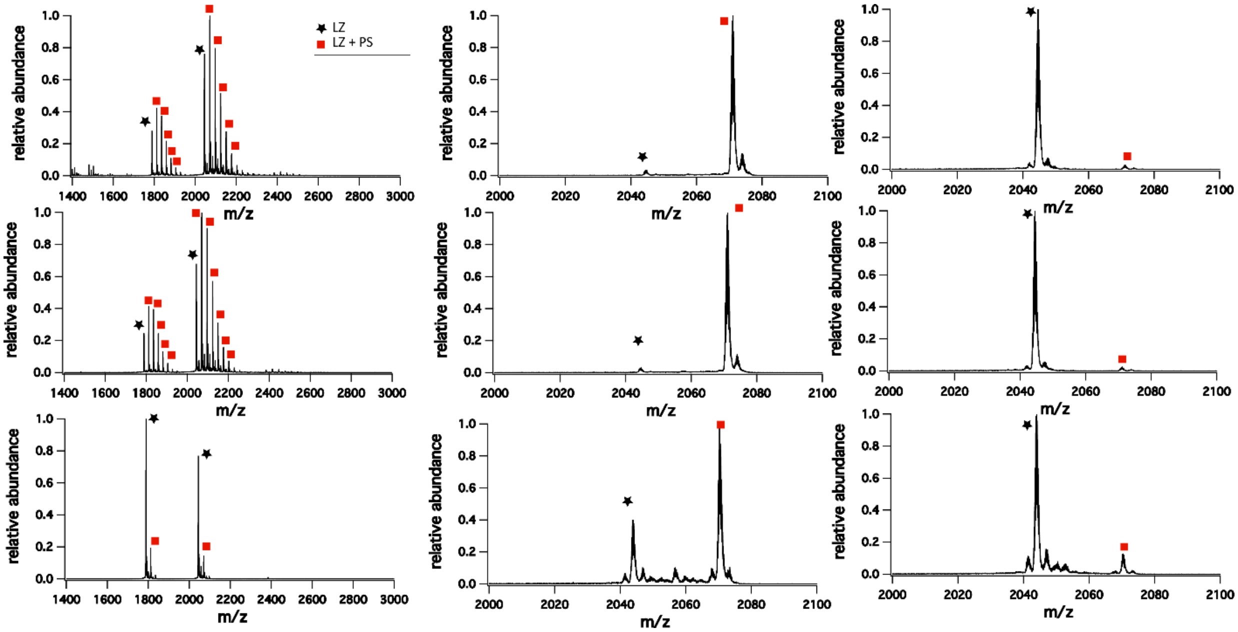

Figure A-S7: Mass spectra of Lysozyme and PS, left column is no isolation, middle column is isolation and low activation, right column is isolation and high activation.

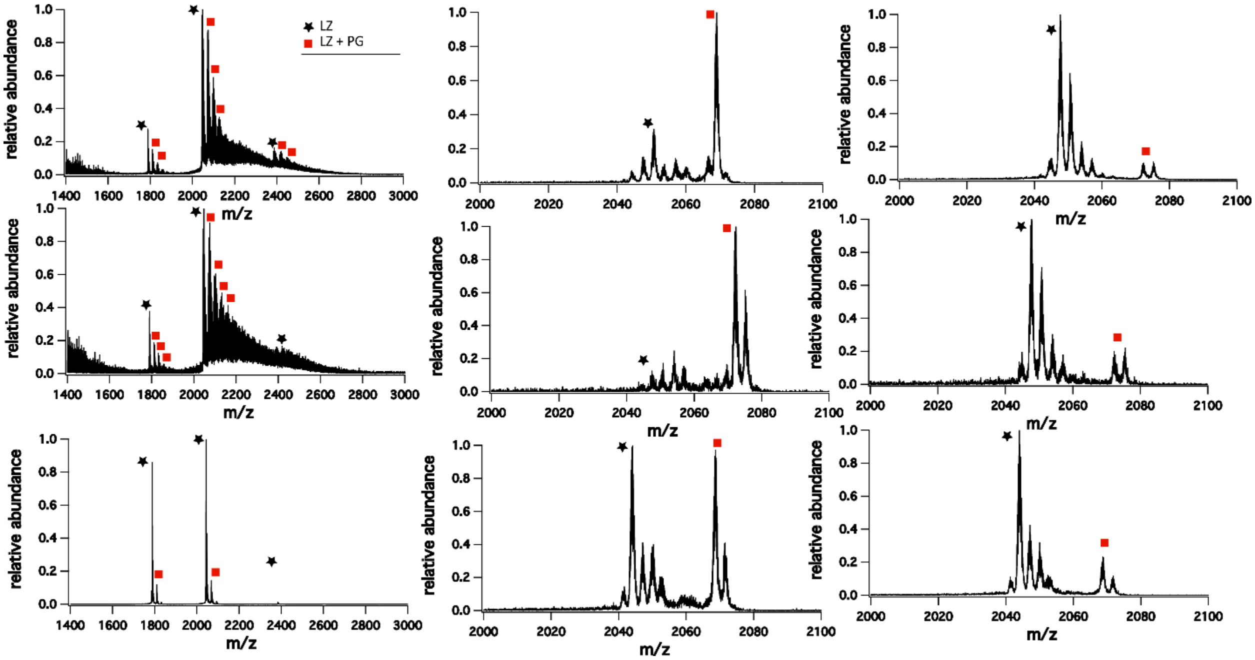

Figure A-S8: Mass spectra of Lysozyme and PG, left column is no isolation, middle column is isolation and low activation, right column is isolation and high activation.

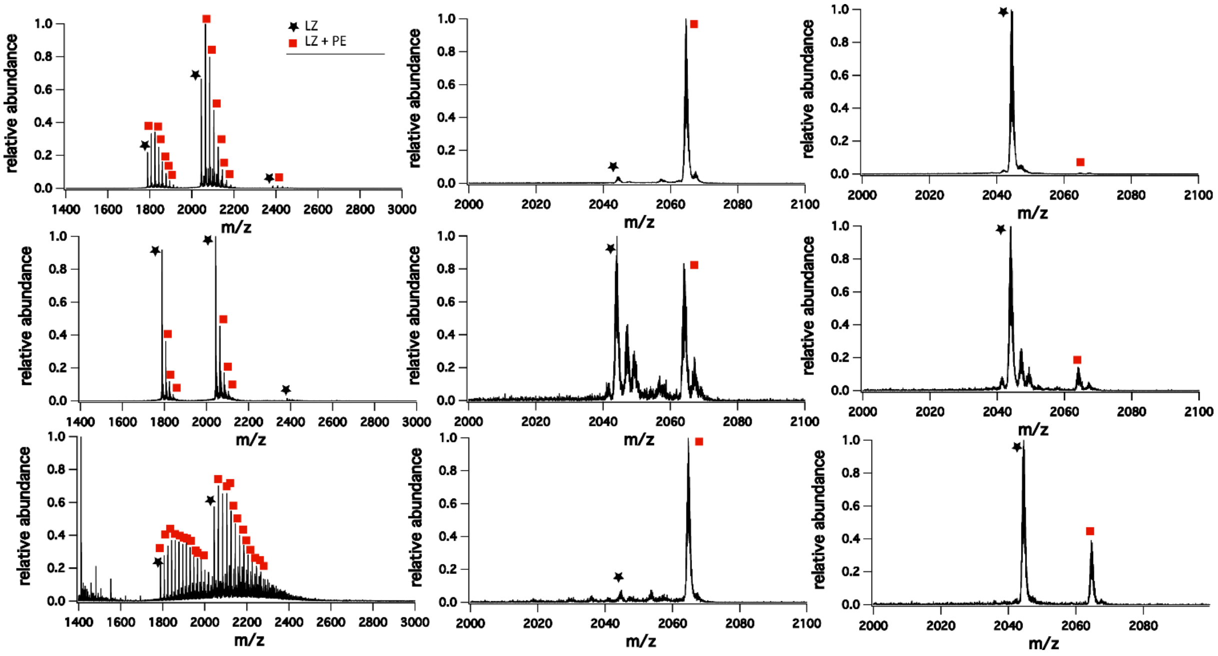

Figure A-S9: Mass spectra of Lysozyme and PE, left column is no isolation, middle column is isolation and low activation, right column is isolation and high activation.

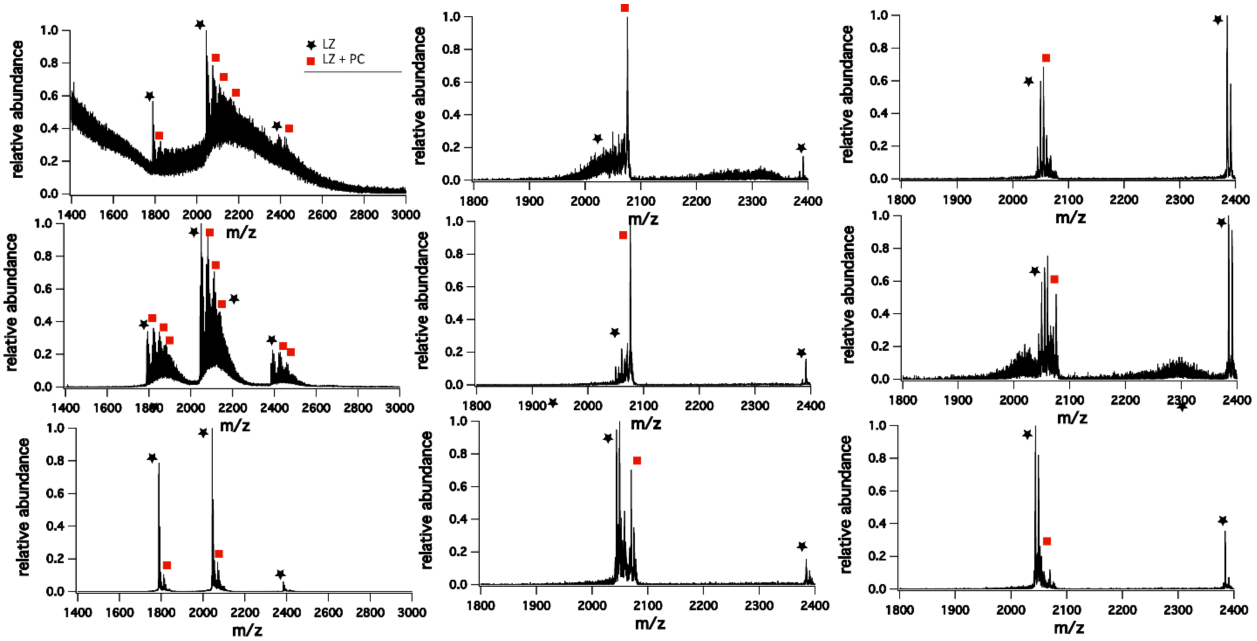

Figure A-S10: Mass spectra of Lysozyme and PC, left column is no isolation, middle column is isolation and low activation, right column is isolation and high activation.

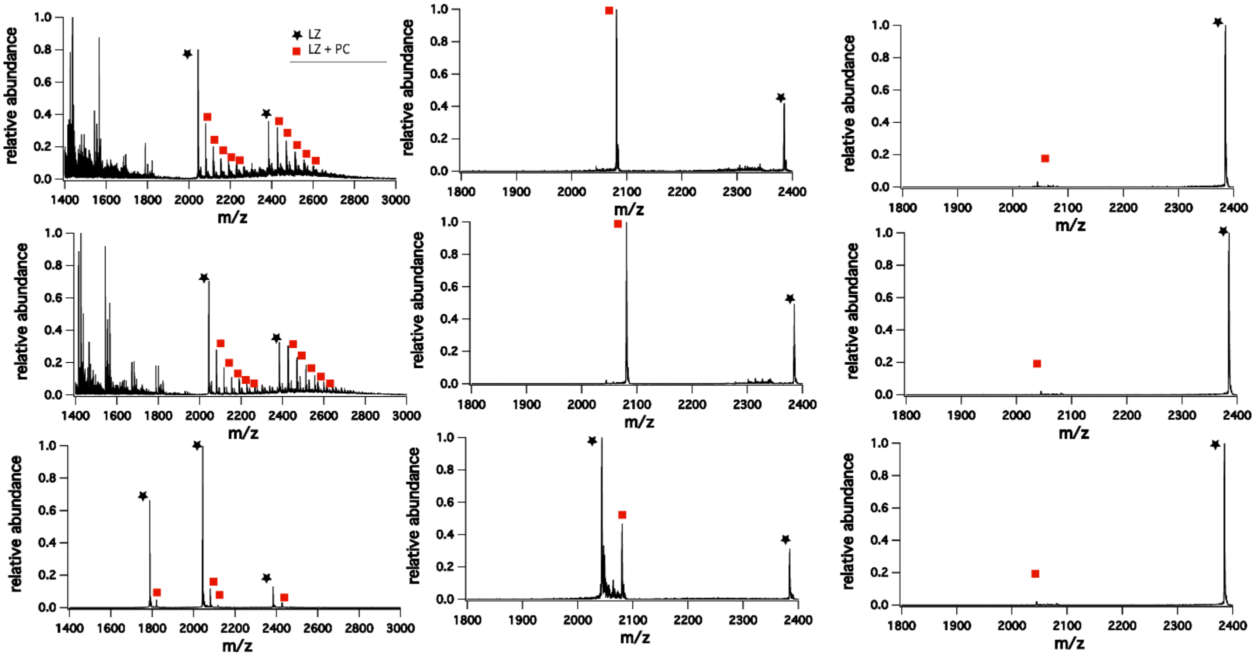

Figure A-S11: Mass spectra of Lysozyme and GPC, left column is no isolation, middle column is isolation and low activation, right column is isolation and high activation.

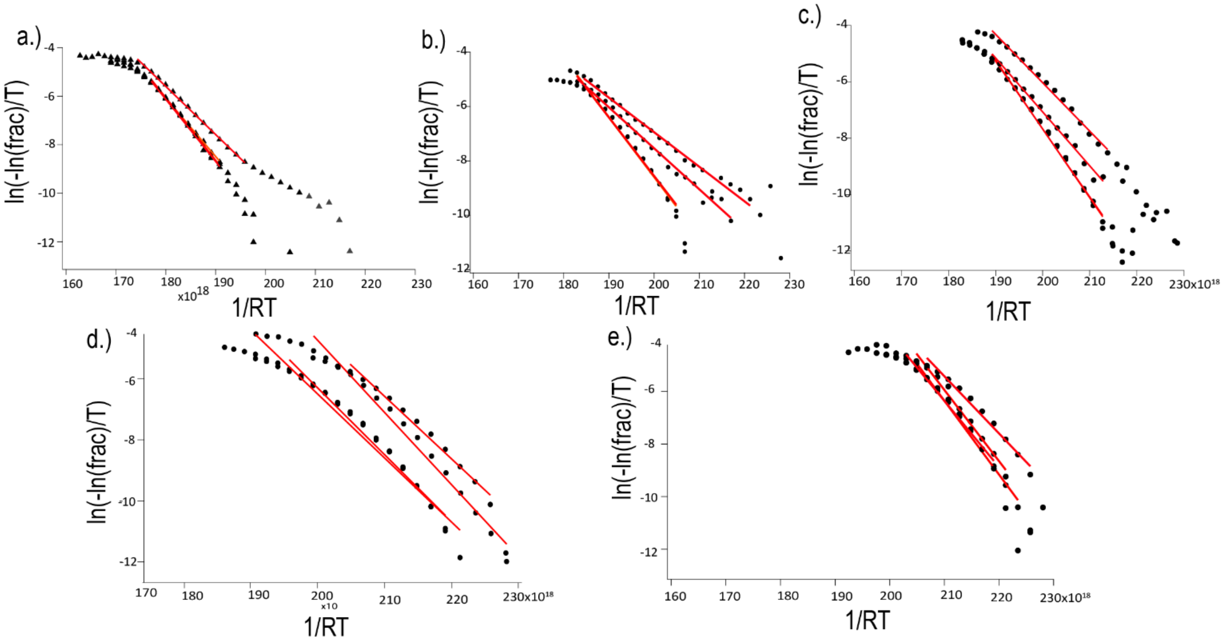

Figure A-S12. Eyring plots for CID of ubiquitin, 5+ losing bound lipid head groups **(a)** GPC **(b)** PC **(c)** PE **(d)** PG and **(e)** PS. The slope of the fit line is related to the activation enthalpy, and the y-intercept is related to the activation entropy. The data from 10% to 90% completed reaction was fit to the Eyring equation as explained in the theory and analysis portion.

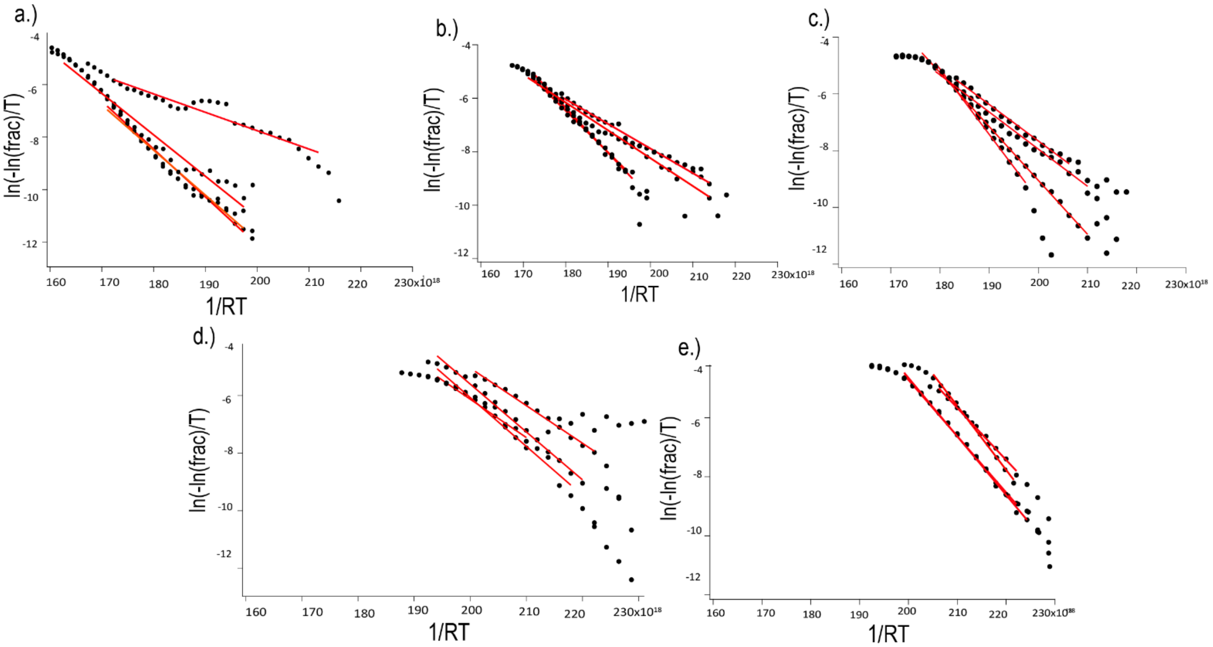

Figure A-S13. Eyring plots for CID of lysozyme, 7+ losing bound lipid head groups **(a)** GPC **(b)** PC **(c)** PE **(d)** PG and **(e)** PS. The slope of the fit line is related to the activation enthalpy, and the y-intercept is related to the activation entropy. In these experiments considerable drift was seen on the order of days and weeks. Because two sets of trials were taken on the same day with exceptionally low error (~1% difference), this is a long term drift and unlikely related to tip pulling.

Table A-S1**.** *Activation enthalpies and entropies for lipid head group CID.*

Head group	Ubiquitin, 5+ $\Delta S^{\ddagger}$ (kJ/mol)	Lysozyme, 7+ $\Delta S^{\ddagger}$ (kJ/mol)
GPC	275.0 ± 80.2	149.4 ± 47.0
PC	170.8 ± 26.5	63.4 ± 31.2
PE	150.8 ± 46.6	66.5 ± 71.6
PG	86.2 ± 68.7	17.2 ± 52.9
PS	160 ± 39.8	6.0 ± 68.3

Head group	Ubiquitin, 5+ $\Delta H^{\ddagger}$ (kJ/mol)	Lysozyme, 7+ $\Delta H^{\ddagger}$ (kJ/mol)
GPC	159.4 ± 27.8	116.9 ± 15.8
PC	128.4 ± 8.3	91.1 ± 10.7
PE	127.0 ± 17.8	99.8 ± 28.6
PG	105.0 ± 27.2	83.8 ± 21.9
PS	140.0 ± 16.8	84.0 ± 30.8

Head group	Ubiquitin, 5+ $\Delta G^{\ddagger}$ (kJ/mol)	Lysozyme, 7+ $\Delta G^{\ddagger}$ (kJ/mol)
GPC	64.6 ± 1.4	65.5 ± 2.0
PC	69.2 ± 3.0	69.1 ± 0.9
PE	73.4 ± 1.5	74.9 ± 2.5
PG	73.6 ± 2.3	76.7 ± 2.0
PS	79.4 ± 1.8	81.5 ± 3.0

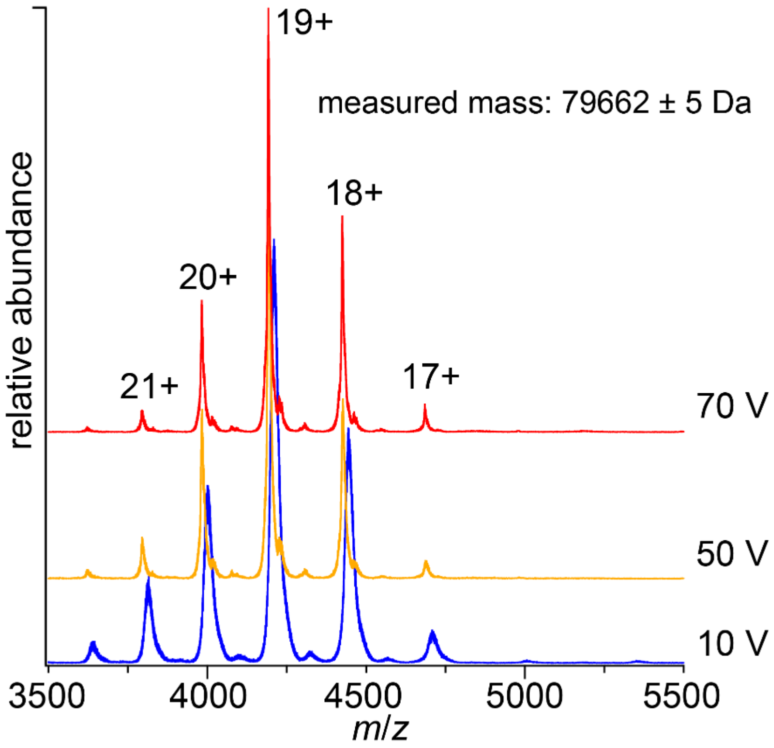

Figure A-S14. Native mass spectra of transferrin with no lipid head group present at Trap CE values of 10, 50, and 70 V. At all levels of activation transferrin produces clearly resolved spectra with a homogenous base mass.

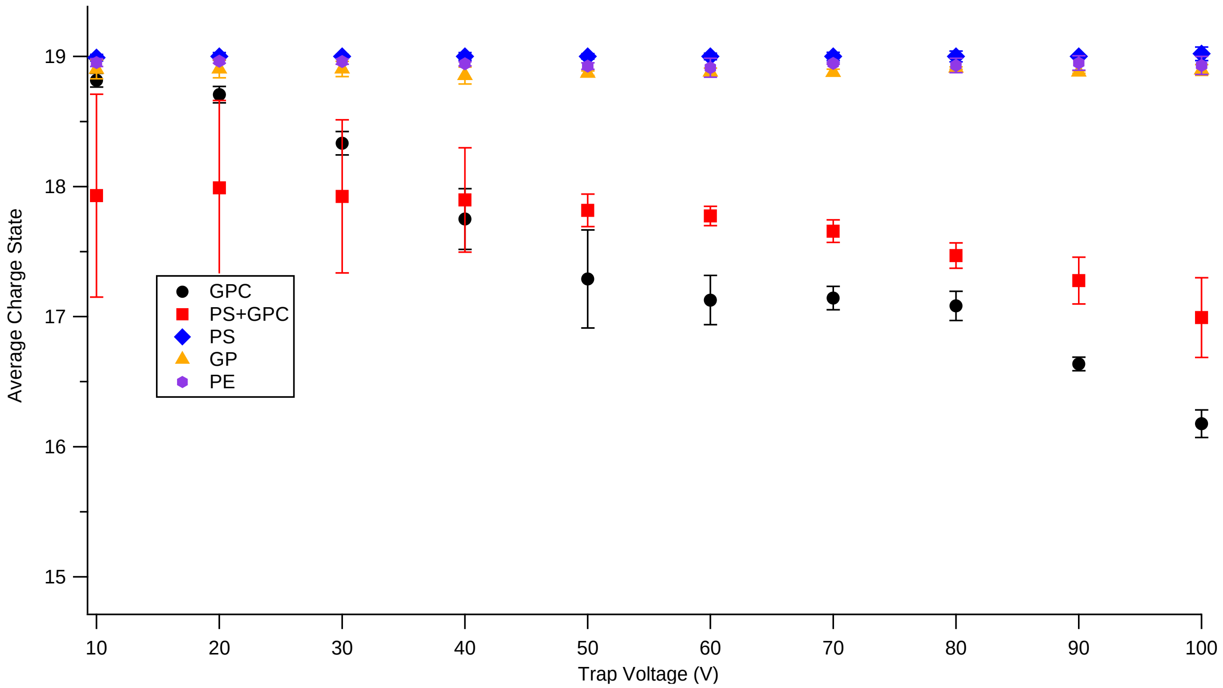

Figure A-S15. Change in weighted-average charge state of isolated TF19+ with increasing collisional activation. Charge state distributions were determined using Unidec, and error bars correspond to the weighted standard deviation of the charge state distribution. Significant loss of charge is observed only when GPC is present. The average charge state was also determined in these CID experiments to investigate charge stripping in mixed-binding environments (Figure 5). When PS, PE, and PG dissociate, no reduction in charge is observed. However, if GPC is present, either alone or in combination with another head group, charge stripping upon dissociation is observed, with an average of 2-3 charges lost at 100 V Trap CE. The rate of charge loss is similar across all the experiments with GPC present, suggesting that GPC dissociates more readily than the other head groups. This agrees with predicted behavior based on GB and the above results for Ubq and LZ and confirms that GPC dissociates readily and retains its charge stripping effect even in the presence of other head groups. This particular figure shows quantitation for only the initial trial in which unfolding of transferrin was not observed.

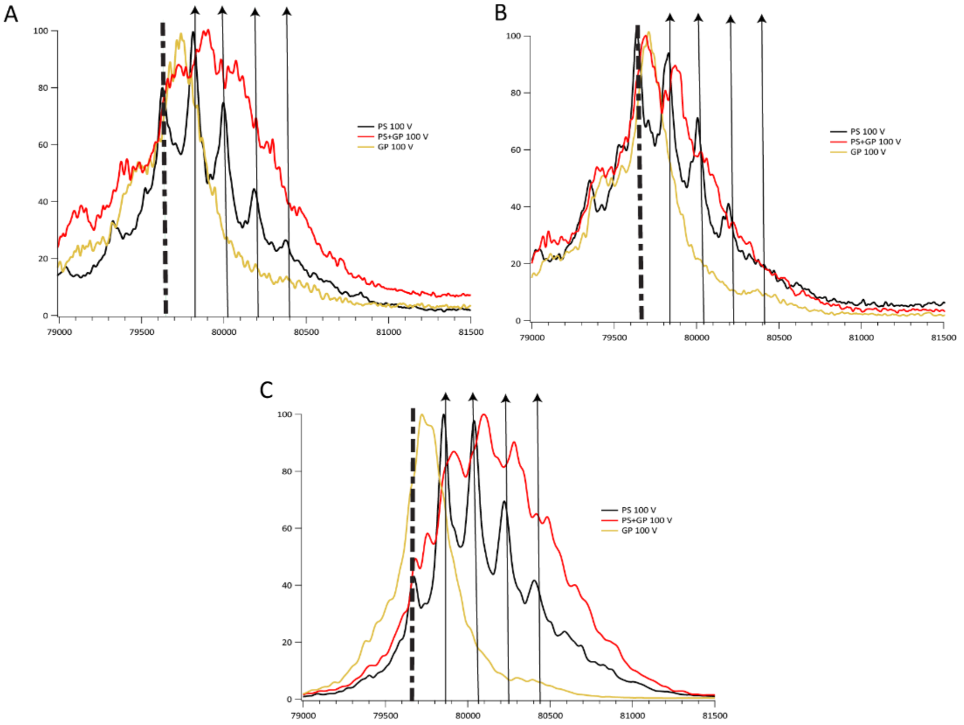

Figure A-S16. Overlaid deconvolved mass spectra for TF^{19+} with PS bound (black), PG bound (gold), and PS + PG bound (red) at a Trap CE of 100 V. The dashed line corresponds to the base mass of TF with no adducts. For TF with PG, no adducts are resolved, while for TF with PS several PS adducts are clearly resolved (stars). For TF with both PS and PG, partially-resolved adduct peaks are observed at *m*/*z* slightly higher than that of the PS adducts, likely corresponding to PS adducts with some additional salt adduction.

B. SUPPORTING INFORMATION FOR EFFECTS OF NANO-ELECTROSPRAY IONIZATION EMITTER POSITION ON UNINTENTIONAL IN-SOURCE ACTIVATION OF PEPTIDE AND PROTEIN IONS

Table B-S1: *Summary of Settings and Positions.*

data set	**Instrument**	**nESI potential (kV)**	**source pressure readback (mbar, unless otherwise noted)**	**trap gas (flow in mL/min, pressure in mbar for Synapt G2-*Si* data*)**	**capillary program used#**	**capillary position referenced to cone (vertical, along inlet axis, perpendicular to inlet axis, in mm)**
Figure 3, myoglobin (H2O/MeOH)	Synapt G2-*Si*	1.3	9.00E-03	5, 1.94e-2	2	~(0, 3, 2)
	Synapt G2-*Si*	1.3	9.11E-03	2.2, 9.45e-3	2	~(0, 3, 2)
	Synapt G2-*Si*	1.3	9.05E-03	2.2, 9.45e-3	2	~(0, 3, 2)
	Synapt G2-*Si*	0.9	9.11E-03	2.2, 9.45e-3	2	varied
	Synapt G2-*Si*	0.9	9.22E-03	2.2,9.51e-3	2	varied
	Synapt G2-*Si*	1	9.05E-03	2.2, 9.51e-3	2	varied
Figure 3 leucine enkephalin	Synapt G2-*Si*	0.9	9.05E-03	4, 1.60e-2	2	varied
	Synapt G2-*Si*	1	9.05E-03	4, 1.6e-2	2	varied
	Synapt G2-*Si*	1	9.05E-03	4, 1.61e-2	2	varied
	Synapt G2-*Si*	0.9	9.11E-03	4, 1.6e-2	2	varied
	Synapt G2-*Si*	0.9	9.05E-03	2, 8.89e-3	2	(-1, 5, 3)
	Synapt G2-*Si*	1	9.11E-03	2, 8.83e-3	2	(-1, 5, 3)

	Synapt G2-S*i*	0.9	9.11E-03	2, 8.89e-3	2	(-1, 5, 3)
Figure 4, myoglobin (water/methanol)	Synapt G2-S*i*	1.3	9.22E-03	2.2, 9.57e-3	2	many
	Synapt G2-S*i*	1.3	9.17E-03	2.2, 9.57e-3	2	many
	Synapt G2-S*i*	1.3	9.11E-03	2.2, 9.51e-3	2	many
	Synapt G2-S*i*	1.3	9.22E-03	2.2, 9.45e-3	2	many
	Synapt G2-S*i*	1.3	9.17E-03	2.2, 9.57e-3	2	many
	Synapt G2-S*i*	1.3	9.17E-03	2.2, 9.51e-3	2	many
	Synapt G2-S*i*	1.3	9.17E-03	2.2, 9.45e-3	2	many
	Synapt G2-S*i*	1.3	9.17E-03	2.2, 9.51e-3	2	many
	Synapt G2-S*i*	1.5	9.22E-03	2.2, 9.45e-3	2	many
Figure S4, Shiga toxin B pentamer	Synapt G2-S*i*	1	9.17E-03	2.2, 9.45e-3	2	(0, 1, 1)
	Synapt G2-S*i*	1	9.17E-03	2.2, 9.45e-3	2	(-3, 1, 1)
Figure S7, myoglobin (35 micromolar in ammonium acetate)	Agilent 6545XT	1.2	Quad 5.494e-5 Torr	22	2	multiple
	Agilent 6545XT	1.2	Quad 5.494e-5 Torr	22	2	multiple
NIST mAb	Synapt G2-S*i*	0.9	9.51e-3	10,4.33e-2	2	(0, 3, 5)
	Synapt G2-S*i*	0.9		10,4.38e-2	2	(0, 0.5, 0.5)
Figure S5, leucine enkephalin	Agilent 6545XT	1.1	Quad 5.479e-5 Torr	22	2	Varied
leucine enkephalin	Synapt G2-S*i*	1	9.05E-03	5, 1.96e-2	2	(0, 5, 6), (0, 2, 2), (0, 5, 2), (0, 2, 6)
BSA day 1	Synapt G2-S*i*	0.9	9.45E-03	5, 2.71	2	(0, 3, 5)

	Synapt G2-S*i*	0.9	9.34E-03	5, 2.71e-2	2	(0, 0.5, 0.5)
BSA day 2	Synapt G2-S*i*	0.9	9.45E-03	5, 2.69e-2	2	(0, 3, 5)
	Synapt G2-S*i*	0.9	9.39E-03	5, 2.71	2	(0, 0.5, 0.5)
BSA day 3	Synapt G2-S*i*	0.9	9.41E-03	5, 2.69e-2	2	(0, 3, 5)
	Synapt G2-S*i*	0.9	9.39E-03	5, 2.69	2	(0, 0.5, 0.5)
myoglobin (8 micromolar, AA)	Synapt G2-S*i*	0.9	9.22E-03	5, 1.97e-2	2	(0, 3, 5)
	Synapt G2-S*i*	0.9	9.22E-03	5, 1.96e-2	2	(0, 0.5, 0.5)
myoglobin (8 micromolar, AA)	Agilent 6545XT	1.5	Quad 5.494e-5 Torr	22	2	(0, 2.5)
	Agilent 6545XT	1.5	Quad 5.494e-5 Torr	22	2	(2, 6)

* Agilent 6545XT does not have a pressure readback for the Collision Cell.

#The Sutter Instrument P97 Micropipette Puller program 2 used was heat-495 (ramp+1), pull-5, vel-40, time-235; this program resulted in ~2 micron i.d. emitters.

Appendix S1: Capillary Emitter Reproducibility and Methods.

Capillary emitter reproducibility and settings. Scanning electron microscopy (SEM) images of pulled nESI capillaries (6 before use in nESI and 3 after use) were acquired in order to measure the typical shape and i.d. of nESI emitters used in all experiments. The heating filament of the capillary puller was replaced once over the time period of data acquisition. The i.d. of the pulled emitter openings overall was 2.2 ± 0.6 µm, the emitter opening of the set of capillaries before the filament change was 2.4 ± 0.2 µm (a possible slight underestimate due to parallax effects), and the emitter opening of capillaries after a filament change was 1.9 ± 0.2 µm. These uncertainties are expected to correspond to ± ~10% variability in average initial nESI droplet diameter. Capillary taper length for these tips (defined as the distance from the beginning of the pulled capillary taper to the emitter tip, see Figure S2) varied negligibly in this study (3.3 ± 0.1 mm).

Other uncertainties (wire length and placement, reproducibility of micrometer placement, and left/right flexibility of emitter holder) are estimated to contribute 1 mm combined uncertainty in the directions along the instrument inlet axis and horizontal axis perpendicular to the inlet and less than 0.5 mm in the up/down direction. The end of the platinum wire was placed at the beginning of the taper by eye. These position variations are small compared to the distance between the “far” emitter position (~7 mm from instrument entrance), the “close” position (0-1 mm from instrument entrance), and the “below” position (1.5 mm below the “close” position) on a Synapt G2-S*i*. The stage position reproducibility on the Agilent 6545XT is estimated to be slightly worse, but in this case the positions described here are still separated from each other by ~4 mm. It is therefore expected that variation in emitter position due to tuning nESI stage micrometer positions contributes most of the source geometry-dependent variation observed in the experiments described in this manuscript, though the variability effects above are likely relevant for reproducibility in other studies.

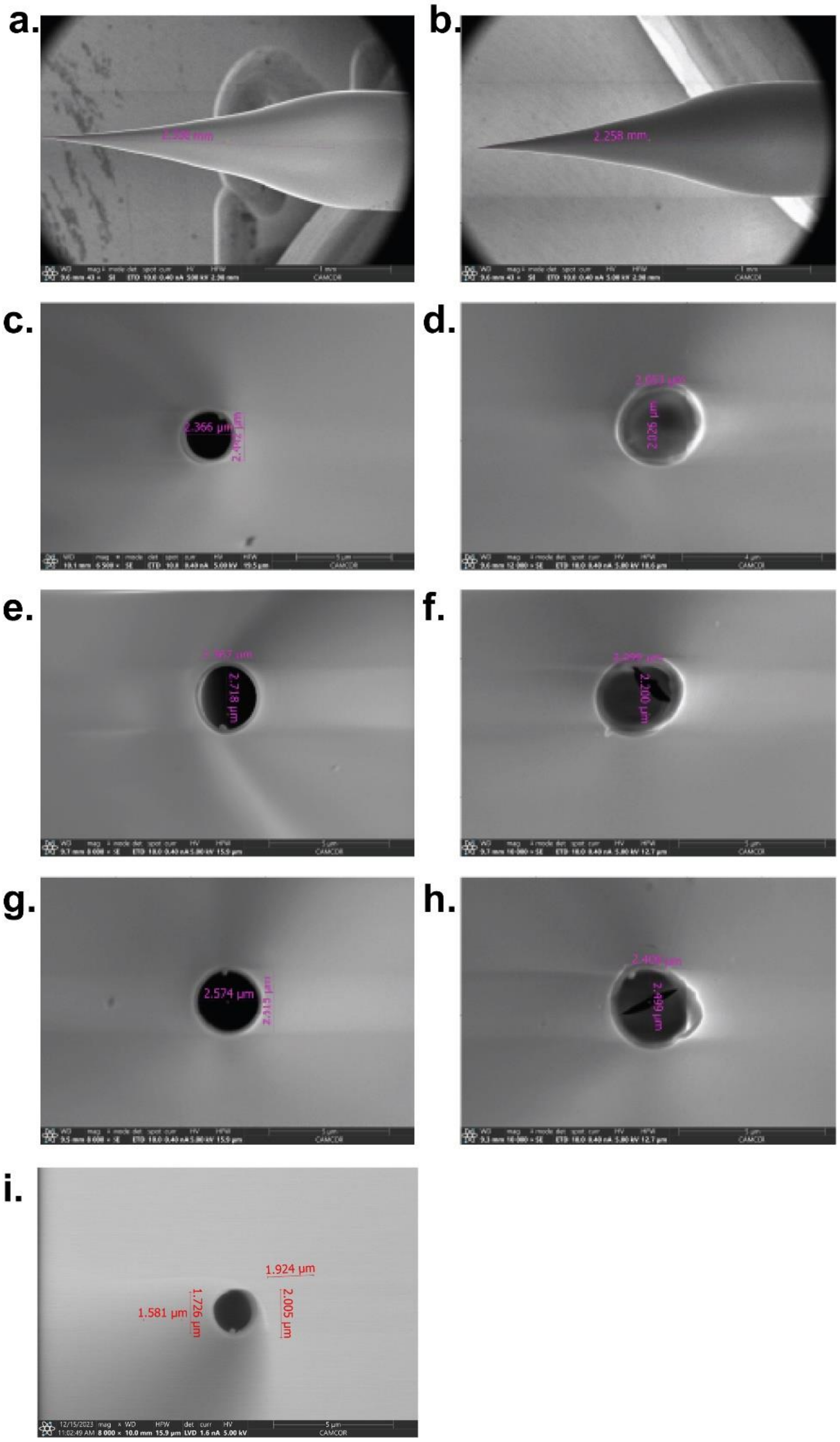
a.
b.
2.258 mm
c.
2.366 µm
d.
2.026 µm
e.
2.718 µm
f.
2.200 µm
g.
2.574 µm
h.
2.499 µm
i.
1.924 µm
1.581 µm
1.726 µm
2.005 µm
12/15/2023
11:02:49 AM
CAMCOR

Figure B-S1. Representative emitter SEM images from before (a, c, e, g, and i) and after (b, d, f, and h) nESI. Measurements shown in images are made by SEM software. The morphology of the emitters (a and b) is similar across all emitters. The emitters with filament 1 (a-h) differ somewhat in opening diameter from those pulled using filament 2 (i).

Table B-S2. *CIUSuite2 Processing Parameters.*

		BSA	NIST mAb
Data Import	Smoothing: Savitzky-Golay	Window 5; Iteration 1 (default)	(default)
	Crop: none (5-200V)	5-200 V 0-200 bins	5-200 V 0-200 bins
	Plot options	Default	Default
	Injection Potential step size	5 V	5 V
Feature Detection	Mode	Default	Default
	Minimum feature length	4	4
	Interpolation	2	2
	Feature width allowed	0.75	0.75-1.2
	Max CV gap	0	0
CIU-50 Fitting	mode	Default	Default
	Transition region padding	15	15
	Max CV gap	0	0

Appendix S2: RMSD analysis

Average of Pairwise and Pairwise of Average Differences in Scaling. Because RMSD between CIU fingerprints is by definition a positive number (it is the square root of the sum of many squared real numbers), there is not a unique way to define the “average difference” among multiple CIU fingerprints as one would with numbers that can take on any real value. In particular, RMSD between replicate-averaged CIU fingerprints belonging to two sets of data and the average of the RMSD between each possible pair of replicates (one from each set) can often be similar, especially when the fingerprints within each set are very similar, but the sets as a whole differ greatly. However, when differences within sets and between sets are similar in (absolute) magnitude, these two types of average RMSD can differ substantially. The average-of-pairwise RMSD ($RMSD_{AofP}$) includes consideration of the noise in the data (and is higher for data with greater variation within a triplicate), while the pairwise RMSD of averages ($RMSD_{PofA}$) considers only the average value. Consequently the $RMSD_{PofA}$ can be lower than $RMSD_{AofP}$ of replicates while still representing a significant difference. Thus, we use $RMSD_{AofP}$ for comparisons of inter-position RMSD values. This method averages only the pairwise RMSDs between close and far position and excludes those between two close positions or two far positions.

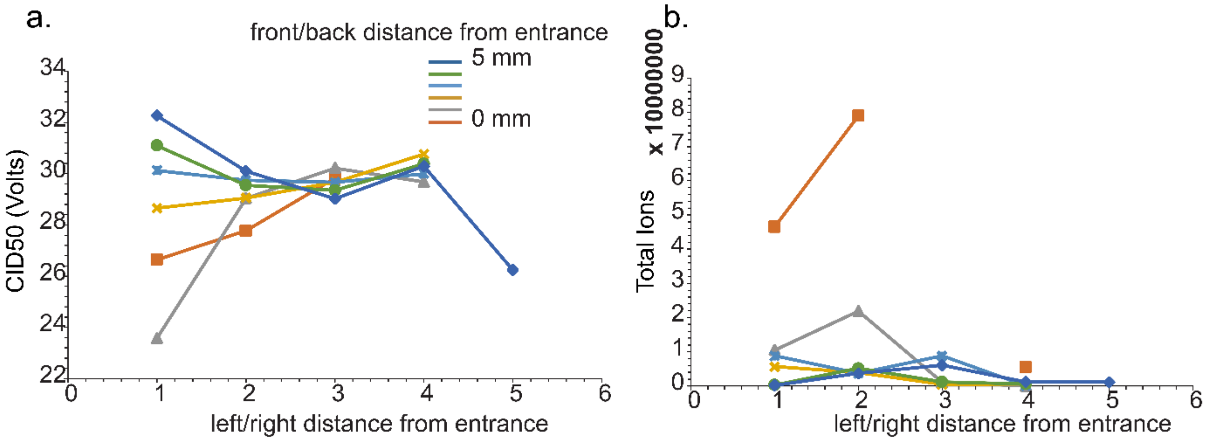

Figure B-S2. Example of CID50 vs signal strength for partially denatured holomyoglobin^{9+} on a Waters Synapt G2-Si (a) CID50 vs emitter position as compared to (b) total ions vs emitter position.

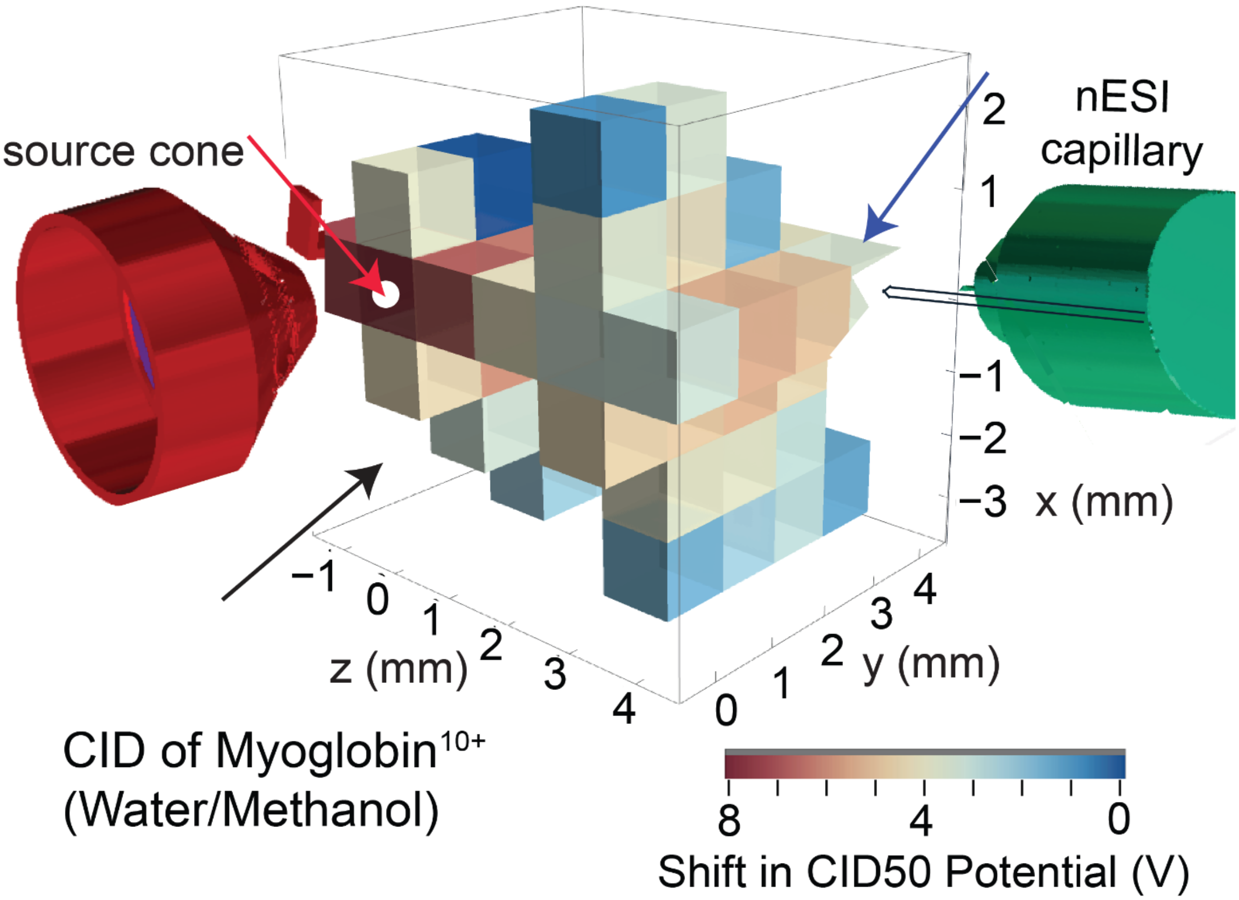

Figure B-S3. Spatial map of CID50 shift for partially denatured myoglobin^{10+} as a function of emitter position. The white dot represents the emitter position origin (0, 0, 0).

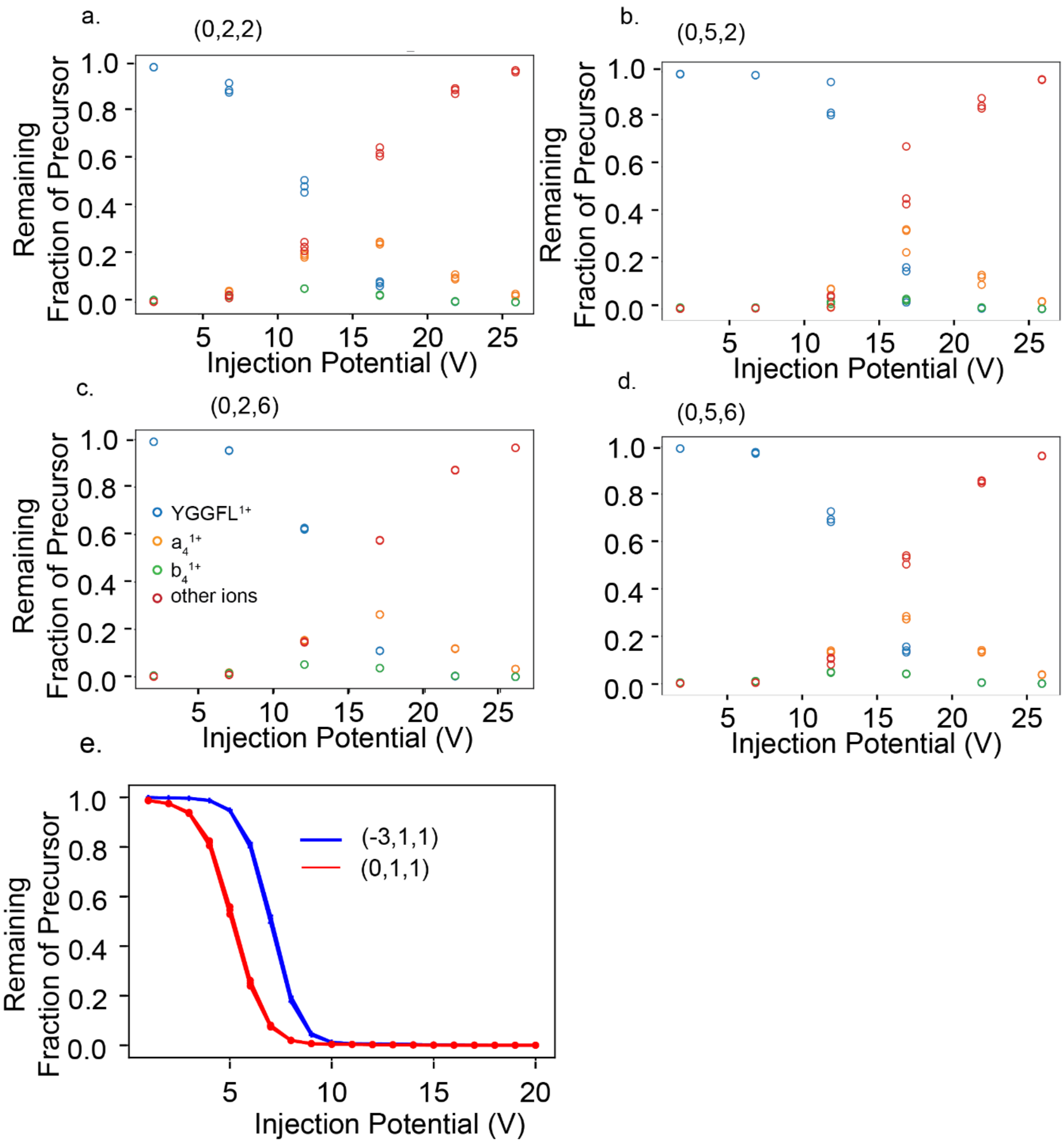

Figure B-S4. Emitter position influence on leucine enkephalin (a-d), where the close position (0, 2, 2) shows 3-4 V more in-source activation (lower CID50) than the far position (0, 5, 6). Shiga toxin pentamer (e) shows 4 V more in-source activation at a close (0, 1, 1) than a peripheral (-3, 1, 1) position. All data were acquired on a Synapt G2-S*i*. These and other CID50 are summarized in Figure S8.

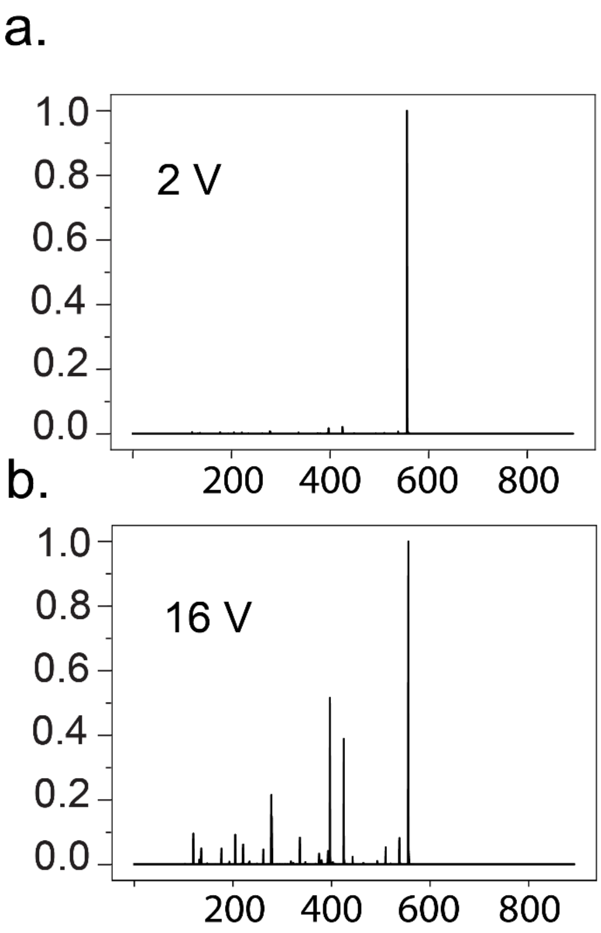

Figure B-S5. Representative mass spectra of leucine enkephalin at a low (a) and near CID50 (b) voltage. Leucine enkephalin dissociates into primarily a_4 and b_4 ions, these ions subsequently dissociate due to additional collisional activation. All detected product ions are summed in calculating the fraction of precursor remaining (see main text).

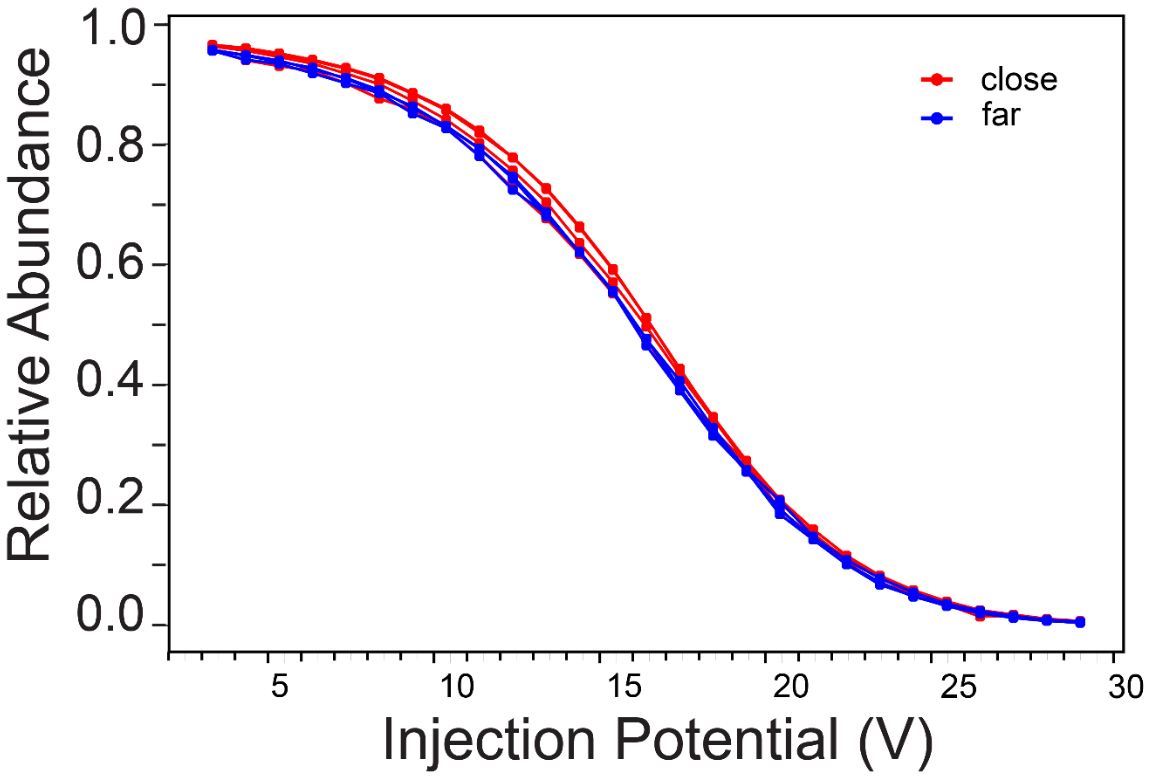

Figure B-S6. CID of leucine enkephalin in close (1-3 mm total distance, red) and far (5-7 mm total distance, blue) positions on the Agilent 6545XT Q-TOF Mass Spectrometer.

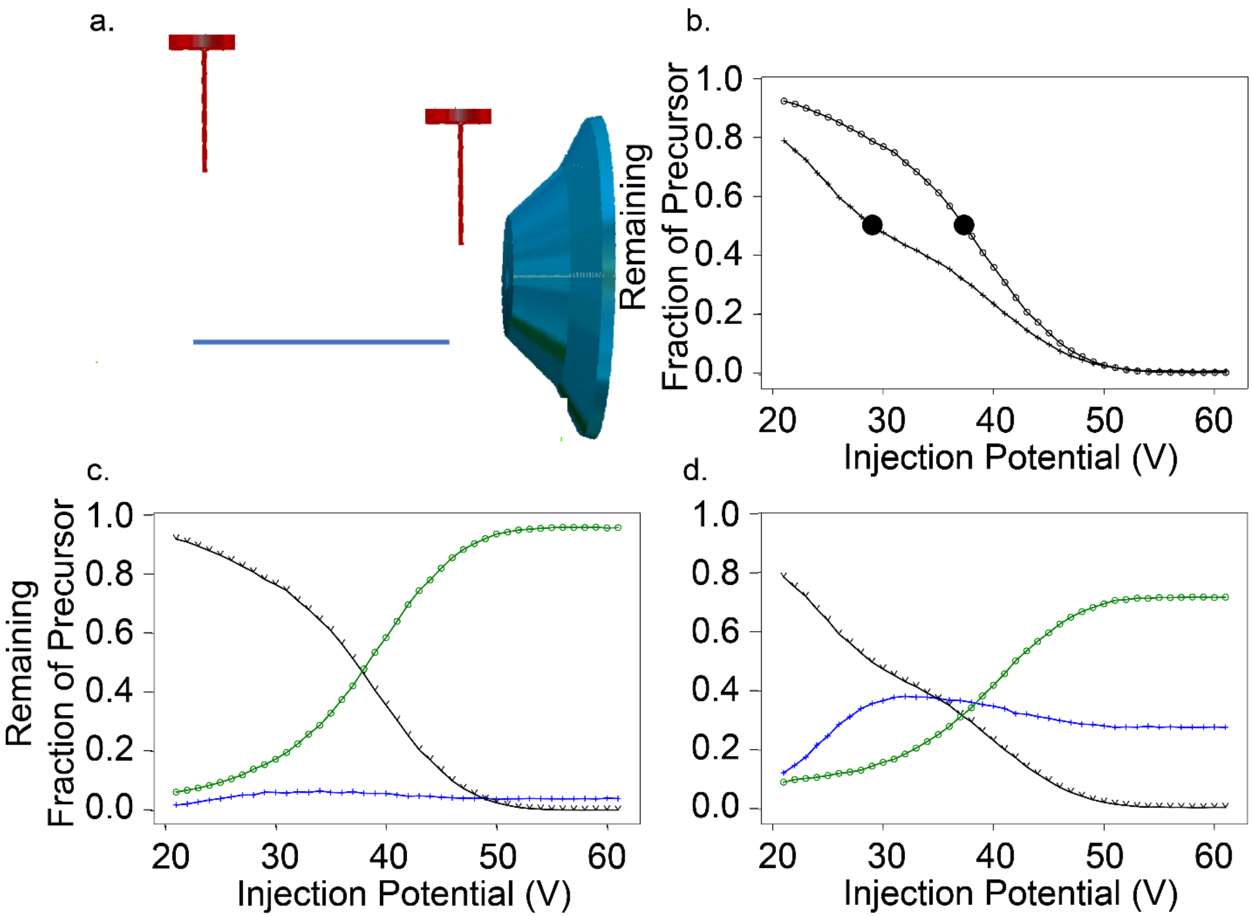

Figure B-S7. (a) shows a diagram representing the close (right) and far (left) nESI emitter positions on the 6545XT Q-TOF Mass Spectrometer. (b) shows the holomyoglobin^{9+} CID breakdown curves for the close (right) and far(left) with a large difference in CID50 (black circles). (c) and (d) show the breakdown curves (black) and appearance curves of heme^{0} (blue) and heme^{1+} (green) for the close (left, c) and far (right, d) emitter positions. The shift in CID50 is caused by the presence of a second channel to heme^{0} in the far position as the appearance curves (green) have the same midpoint.

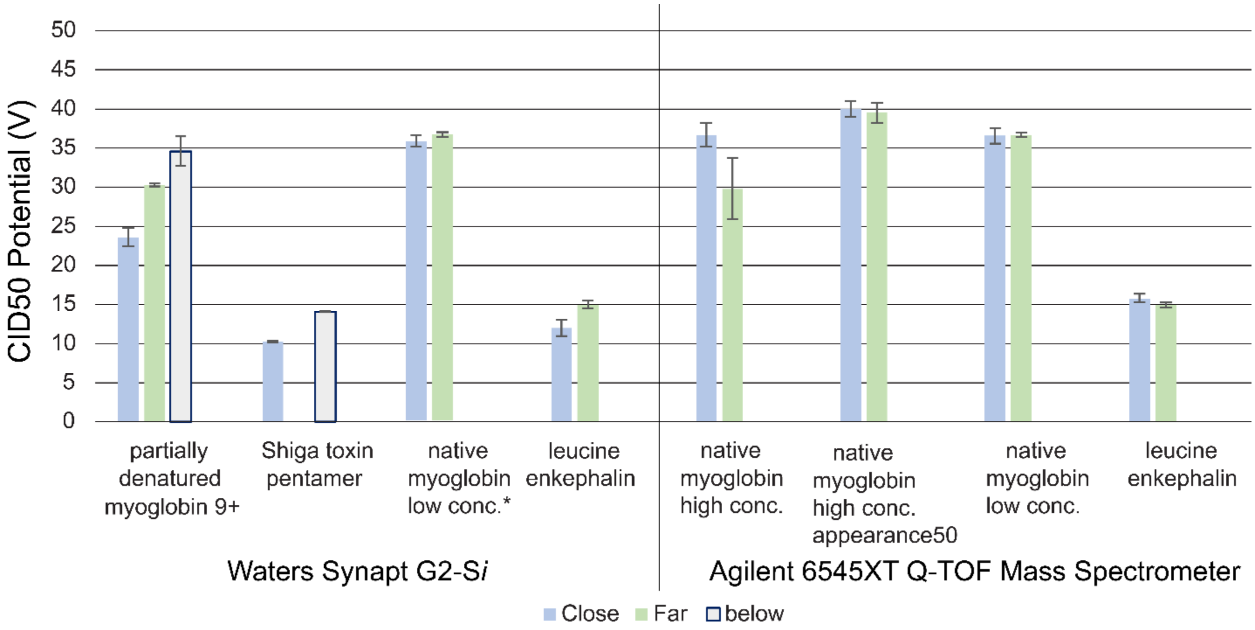

Figure B-S8. Summary of CID50 values in “close” (blue), “far” (green) and “below” nESI emitter positions (gray) on both the Waters Synapt G2-S*i* and the Agilent 6545XT Q-TOF Mass Spectrometer (see main text and Table S1).

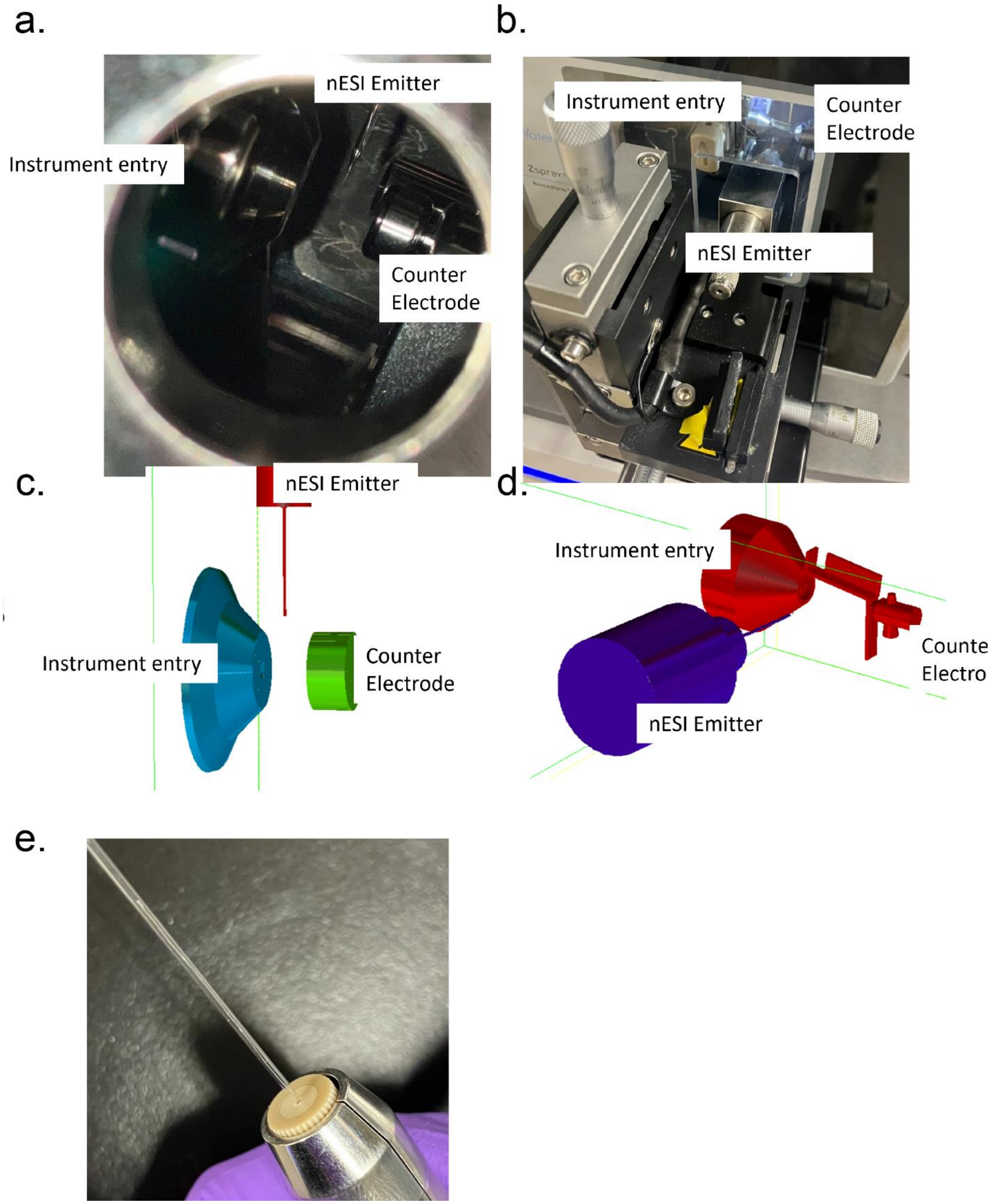
a.
nESI Emitter
Instrument entry
Counter Electrode
b.
Instrument entry
Counter Electrode
nESI Emitter
c.
nESI Emitter
Instrument entry
Counter Electrode
d.
Instrument entry
Counte Electro
nESI Emitter
e.

Figure B-S9. Images of the Agilent 6545XT Q-TOF Mass Spectrometer (a) and Waters Synapt G2-Si (b) nESI source designs with representative diagrams (c and d, respectively). (e) shows the additional piece fashioned for the nESI emitter holder on the Agilent 6545XT by placing a piece with an emitter width opening bored out inside of an LC fitting. This piece is used to increase symmetry of the emitter/emitter holder together and to keep the emitter pointed at 90 degrees from the entrance to the instrument.

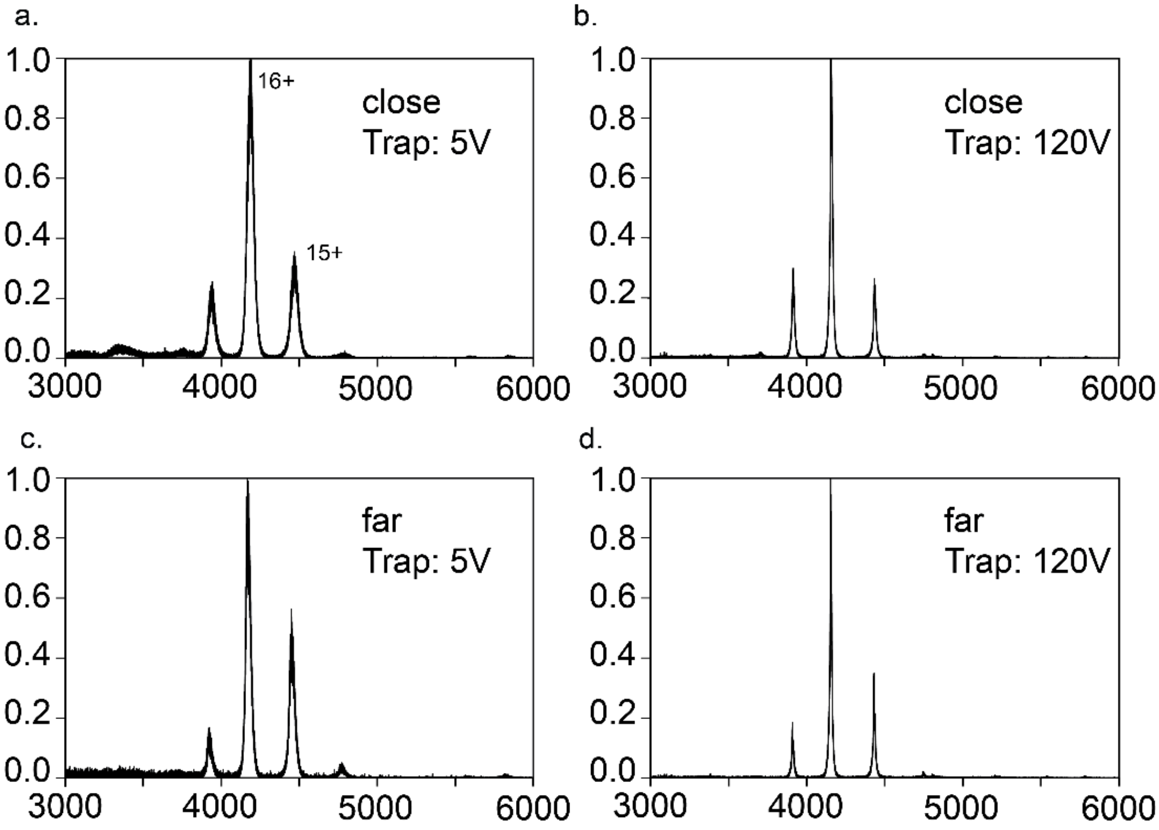

Figure B-S10. Representative native mass spectra of BSA in the close (a,b) and far (c,d) positions at a low (a,c) and high (b,d) Trap injection potential.

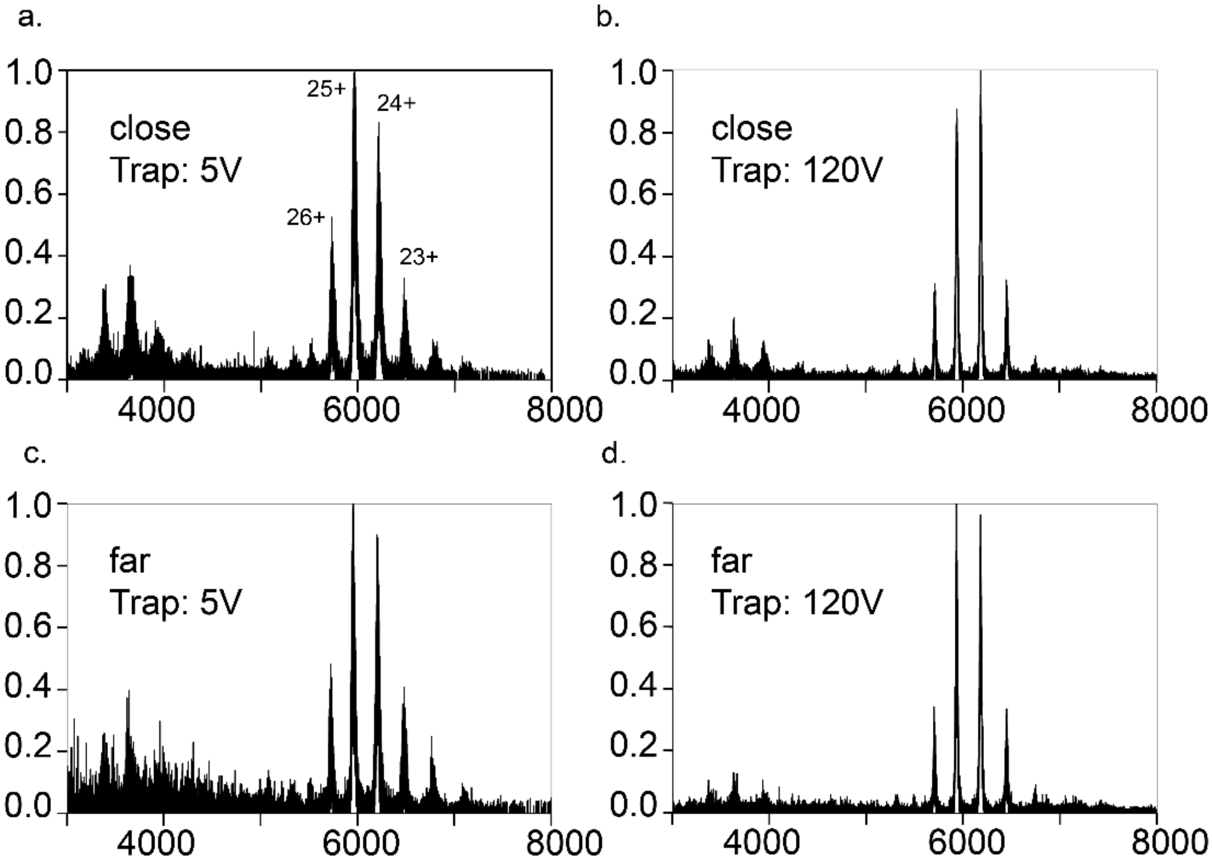

Figure B-S11. Representative mass spectra of NIST mAb in the close (a,b) and far (c,d) positions at a low (a,c) and high (b,d) Trap injection potential.

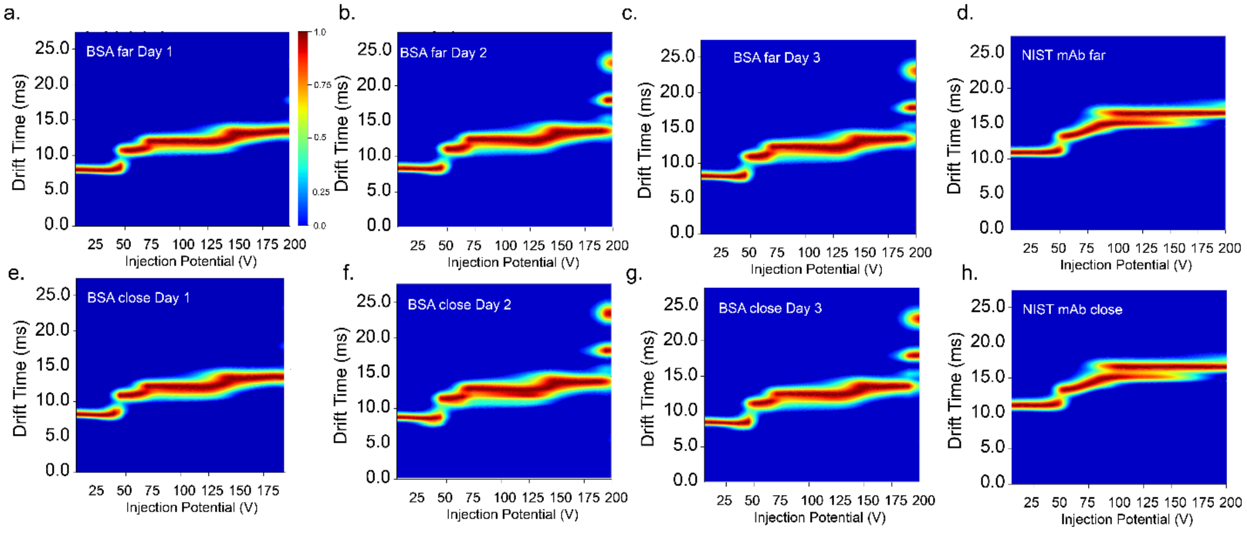

Figure B-S12. Average of quintuplicate CIU fingerprints taken at each nESI emitter position on 3 separate days (a-c, far; e-g, close) for BSA^{15+} and for NIST mAb^{25+} (d, far; h, close) on Synapt G2-S*i*.

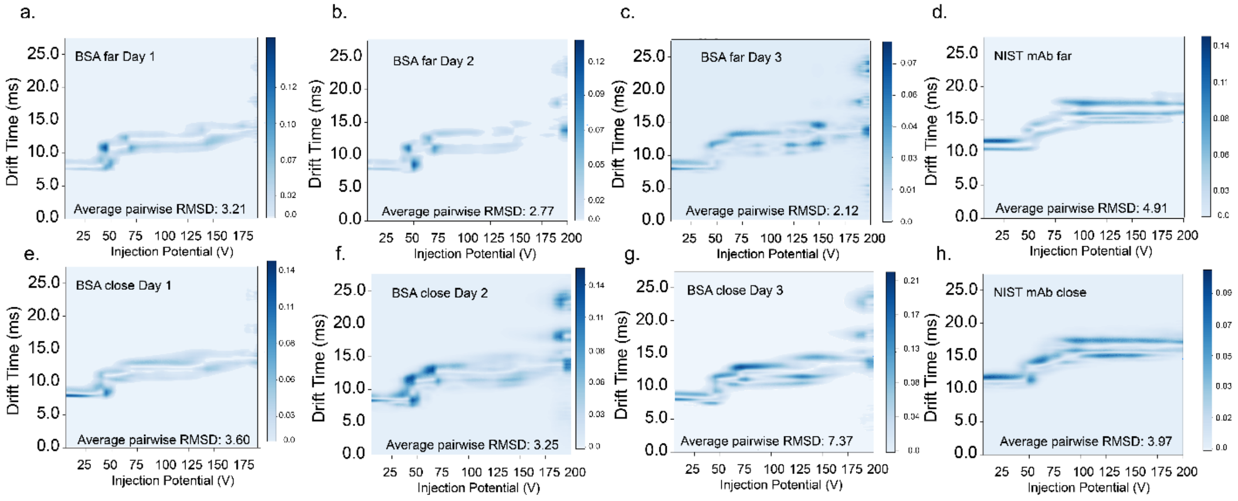

Figure B-S13. Average difference of CIU fingerprints for quintuplicates taken at each nESI emitter position on 3 separate days (a-c, far; e-g, close) for BSA^{15+} and for NIST mAb^{25+} (d, far; h, close) on Synapt G2-S*i*.

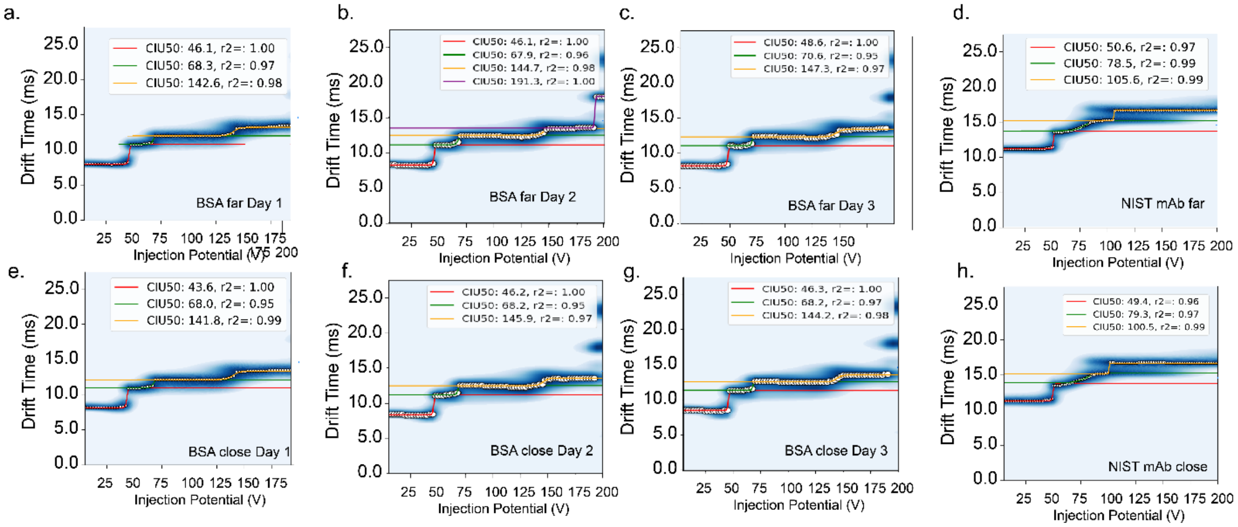

Figure B-S14. CIU50 fits of the averages of the quintuplicate data shown in Figures S12 and S13 taken at each nESI emitter position on 3 separate days (a-c, far; e-g, close) for BSA^{15+} and for NIST mAb^{25+} (d, far; h, close).

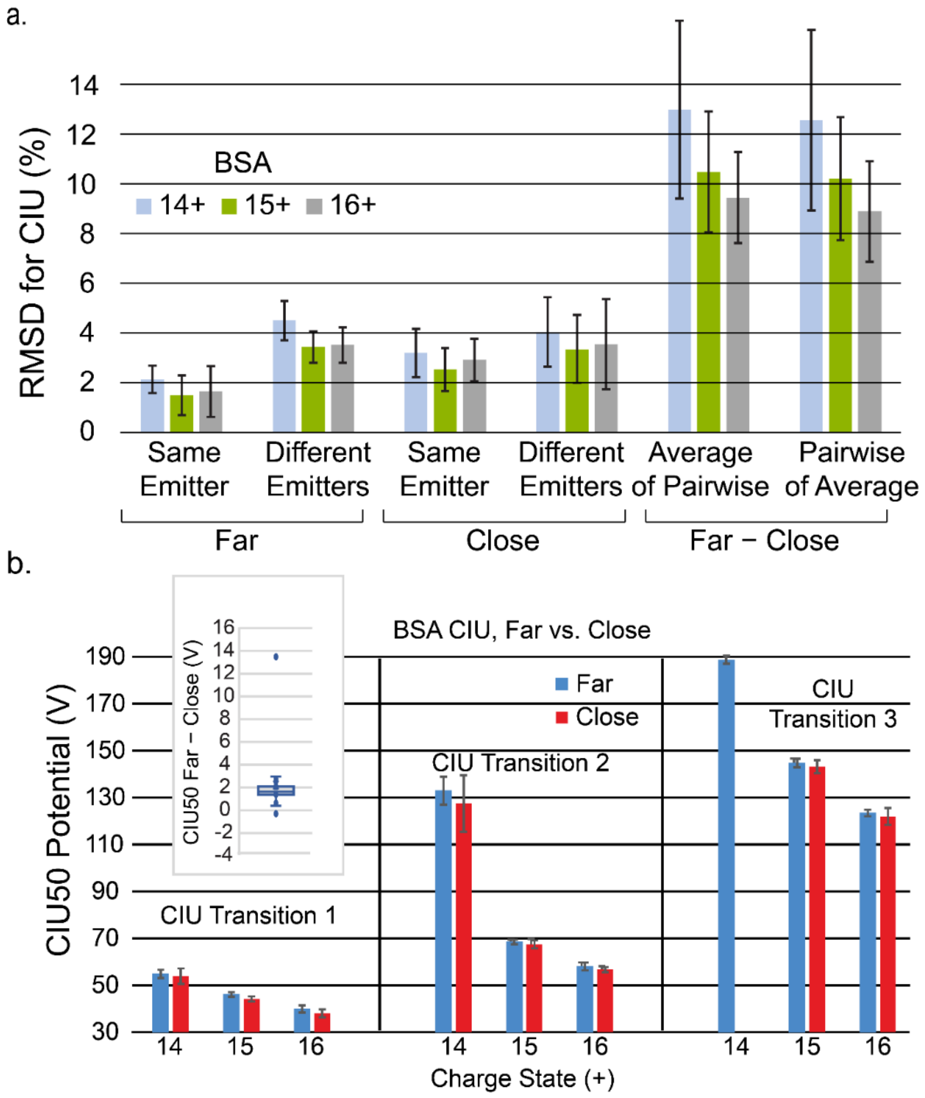

Figure B-S15. RMSD (a) and CIU50 analysis (b) for native charge states of BSA with the exclusion of the high RMSD replicate ("close" nESI emitter position, day 3). With this outlier replicate excluded, both RMSD and CIU50 statistics indicate a clearer difference between "close" and "far" emitter positions. However, it is strongly recommended to acquire multiple replicates at fixed positions to assess the relative magnitude in differences introduced by changing emitter position vs. exchanging emitters.

REFERENCES CITED

(1) Brodbelt, J. S.; Morrison, L. J.; Santos, I. *Chem. Rev.* **2020**, *120* (7), 3328–3380. https://doi.org/10.1021/acs.chemrev.9b00440.

(2) Tamara, S.; den Boer, M. A.; Heck, A. J. R. *Chem. Rev.* **2022**, *122* (8), 7269–7326. https://doi.org/10.1021/acs.chemrev.1c00212.

(3) Snyder, D. T.; Harvey, S. R.; Wysocki, V. H. *Chem. Rev.* **2022**, *122* (8), 7442–7487. https://doi.org/10.1021/acs.chemrev.1c00309.

(4) Rolland, A. D.; Prell, J. S. *Chem. Rev.* **2022**, *122* (8), 7909–7951. https://doi.org/10.1021/acs.chemrev.1c00696.

(5) Pukala, T.; Robinson, C. V. *Chem. Rev.* **2022**, *122* (8), 7267–7268. https://doi.org/10.1021/acs.chemrev.2c00085.

(6) James, E. I.; Murphree, T. A.; Vorauer, C.; Engen, J. R.; Guttman, M. *Chem. Rev.* **2022**, *122* (8), 7562–7623. https://doi.org/10.1021/acs.chemrev.1c00279.

(7) Vallejo, D. D.; Rojas Ramírez, C.; Parson, K. F.; Han, Y.; Gadkari, V. V.; Ruotolo, B. T. *Chem. Rev.* **2022**, acs.chemrev.1c00857. https://doi.org/10.1021/acs.chemrev.1c00857.

(8) Pacholarz, K. J.; Garlish, R. A.; Taylor, R. J.; Barran, P. E. *Chem. Soc. Rev.* **2012**, *41* (11), 4335–4355. https://doi.org/10.1039/C2CS35035A.

(9) Laganowsky, A.; Clemmer, D. E.; Russell, D. H. *Annu. Rev. Biophys.* **2022**, *51* (1), 63–77. https://doi.org/10.1146/annurev-biophys-102221-101121.

(10) Mehmood, S.; Allison, T. M.; Robinson, C. V. *Annu. Rev. Phys. Chem.* **2015**, *66* (1), 453–474. https://doi.org/10.1146/annurev-physchem-040214-121732.

(11) Zhurov, K. O.; Fornelli, L.; Wodrich, M. D.; Laskay, Ü. A.; Tsybin, Y. O. *Chem. Soc. Rev.* **2013**, *42* (12), 5014–5030. https://doi.org/10.1039/C3CS35477F.

(12) Vallejo, D. D.; Jeon, C. K.; Parson, K. F.; Herderschee, H. R.; Eschweiler, J. D.; Filoti, D. I.; Ruotolo, B. T. *Anal. Chem.* **2022**, *94* (18), 6745–6753. https://doi.org/10.1021/acs.analchem.2c00160.

(13) Quintyn, R. S.; Zhou, M.; Yan, J.; Wysocki, V. H. *Anal. Chem.* **2015**, *87* (23), 11879–11886. https://doi.org/10.1021/acs.analchem.5b03441.

(14) Heck, A. J. R.; van den Heuvel, R. H. H. *Mass Spectrom. Rev.* **2004**, *23* (5), 368–389. https://doi.org/10.1002/mas.10081.

(15) Keener, J. E.; Zhang, G.; Marty, M. T. *Anal. Chem.* **2021**, *93* (1), 583–597. https://doi.org/10.1021/acs.analchem.0c04342.

(16) Mitra, G. *Biochim. Biophys. Acta BBA - Proteins Proteomics* **2019**, *1867* (11), 140260. https://doi.org/10.1016/j.bbapap.2019.07.013.

(17) Webb, I. K. *Biochim. Biophys. Acta BBA - Proteins Proteomics* **2022**, *1870* (1), 140732. https://doi.org/10.1016/j.bbapap.2021.140732.

(18) Boeri Erba, E.; Petosa, C. *Protein Sci.* **2015**, *24* (8), 1176–1192. https://doi.org/10.1002/pro.2661.

(19) van Duijn, E. *J. Am. Soc. Mass Spectrom.* **2010**, *21* (6), 971–978. https://doi.org/10.1016/j.jasms.2009.12.010.

(20) Barth, M.; Schmidt, C. *J. Mass Spectrom.* **2020**, *55* (10), e4578. https://doi.org/10.1002/jms.4578.

(21) Heck, A. J. R. *Nat. Methods* **2008**, *5* (11), 927–933. https://doi.org/10.1038/nmeth.1265.

(22) Paizs, B.; Suhai, S. *Mass Spectrom. Rev.* **2005**, *24* (4), 508–548. https://doi.org/10.1002/mas.20024.

(23) Yost, R. A.; Enke, C. G. *Org. Mass Spectrom.* **1981**, *16* (4), 171–175. https://doi.org/10.1002/oms.1210160406.
(24) Brandner, S.; Habeck, T.; Lermyte, F. *J. Am. Soc. Mass Spectrom.* **2023**, *34* (9), 1908–1916. https://doi.org/10.1021/jasms.3c00106.
(25) Black, R.; Barkhanskiy, A.; Ramakers, L. A. I.; Theisen, A.; Brown, J. M.; Bellina, B.; Trivedi, D. K.; Barran, P. E. *Int. J. Mass Spectrom.* **2021**, *464*, 116588. https://doi.org/10.1016/j.ijms.2021.116588.
(26) Bythell, B. J.; Suhai, S.; Somogyi, Á.; Paizs, B. *J. Am. Chem. Soc.* **2009**, *131* (39), 14057–14065. https://doi.org/10.1021/ja903883z.
(27) Williams, P. E.; Klein, D. R.; Greer, S. M.; Brodbelt, J. S. *J. Am. Chem. Soc.* **2017**, *139* (44), 15681–15690. https://doi.org/10.1021/jacs.7b06416.
(28) Laskin, J.; Bailey, T. H.; Futrell, J. H. *J. Am. Chem. Soc.* **2003**, *125* (6), 1625–1632. https://doi.org/10.1021/ja027915t.
(29) Laskin, J.; Denisov, E.; Futrell, J. *J. Am. Chem. Soc.* **2000**, *122* (40), 9703–9714. https://doi.org/10.1021/ja001384w.
(30) Ieritano, C.; Hopkins, W. S. *J. Phys. Chem. Lett.* **2021**, *12* (25), 5994–5999. https://doi.org/10.1021/acs.jpclett.1c01538.
(31) Kitova, E. N.; El-Hawiet, A.; Schnier, P. D.; Klassen, J. S. *J. Am. Soc. Mass Spectrom.* **2012**, *23* (3), 431–441. https://doi.org/10.1007/s13361-011-0311-9.
(32) Kang, J.; Halseth, T.; Vallejo, D.; Najafabadi, Z. I.; Sen, K. I.; Ford, M.; Ruotolo, B. T.; Schwendeman, A. *Anal. Bioanal. Chem.* **2020**, *412* (3), 763–775. https://doi.org/10.1007/s00216-019-02298-9.
(33) Shirzadeh, M.; Poltash, M. L.; Laganowsky, A.; Russell, D. H. *Biochemistry* **2020**, *59* (9), 1013–1022. https://doi.org/10.1021/acs.biochem.0c00105.
(34) Fantin, S. M.; Parson, K. F.; Niu, S.; Liu, J.; Polasky, D. A.; Dixit, S. M.; Ferguson-Miller, S. M.; Ruotolo, B. T. *Anal. Chem.* **2019**, *91* (24), 15469–15476. https://doi.org/10.1021/acs.analchem.9b03208.
(35) Tian, Y.; Lippens, J. L.; Netirojjanakul, C.; Campuzano, I. D. G.; Ruotolo, B. T. *Protein Sci.* **2019**, *28* (3), 598–608. https://doi.org/10.1002/pro.3560.
(36) Karch, K. R.; Snyder, D. T.; Harvey, S. R.; Wysocki, V. H. *Annu. Rev. Biophys.* **2022**, *51* (1), 157–179. https://doi.org/10.1146/annurev-biophys-092721-085421.
(37) Linke, W. A.; Grützner, A. *Pflüg. Arch. - Eur. J. Physiol.* **2008**, *456* (1), 101–115. https://doi.org/10.1007/s00424-007-0389-x.
(38) Bustamante, C. J.; Chemla, Y. R.; Liu, S.; Wang, M. D. *Nat. Rev. Methods Primer* **2021**, *1* (1), 25. https://doi.org/10.1038/s43586-021-00021-6.
(39) Konermann, L.; Douglas, D. J. *J. Am. Soc. Mass Spectrom.* **1998**, *9* (12), 1248–1254. https://doi.org/10.1016/S1044-0305(98)00103-2.
(40) Konermann, L.; Douglas, D. J. *Rapid Commun. Mass Spectrom.* **1998**, *12* (8), 435–442. https://doi.org/10.1002/(SICI)1097-0231(19980430)12:8<435::AID-RCM181>3.0.CO;2-F.
(41) Konermann, L.; Douglas, D. J. *Biochemistry* **1997**, *36* (40), 12296–12302. https://doi.org/10.1021/bi971266u.
(42) Konermann, L.; Collings, B. A.; Douglas, D. J. *Biochemistry* **1997**, *36* (18), 5554–5559. https://doi.org/10.1021/bi970046d.
(43) Bleiholder, C.; Liu, F. C. *J. Phys. Chem. B* **2019**, *123* (13), 2756–2769. https://doi.org/10.1021/acs.jpcb.8b11818.

(44) Harrilal, C. P.; Gandhi, V. D.; Nagy, G.; Chen, X.; Buchanan, M. G.; Wojcik, R.; Conant, C. R.; Donor, M. T.; Ibrahim, Y. M.; Garimella, S. V. B.; Smith, R. D.; Larriba-Andaluz, C. *Anal. Chem.* **2021**, *93* (45), 14966–14975. https://doi.org/10.1021/acs.analchem.1c01736.

(45) Harrilal, C. P.; Garimella, S. V. B.; Chun, J.; Devanathan, N.; Zheng, X.; Ibrahim, Y. M.; Larriba-Andaluz, C.; Schenter, G.; Smith, R. D. *J. Phys. Chem. A* **2023**, *127* (25), 5458–5469. https://doi.org/10.1021/acs.jpca.3c01264.

(46) D'Imprima, E.; Kühlbrandt, W. *Q. Rev. Biophys.* **2021**, *54,* e4. https://doi.org/10.1017/S0033583521000020.

(47) Boswell, Z. K.; Latham, M. P. *Biochemistry* **2019**, *58* (3), 144–155. https://doi.org/10.1021/acs.biochem.8b00953.

(48) Hu, Y.; Cheng, K.; He, L.; Zhang, X.; Jiang, B.; Jiang, L.; Li, C.; Wang, G.; Yang, Y.; Liu, M. *Anal. Chem.* **2021**, *93* (4), 1866–1879. https://doi.org/10.1021/acs.analchem.0c03830.

(49) Lee, K. W.; Salome, A. Z.; Westphall, M. S.; Grant, T.; Coon, J. J. *J. Proteome Res.* **2023**, *22* (3), 851–856. https://doi.org/10.1021/acs.jproteome.2c00595.

(50) Seo, J.; Hoffmann, W.; Warnke, S.; Bowers, M. T.; Pagel, K.; von Helden, G. *Angew. Chem. Int. Ed.* **2016**, *55* (45), 14173–14176. https://doi.org/10.1002/anie.201606029.

(51) Servage, K. A.; Silveira, J. A.; Fort, K. L.; Russell, D. H. *J. Phys. Chem. B* **2015**, *119* (13), 4693–4698. https://doi.org/10.1021/jp512708u.

(52) Hamdy, O. M.; Julian, R. R. *J. Am. Soc. Mass Spectrom.* **2012**, *23* (1), 1–6. https://doi.org/10.1007/s13361-011-0284-8.

(53) Breuker, K.; McLafferty, F. W. *Proc. Natl. Acad. Sci.* **2008**, *105* (47), 18145–18152. https://doi.org/10.1073/pnas.0807005105.

(54) Chang, T. M.; Prell, J. S.; Warrick, E. R.; Williams, E. R. *J. Am. Chem. Soc.* **2012**, *134* (38), 15805–15813. https://doi.org/10.1021/ja304929h.

(55) Donor, M. T.; Wilson, J. W.; Shepherd, S. O.; Prell, J. S. *Int. J. Mass Spectrom.* **2021**, *469*, 116670. https://doi.org/10.1016/j.ijms.2021.116670.

(56) Dongré, A. R.; Jones, J. L.; Somogyi, Á.; Wysocki, V. H. *J. Am. Chem. Soc.* **1996**, *118* (35), 8365–8374. https://doi.org/10.1021/ja9542193.

(57) Miller, Z. M.; Zhang, J. D.; Donald, W. A.; Prell, J. S. *Anal. Chem.* **2020**, *92* (15), 10365–10374. https://doi.org/10.1021/acs.analchem.0c00613.

(58) Sinelnikov, I.; Kitova, E. N.; Klassen, J. S. *J. Am. Soc. Mass Spectrom.* **2007**, *18* (4), 617–631. https://doi.org/10.1016/j.jasms.2006.11.006.

(59) Julian, R. R.; Hodyss, R.; Beauchamp, J. L. *J. Am. Chem. Soc.* **2001**, *123* (15), 3577–3583. https://doi.org/10.1021/ja003105a.

(60) Wysocki, V. H.; Tsaprailis, G.; Smith, L. L.; Breci, L. A. *J. Mass Spectrom.* **2000**, *35* (12), 1399–1406. https://doi.org/10.1002/1096-9888(200012)35:12<1399::AID-JMS86>3.0.CO;2-R.

(61) Tsaprailis, G.; Nair, H.; Somogyi, Á.; Wysocki, V. H.; Zhong, W.; Futrell, J. H.; Summerfield, S. G.; Gaskell, S. J. *J. Am. Chem. Soc.* **1999**, *121* (22), 5142–5154. https://doi.org/10.1021/ja982980h.

(62) Meyer, B.; Papasotiriou, D. G.; Karas, M. *Amino Acids* **2011**, *41* (2), 291–310. https://doi.org/10.1007/s00726-010-0680-6.

(63) Lyon, Y. A.; Riggs, D.; Fornelli, L.; Compton, P. D.; Julian, R. R. *J. Am. Soc. Mass Spectrom.* **2018**, *29* (1), 150–157. https://doi.org/10.1007/s13361-017-1823-8.

(64) Panda, A.; Brown, C.; Gupta, K. *J. Am. Soc. Mass Spectrom.* **2023**. https://doi.org/10.1021/jasms.3c00110.
(65) Bush, M. F.; Hall, Z.; Giles, K.; Hoyes, J.; Robinson, C. V.; Ruotolo, B. T. *Anal. Chem.* **2010**, *82* (22), 9557–9565. https://doi.org/10.1021/ac1022953.
(66) Richardson, K.; Langridge, D.; Dixit, S. M.; Ruotolo, B. T. *Anal. Chem.* **2021**, *93* (7), 3542–3550. https://doi.org/10.1021/acs.analchem.0c04948.
(67) Gabelica, V.; Shvartsburg, A. A.; Afonso, C.; Barran, P.; Benesch, J. L. P.; Bleiholder, C.; Bowers, M. T.; Bilbao, A.; Bush, M. F.; Campbell, J. L.; Campuzano, I. D. G.; Causon, T.; Clowers, B. H.; Creaser, C. S.; De Pauw, E.; Far, J.; Fernandez-Lima, F.; Fjeldsted, J. C.; Giles, K.; Groessl, M.; Hogan Jr, C. J.; Hann, S.; Kim, H. I.; Kurulugama, R. T.; May, J. C.; McLean, J. A.; Pagel, K.; Richardson, K.; Ridgeway, M. E.; Rosu, F.; Sobott, F.; Thalassinos, K.; Valentine, S. J.; Wyttenbach, T. *Mass Spectrom. Rev.* **2019**, *38* (3), 291–320. https://doi.org/10.1002/mas.21585.
(68) Mortensen, D. N.; Susa, A. C.; Williams, E. R. *J. Am. Soc. Mass Spectrom.* **2017**, *28* (7), 1282–1292. https://doi.org/10.1007/s13361-017-1669-0.
(69) Donor, M. T.; Mroz, A. M.; Prell, J. S. *Chem. Sci.* **2019**, *10* (14), 4097–4106. https://doi.org/10.1039/C9SC00644C.
(70) Matney, R.; Gadkari, V. Evaluation of Surface Induced Dissociation as a Higher Energy Approach to Gas-Phase Unfolding and Development of “Complex-Down” Gas-Phase Unfolding, 2023.
(71) Laskin, J.; Futrell, J. H. *J. Am. Soc. Mass Spectrom.* **2003**, *14* (12), 1340–1347. https://doi.org/10.1016/j.jasms.2003.08.004.
(72) Price, W. D.; Schnier, P. D.; Jockusch, R. A.; Strittmatter, E. F.; Williams, E. R. *J. Am. Chem. Soc.* **1996**, *118* (43), 10640–10644. https://doi.org/10.1021/ja961812r.
(73) Rondeau, D.; Drahos, L.; Vékey, K. *Rapid Commun. Mass Spectrom.* **2014**, *28* (11), 1273–1284. https://doi.org/10.1002/rcm.6899.
(74) Naban-Maillet, J.; Lesage, D.; Bossée, A.; Gimbert, Y.; Sztáray, J.; Vékey, K.; Tabet, J.-C. *J. Mass Spectrom.* **2005**, *40* (1), 1–8. https://doi.org/10.1002/jms.773.
(75) Gabelica, V.; Pauw, E. D. *Mass Spectrom. Rev.* **2005**, *24* (4), 566–587. https://doi.org/10.1002/mas.20027.
(76) Gabelica, V.; De Pauw, E.; Karas, M. *Int. J. Mass Spectrom.* **2004**, *231* (2), 189–195. https://doi.org/10.1016/j.ijms.2003.10.010.
(77) Collette, C.; De Pauw, E. *Rapid Commun. Mass Spectrom.* **1998**, *12* (4), 165–170. https://doi.org/10.1002/(SICI)1097-0231(19980227)12:4<165::AID-RCM140>3.0.CO;2-1.
(78) Laskin, J.; Byrd, M.; Futrell, J. *Int. J. Mass Spectrom.* **2000**, *195–196*, 285–302. https://doi.org/10.1016/S1387-3806(99)00185-2.
(79) Armentrout, P. B. *Int. J. Mass Spectrom.* **2000**, *200* (1–3), 219–241. https://doi.org/10.1016/S1387-3806(00)00310-9.
(80) Carpenter, J. E.; McNary, C. P.; Furin, A.; Sweeney, A. F.; Armentrout, P. B. *J. Am. Soc. Mass Spectrom.* **2017**, *28* (9), 1876–1888. https://doi.org/10.1007/s13361-017-1693-0.
(81) Cooks, G.; Patrick, J.; Kotiaho, T.; McLuckey, S. *Mass Spectrom. Rev.* **1994**, *13* (4), 287–339. https://doi.org/10.1002/mas.1280130402.
(82) Stephens, E. R.; Dumlao, M.; Xiao, D.; Zhang, D.; Donald, W. A. *J. Am. Soc. Mass Spectrom.* **2015**, *26* (12), 2081–2084. https://doi.org/10.1007/s13361-015-1272-1.

(83) Barylyuk, K. V.; Chingin, K.; Balabin, R. M.; Zenobi, R. *J. Am. Soc. Mass Spectrom.* **2010**, *21* (1), 172–177. https://doi.org/10.1016/j.jasms.2009.09.023.

(84) Sztáray, J.; Memboeuf, A.; Drahos, L.; Vékey, K. *Mass Spectrom. Rev.* **2011**, *30* (2), 298–320. https://doi.org/10.1002/mas.20279.

(85) Merenbloom, S. I.; Flick, T. G.; Williams, E. R. *J. Am. Soc. Mass Spectrom.* **2012**, *23* (3), 553–562. https://doi.org/10.1007/s13361-011-0313-7.

(86) Polasky, D. A.; Dixit, S. M.; Fantin, S. M.; Ruotolo, B. T. *Anal. Chem.* **2019**, *91* (4), 3147–3155. https://doi.org/10.1021/acs.analchem.8b05762.

(87) Kertesz, T. M.; Hall, L. H.; Hill, D. W.; Grant, D. F. *J. Am. Soc. Mass Spectrom.* **2009**, *20* (9), 1759–1767. https://doi.org/10.1016/j.jasms.2009.06.002.

(88) Seffernick, J. T.; Turzo, S. B. A.; Harvey, S. R.; Kim, Y.; Somogyi, Á.; Marciano, S.; Wysocki, V. H.; Lindert, S. *Anal. Chem.* **2022**, *94* (29), 10506–10514. https://doi.org/10.1021/acs.analchem.2c01869.

(89) Ma, X.; Zhou, M.; Wysocki, V. H. *J. Am. Soc. Mass Spectrom.* **2014**, *25* (3), 368–379. https://doi.org/10.1007/s13361-013-0790-y.

(90) Gadkari, V. V.; Juliano, B. R.; Mallis, C. S.; May, J. C.; Kurulugama, R. T.; Fjeldsted, J. C.; McLean, J. A.; Russell, D. H.; Ruotolo, B. T. *Analyst* **2023**, *148* (2), 391–401. https://doi.org/10.1039/D2AN01452A.

(91) Armentrout, P. B.; Ervin, K. M.; Rodgers, M. T. *J. Phys. Chem. A* **2008**, *112* (41), 10071–10085. https://doi.org/10.1021/jp805343h.

(92) Ghiassee, M.; Christensen, E. G.; Fenn, T.; Armentrout, P. B. *J. Phys. Chem. A* **2023**, *127* (1), 169–180. https://doi.org/10.1021/acs.jpca.2c07638.

(93) Armentrout, P. B. *Mass Spectrom. Rev.* **2023**, *42* (3), 928–953. https://doi.org/10.1002/mas.21723.

(94) Kafle, A.; Armentrout, P. B. *Inorg. Chem.* **2022**, *61* (40), 15936–15952. https://doi.org/10.1021/acs.inorgchem.2c02138.

(95) Demireva, M.; Armentrout, P. B. *J. Phys. Chem. A* **2021**, *125* (14), 2849–2865. https://doi.org/10.1021/acs.jpca.0c11540.

(96) Mookherjee, A.; Armentrout, P. B. *J. Am. Soc. Mass Spectrom.* **2022**, *33* (2), 355–368. https://doi.org/10.1021/jasms.1c00345.

(97) Rahrt, R.; Auth, T.; Demireva, M.; Armentrout, P. B.; Koszinowski, K. *Anal. Chem.* **2019**, *91* (18), 11703–11711. https://doi.org/10.1021/acs.analchem.9b02257.

(98) Moision, R. M.; Armentrout, P. B. *J. Am. Soc. Mass Spectrom.* **2007**, *18* (6), 1124–1134. https://doi.org/10.1016/j.jasms.2007.03.011.

(99) Price, W. D.; Schnier, P. D.; Williams, E. R. *Anal. Chem.* **1996**, *68* (5), 859–866. https://doi.org/10.1021/ac951038a.

(100) Rolland, A. D.; Prell, J. S. *TrAC Trends Anal. Chem.* **2019**, *116*, 282–291. https://doi.org/10.1016/j.trac.2019.04.023.

(101) Vahidi, S.; Stocks, B. B.; Konermann, L. *Anal. Chem.* **2013**, *85* (21), 10471–10478. https://doi.org/10.1021/ac402490r.

(102) Cheung See Kit, M.; Shepherd, S. O.; Prell, J. S.; Webb, I. K. *J. Am. Soc. Mass Spectrom.* **2021**, *32* (9), 2313–2321. https://doi.org/10.1021/jasms.1c00025.

(103) Wollnik, H. *Int. J. Mass Spectrom.* **2013**, *349–350*, 38–46. https://doi.org/10.1016/j.ijms.2013.04.023.

(104) Gale, P. J.; Vestal, M. L. The Development of Time-of-Flight Mass Spectrometry. In *The Encyclopedia of Mass Spectrometry*; Gross, M. L., Caprioli, R. M., Eds.; Elsevier: Boston, 2016; pp 34–42. https://doi.org/10.1016/B978-0-08-043848-1.00005-5.
(105) Wiley, W. C.; McLaren, I. H. *Rev. Sci. Instrum.* **1955**, *26* (12), 1150–1157. https://doi.org/10.1063/1.1715212.
(106) Comisarow, M. B.; Marshall, A. G. *J. Chem. Phys.* **1976**, *64* (1), 110–119. https://doi.org/10.1063/1.431959.
(107) Comisarow, M. B. *J. Chem. Phys.* **2008**, *69* (9), 4097–4104. https://doi.org/10.1063/1.437143.
(108) Marshall, A. G.; Comisarow, M. B.; Parisod, G. *J. Chem. Phys.* **1979**, *71* (11), 4434–4444. https://doi.org/10.1063/1.438196.
(109) Marshall, A. G.; Wang, T. C. L.; Ricca, T. L. *J. Am. Chem. Soc.* **1985**, *107* (26), 7893–7897. https://doi.org/10.1021/ja00312a015.
(110) Skeene, K.; Khatri, K.; Soloviev, Z.; Lapthorn, C. *Biochim. Biophys. Acta BBA - Proteins Proteomics* **2021**, *1869* (12), 140697. https://doi.org/10.1016/j.bbapap.2021.140697.
(111) Donnelly, D. P.; Rawlins, C. M.; DeHart, C. J.; Fornelli, L.; Schachner, L. F.; Lin, Z.; Lippens, J. L.; Aluri, K. C.; Sarin, R.; Chen, B.; Lantz, C.; Jung, W.; Johnson, K. R.; Koller, A.; Wolff, J. J.; Campuzano, I. D. G.; Auclair, J. R.; Ivanov, A. R.; Whitelegge, J. P.; Paša-Tolić, L.; Chamot-Rooke, J.; Danis, P. O.; Smith, L. M.; Tsybin, Y. O.; Loo, J. A.; Ge, Y.; Kelleher, N. L.; Agar, J. N. *Nat. Methods* **2019**, *16* (7), 587–594. https://doi.org/10.1038/s41592-019-0457-0.
(112) Laszlo, K. J.; Munger, E. B.; Bush, M. F. *J. Am. Chem. Soc.* **2016**, *138* (30), 9581–9588. https://doi.org/10.1021/jacs.6b04282.
(113) Mark, L. P.; Gill, M. C.; Mahut, M.; Derrick, P. J. *Eur. J. Mass Spectrom.* **2012**, *18* (5), 439–446. https://doi.org/10.1255/ejms.1198.
(114) N. Moore, B.; J. Blanksby, S.; R. Julian, R. *Chem. Commun.* **2009**, *0* (33), 5015–5017. https://doi.org/10.1039/B907833A.
(115) Yost, R. A.; Enke, C. G. *Anal. Chem.* **1979**, *51* (12), 1251–1264. https://doi.org/10.1021/ac50048a002.
(116) Perchalski, R. J.; Yost, R. A.; Wilder, B. J. *Anal. Chem.* **1982**, *54* (9), 1466–1471. https://doi.org/10.1021/ac00246a006.
(117) Dolnikowski, G. G.; Kristo, M. J.; Enke, C. G.; Watson, J. T. *Int. J. Mass Spectrom. Ion Process.* **1988**, *82* (1), 1–15. https://doi.org/10.1016/0168-1176(88)80001-6.
(118) Zubarev, R. A.; Kelleher, N. L.; McLafferty, F. W. *J. Am. Chem. Soc.* **1998**, *120* (13), 3265–3266. https://doi.org/10.1021/ja973478k.
(119) Leib, R. D.; Donald, W. A.; Bush, M. F.; O'Brie, J. T.; Williams, E. R. *J. Am. Chem. Soc.* **2007**, *129* (16), 4894–4895. https://doi.org/10.1021/ja0666607.
(120) Cooper, H. J.; Håkansson, K.; Marshall, A. G. *Mass Spectrom. Rev.* **2005**, *24* (2), 201–222. https://doi.org/10.1002/mas.20014.
(121) Williams, J. P.; Morrison, L. J.; Brown, J. M.; Beckman, J. S.; Voinov, V. G.; Lermyte, F. *Anal. Chem.* **2020**, *92* (5), 3674–3681. https://doi.org/10.1021/acs.analchem.9b04763.
(122) Lermyte, F.; Valkenborg, D.; Loo, J. A.; Sobott, F. *Mass Spectrom. Rev.* **2018**, *37* (6), 750–771. https://doi.org/10.1002/mas.21560.
(123) Loo, J. A.; Edmonds, C. G.; Udseth, H. R.; Smith, R. D. *Anal. Chim. Acta* **1990**, *241* (2), 167–173. https://doi.org/10.1016/S0003-2670(00)83644-2.

(124) Smith, R. D.; Loa, J. A.; Barinaga, C. J.; Edmonds, C. G.; Udseth, H. R. *J. Am. Soc. Mass Spectrom.* **1990**, *1* (1), 53–65. https://doi.org/10.1016/1044-0305(90)80006-9.
(125) Zhai, H.; Han, X.; Breuker, K.; McLafferty, F. W. *Anal. Chem.* **2005**, *77* (18), 5777–5784. https://doi.org/10.1021/ac0580215.
(126) Schmidt, A.; Bahr, U.; Karas, M. *Anal. Chem.* **2001**, *73* (24), 6040–6046. https://doi.org/10.1021/ac010451h.
(127) Harrison, J. A.; Pruška, A.; Bittner, P.; Muck, A.; Cooper-Shepherd, D. A.; Zenobi, R. *Anal. Chem.* **2022**, *94* (36), 12435–12443. https://doi.org/10.1021/acs.analchem.2c02406.
(128) Gross, D. S.; Zhao, Y.; William, E. R. *J. Am. Soc. Mass Spectrom.* **1997**, *8* (5), 519–524. https://doi.org/10.1016/S1044-0305(97)00010-X.
(129) Biemann, K.; Scoble, H. A. *Science* **1987**, *237* (4818), 992–998. https://doi.org/10.1126/science.3303336.
(130) Johnson, R. S.; Martin, S. A.; Biemann, Klaus.; Stults, J. T.; Watson, J. Throck. *Anal. Chem.* **1987**, *59* (21), 2621–2625. https://doi.org/10.1021/ac00148a019.
(131) Yamashita, M.; Fenn, J. B. *J. Phys. Chem.* **1984**, *88* (20), 4451–4459. https://doi.org/10.1021/j150664a002.
(132) Yamashita, M.; Fenn, J. B. *J. Phys. Chem.* **1984**, *88* (20), 4671–4675. https://doi.org/10.1021/j150664a046.
(133) Dole, M.; Mack, L. L.; Hines, R. L.; Mobley, R. C.; Ferguson, L. D.; Alice, M. B. *J. Chem. Phys.* **1968**, *49* (5), 2240–2249. https://doi.org/10.1063/1.1670391.
(134) Fenn, J. B. *Angew. Chem. Int. Ed.* **2003**, *42* (33), 3871–3894. https://doi.org/10.1002/anie.200300605.
(135) Whitehouse, C. M.; Dreyer, R. N.; Yamashita, Masamichi.; Fenn, J. B. *Anal. Chem.* **1985**, *57* (3), 675–679. https://doi.org/10.1021/ac00280a023.
(136) Biemann, K. *Biomed. Environ. Mass Spectrom.* **1988**, *16* (1–12), 99–111. https://doi.org/10.1002/bms.1200160119.
(137) Wilm, M. S.; Mann, M. *Int. J. Mass Spectrom. Ion Process.* **1994**, *136* (2), 167–180. https://doi.org/10.1016/0168-1176(94)04024-9.
(138) Rogawski, R.; Sharon, M. *Chem. Rev.* **2022**, *122* (8), 7386–7414. https://doi.org/10.1021/acs.chemrev.1c00217.
(139) Largy, E.; König, A.; Ghosh, A.; Ghosh, D.; Benabou, S.; Rosu, F.; Gabelica, V. *Chem. Rev.* **2022**, *122* (8), 7720–7839. https://doi.org/10.1021/acs.chemrev.1c00386.
(140) Ebberink, E. H. T. M.; Ruisinger, A.; Nuebel, M.; Thomann, M.; Heck, A. J. R. *Mol. Ther. - Methods Clin. Dev.* **2022**, *27*, 491–501. https://doi.org/10.1016/j.omtm.2022.11.003.
(141) Hammerschmid, D.; van Dyck, J. F.; Sobott, F.; Calabrese, A. N. .
(142) Laganowsky, A.; Reading, E.; Hopper, J. T. S.; Robinson, C. V. *Nat. Protoc.* **2013**, *8* (4), 639–651. https://doi.org/10.1038/nprot.2013.024.
(143) Martens, C.; Stein, R. A.; Masureel, M.; Roth, A.; Mishra, S.; Dawaliby, R.; Konijnenberg, A.; Sobott, F.; Govaerts, C.; Mchaourab, H. S. *Nat. Struct. Mol. Biol.* **2016**, *23* (8), 744–751. https://doi.org/10.1038/nsmb.3262.
(144) Marty, M. T.; Hoi, K. K.; Gault, J.; Robinson, C. V. *Angew. Chem. Int. Ed.* **2016**, *55* (2), 550–554. https://doi.org/10.1002/anie.201508289.
(145) Iavarone, A. T.; Williams, E. R. *J. Am. Chem. Soc.* **2003**, *125* (8), 2319–2327. https://doi.org/10.1021/ja021202t.
(146) Tang, K.; Smith, R. D. *J. Am. Soc. Mass Spectrom.* **2001**, *12* (3), 343–347. https://doi.org/10.1016/S1044-0305(01)00222-7.

(147) Tang, K.; Page, J. S.; Smith, R. D. *J. Am. Soc. Mass Spectrom.* **2004**, *15* (10), 1416–1423. https://doi.org/10.1016/j.jasms.2004.04.034.
(148) Gomez, A.; Tang, K. *Phys. Fluids* **1994**, *6* (1), 404–414. https://doi.org/10.1063/1.868037.
(149) Benkestock, K.; Sundqvist, G.; Edlund, P.-O.; Roeraade, J. *J. Mass Spectrom.* **2004**, *39* (9), 1059–1067. https://doi.org/10.1002/jms.685.
(150) Yen, H.-Y.; Abramsson, M. L.; Agasid, M. T.; Lama, D.; Gault, J.; Liko, I.; Kaldmäe, M.; Saluri, M.; Qureshi, A. A.; Suades, A.; Drew, D.; Degiacomi, M. T.; Marklund, E. G.; Allison, T. M.; Robinson, C. V.; Landreh, M. *RSC Adv.* **2022**, *12* (16), 9671–9680. https://doi.org/10.1039/D2RA01282K.
(151) Consta, S.; Oh, M. I.; Malevanets, A. *Chem. Phys. Lett.* **2016**, *663*, 1–12. https://doi.org/10.1016/j.cplett.2016.08.001.
(152) Sterling, H. J.; Cassou, C. A.; Susa, A. C.; Williams, E. R. *Anal. Chem.* **2012**, *84* (8), 3795–3801. https://doi.org/10.1021/ac300468a.
(153) Sharawy, M.; Consta, S. *Phys. Chem. Chem. Phys.* **2015**, *17* (38), 25550–25562. https://doi.org/10.1039/C5CP04331J.
(154) Ogorzalek Loo, R. R.; Lakshmanan, R.; Loo, J. A. *J. Am. Soc. Mass Spectrom.* **2014**, *25* (10), 1675–1693. https://doi.org/10.1007/s13361-014-0965-1.
(155) Consta, S.; Malevanets, A. *Phys. Rev. Lett.* **2012**, *109* (14), 148301. https://doi.org/10.1103/PhysRevLett.109.148301.
(156) Fernández De La Mora, J. *Annu. Rev. Fluid Mech.* **2007**, *39* (1), 217–243. https://doi.org/10.1146/annurev.fluid.39.050905.110159.
(157) Fernandez de la Mora, J. *Anal. Chim. Acta* **2000**, *406* (1), 93–104. https://doi.org/10.1016/S0003-2670(99)00601-7.
(158) Perez-Lorenzo, L. J.; Fernandez De La Mora, J. *J. Fluid Mech.* **2022**, *931*, A4. https://doi.org/10.1017/jfm.2021.771.
(159) Cech, N. B.; Enke, C. G. *Mass Spectrom. Rev.* **2001**, *20* (6), 362–387. https://doi.org/10.1002/mas.10008.
(160) Aliyari, E.; Konermann, L. *Anal. Chem.* **2022**, *94* (21), 7713–7721. https://doi.org/10.1021/acs.analchem.2c01355.
(161) Iribarne, J. V.; Thomson, B. A. *J. Chem. Phys.* **1976**, *64* (6), 2287–2294. https://doi.org/10.1063/1.432536.
(162) Thomson, B. A.; Iribarne, J. V. *J. Chem. Phys.* **1979**, *71* (11), 4451–4463. https://doi.org/10.1063/1.438198.
(163) Konermann, L.; Metwally, H.; Duez, Q.; Peters, I. *Analyst* **2019**, *144* (21), 6157–6171. https://doi.org/10.1039/C9AN01201J.
(164) Winger, B. E.; Light-Wahl, K. J.; Ogorzalek Loo, R. R.; Udseth, H. R.; Smith, R. D. *J. Am. Soc. Mass Spectrom.* **1993**, *4* (7), 536–545. https://doi.org/10.1016/1044-0305(93)85015-P.
(165) Konermann, L.; Rodriguez, A. D.; Liu, J. *Anal. Chem.* **2012**, *84* (15), 6798–6804. https://doi.org/10.1021/ac301298g.
(166) Jordan, J. S.; Xia, Z.; Williams, E. R. *J. Am. Soc. Mass Spectrom.* **2022**, *33* (3), 607–611. https://doi.org/10.1021/jasms.1c00372.
(167) Davidson, K. L.; Oberreit, D. R.; Hogan, C. J.; Bush, M. F. *Int. J. Mass Spectrom.* **2017**, *420*, 35–42. https://doi.org/10.1016/j.ijms.2016.09.013.

(168) Kostelic, M. M.; Hsieh, C.-C.; Sanders, H. M.; Zak, C. K.; Ryan, J. P.; Baker, E. S.; Aspinwall, C. A.; Marty, M. T. *J. Am. Soc. Mass Spectrom.* **2022**, *33* (6), 1031–1037. https://doi.org/10.1021/jasms.2c00087.
(169) Iavarone, A. T.; Udekwu, O. A.; Williams, E. R. *Anal. Chem.* **2004**, *76* (14), 3944–3950. https://doi.org/10.1021/ac049724+.
(170) Kostelic, M. M.; Marty, M. T. Deconvolving Native and Intact Protein Mass Spectra with UniDec. In *Proteoform Identification: Methods and Protocols*; Sun, L., Liu, X., Eds.; Methods in Molecular Biology; Springer US: New York, NY, 2022; pp 159–180. https://doi.org/10.1007/978-1-0716-2325-1_12.
(171) Marty, M. T.; Baldwin, A. J.; Marklund, E. G.; Hochberg, G. K. A.; Benesch, J. L. P.; Robinson, C. V. *Anal. Chem.* **2015**, *87* (8), 4370–4376. https://doi.org/10.1021/acs.analchem.5b00140.
(172) Labowsky, M.; Whitehouse, C.; Fenn, J. B. *Rapid Commun. Mass Spectrom.* **1993**, *7* (1), 71–84. https://doi.org/10.1002/rcm.1290070117.
(173) Nguyen, G. T. H.; Tran, T. N.; Podgorski, M. N.; Bell, S. G.; Supuran, C. T.; Donald, W. A. *ACS Cent. Sci.* **2019**, *5* (2), 308–318. https://doi.org/10.1021/acscentsci.8b00787.
(174) Verbeck, G.; Hoffmann, W.; Walton, B. *Analyst* **2012**, *137* (19), 4393–4407. https://doi.org/10.1039/C2AN35550G.
(175) Gologan, B.; Takáts, Z.; Alvarez, J.; Wiseman, J.; Talaty, N.; Ouyang, Z.; Cooks, R. *J. Am. Soc. Mass Spectrom.* **2004**. https://doi.org/10.1016/J.JASMS.2004.09.005.
(176) Lomeli, S. H.; Yin, S.; Ogorzalek Loo, R. R.; Loo, J. A. *J. Am. Soc. Mass Spectrom.* **2009**, *20* (4), 593–596. https://doi.org/10.1016/j.jasms.2008.11.013.
(177) Gadzuk-Shea, M. M.; Hubbard, E. E.; Gozzo, T. A.; Bush, M. F. *J. Am. Soc. Mass Spectrom.* **2023**. https://doi.org/10.1021/jasms.3c00147.
(178) Laskin, J. *J. Phys. Chem. A* **2006**, *110* (27), 8554–8562. https://doi.org/10.1021/jp057229r.
(179) Jia, M.; Song, Y.; Du, C.; Wysocki, V. H. *J. Am. Soc. Mass Spectrom.* **2023**, *34* (10), 2166–2175. https://doi.org/10.1021/jasms.3c00142.
(180) Loo, J.; Sannes-Lowery, K. A.; Hu, P.; Mack, D. P.; Mei, H.-Y. STUDYING NONCOVALENT PROTEIN-RNA INTERACTIONS AND DRUG BINDING BY ELECTROSPRAY IONIZATION MASS SPECTROMETRY. In *New Methods for the Study of Biomolecular Complexes*.
(181) Rondeau, D.; Galland, N.; Zins, E.-L.; Pepe, C.; Drahos, L.; Vékey, K. *J. Mass Spectrom.* **2011**, *46* (2), 100–111. https://doi.org/10.1002/jms.1873.
(182) Pak, A.; Lesage, D.; Gimbert, Y.; Vékey, K.; Tabet, J.-C. *J. Mass Spectrom.* **2008**, *43* (4), 447–455. https://doi.org/10.1002/jms.1330.
(183) Mora, J. F. de la; Van Berkel, G. J.; Enke, C. G.; Cole, R. B.; Martinez-Sanchez, M.; Fenn, J. B. *J. Mass Spectrom.* **2000**, *35* (8), 939–952. https://doi.org/10.1002/1096-9888(200008)35:8<939::AID-JMS36>3.0.CO;2-V.
(184) Loo, J.; Ogorzalek Loo, R. R. *Proc. 43rd ASMS Conf. Mass Spectrom. Allied Top. Atlanta Ga. May 21-26 1995.*
(185) Gadkari, V. V.; Ramírez, C. R.; Vallejo, D. D.; Kurulugama, R. T.; Fjeldsted, J. C.; Ruotolo, B. T. *Anal. Chem.* **2020**, *92* (23), 15489–15496. https://doi.org/10.1021/acs.analchem.0c03372.
(186) Donor, M. T.; Shepherd, S. O.; Prell, J. S. *J. Am. Soc. Mass Spectrom.* **2020**, *31* (3), 602–610. https://doi.org/10.1021/jasms.9b00055.

(187) Schnier, P. D.; Jurchen, J. C.; Williams, E. R. *J. Phys. Chem. B* **1999**, *103* (4), 737–745. https://doi.org/10.1021/jp9833193.

(188) Schnier, P. D.; Price, W. D.; Jockusch, R. A.; Williams, E. R. *J. Am. Chem. Soc.* **1996**, *118* (30), 7178–7189. https://doi.org/10.1021/ja9609157.

(189) Kitova, E. N.; Sinelnikov, I.; Deng, L.; Klassen, J. S. *Int. J. Mass Spectrom.* **2013**, *345–347*, 97–103. https://doi.org/10.1016/j.ijms.2012.08.025.

(190) Muntean, F.; Armentrout, P. B. *J. Chem. Phys.* **2001**, *115* (3), 1213–1228. https://doi.org/10.1063/1.1371958.

(191) Uggerud, E.; Derrick, P. J. *J. Phys. Chem.* **1991**, *95* (3), 1430–1436. https://doi.org/10.1021/j100156a073.

(192) Bordas-Nagy, J.; Jennings, K. R. *Int. J. Mass Spectrom. Ion Process.* **1990**, *100*, 105–131. https://doi.org/10.1016/0168-1176(90)85071-9.

(193) Watkins, H.; Koski, W. *Chemical Physics Letters* **1980**, *77* (3).

(194) Teloy, E.; Gerlich, D. *Chemical Physics* **1974**, *4*, 417–427.

(195) T. Snyder, D.; J. Jones, B.; Lin, Y.-F.; A. Cooper-Shepherd, D.; Hewitt, D.; Wildgoose, J.; M. Brown, J.; I. Langridge, J.; H. Wysocki, V. *Analyst* **2021**, *146* (22), 6861–6873. https://doi.org/10.1039/D1AN01407B.

(196) Snyder, D. T.; Panczyk, E. M.; Somogyi, A.; Kaplan, D. A.; Wysocki, V. *Anal. Chem.* **2020**, *92* (16), 11195–11203. https://doi.org/10.1021/acs.analchem.0c01657.

(197) Stow, S. M.; Causon, T. J.; Zheng, X.; Kurulugama, R. T.; Mairinger, T.; May, J. C.; Rennie, E. E.; Baker, E. S.; Smith, R. D.; McLean, J. A.; Hann, S.; Fjeldsted, J. C. *Anal. Chem.* **2017**, *89* (17), 9048–9055. https://doi.org/10.1021/acs.analchem.7b01729.

(198) Thomas, C. L. P.; Rezgui, N. D.; Kanu, A. B.; Munro, W. A. **2002**.

(199) Zhong, Y.; Hyung, S.-J.; Ruotolo, B. T. *Analyst* **2011**, *136* (17), 3534–3541. https://doi.org/10.1039/C0AN00987C.

(200) Shvartsburg, A. A.; Smith, R. D. *Anal. Chem.* **2008**, *80* (24), 9689–9699. https://doi.org/10.1021/ac8016295.

(201) Dixit, S. M.; Ruotolo, B. T. *J. Am. Soc. Mass Spectrom.* **2019**, *30* (6), 956–966. https://doi.org/10.1007/s13361-019-02133-6.

(202) Rolland, A. D.; Takata, T.; Donor, M. T.; Lampi, K. J.; Prell, J. S. *Structure* **2023**, S0969212623002095. https://doi.org/10.1016/j.str.2023.06.013.

(203) Johnson, A. R.; Carlson, E. E. *Anal. Chem.* **2015**, *87* (21), 10668–10678. https://doi.org/10.1021/acs.analchem.5b01543.

(204) Wells, J. M.; McLuckey, S. A. *Methods Enzymol.* **2005**, *402*, 148–185. https://doi.org/10.1016/S0076-6879(05)02005-7.

(205) Laskin, J.; Denisov, E. V.; Shukla, A. K.; Barlow, S. E.; Futrell, J. H. *Anal. Chem.* **2002**, *74* (14), 3255–3261. https://doi.org/10.1021/ac025514q.

(206) Sipe, S. N.; Jeanne Dit Fouque, K.; Garabedian, A.; Leng, F.; Fernandez-Lima, F.; Brodbelt, J. S. *J. Am. Soc. Mass Spectrom.* **2022**, *33* (7), 1092–1102. https://doi.org/10.1021/jasms.2c00083.

(207) Jeanne Dit Fouque, K.; Sipe, S. N.; Garabedian, A.; Mejia, G.; Su, L.; Hossen, M. L.; Chapagain, P. P.; Leng, F.; Brodbelt, J. S.; Fernandez-Lima, F. *J. Am. Soc. Mass Spectrom.* **2022**, *33* (7), 1103–1112. https://doi.org/10.1021/jasms.2c00101.

(208) Rodgers, M. T.; Armentrout, P. B. *J. Phys. Chem. A* **1997**, *101* (7), 1238–1249. https://doi.org/10.1021/jp962170x.

(209) Laskin, J.; Denisov, E.; Futrell, J. *J. Phys. Chem. B* **2001**, *105* (9), 1895–1900. https://doi.org/10.1021/jp004153k.
(210) Rodgers, M. T.; Ervin, K. M.; Armentrout, P. B. *J. Chem. Phys.* **1997**, *106* (11), 4499–4508. https://doi.org/10.1063/1.473494.
(211) Hales, D. A.; Lian, L.; Armentrout, P. B. *Int. J. Mass Spectrom. Ion Process.* **1990**, *102*, 269–301. https://doi.org/10.1016/0168-1176(90)80065-B.
(212) Chrisman, P. A.; Newton, K. A.; Reid, G. E.; Wells, J. M.; McLuckey, S. A. *Rapid Commun. Mass Spectrom.* **2001**, *15* (23), 2334–2340. https://doi.org/10.1002/rcm.512.
(213) Shoff, T. A.; Julian, R. R. *J. Am. Soc. Mass Spectrom.* **2023**. https://doi.org/10.1021/jasms.3c00196.
(214) Kelleher, N. L.; Lin, H. Y.; Valaskovic, G. A.; Aaserud, D. J.; Fridriksson, E. K.; McLafferty, F. W. *J. Am. Chem. Soc.* **1999**, *121* (4), 806–812. https://doi.org/10.1021/ja973655h.
(215) Bennett, J. L.; Nguyen, G. T. H.; Donald, W. A. *Chem. Rev.* **2022**, *122* (8), 7327–7385. https://doi.org/10.1021/acs.chemrev.1c00293.
(216) Cong, X.; Liu, Y.; Liu, W.; Liang, X.; Russell, D. H.; Laganowsky, A. *J. Am. Chem. Soc.* **2016**, *138* (13), 4346–4349. https://doi.org/10.1021/jacs.6b01771.
(217) Allison, T. M.; Reading, E.; Liko, I.; Baldwin, A. J.; Laganowsky, A.; Robinson, C. V. *Nat. Commun.* **2015**, *6* (1), 8551. https://doi.org/10.1038/ncomms9551.
(218) El-Hawiet, A.; Kitova, E. N.; Arutyunov, D.; Simpson, D. J.; Szymanski, C. M.; Klassen, J. S. *Anal. Chem.* **2012**, *84* (9), 3867–3870. https://doi.org/10.1021/ac3005082.
(219) Hyung, S.-J.; Robinson, C. V.; Ruotolo, B. T. *Chem. Biol.* **2009**, *16* (4), 382–390. https://doi.org/10.1016/j.chembiol.2009.02.008.
(220) Hu, P.; Loo, J. A. *J. Am. Chem. Soc.* **1995**, *117* (45), 11314–11319. https://doi.org/10.1021/ja00150a032.
(221) Bornschein, R. E.; Ruotolo, B. T. *Analyst* **2015**, *140* (20), 7020–7029. https://doi.org/10.1039/C5AN01242B.
(222) Light-Wahl, K. J.; Schwartz, B. L.; Smith, R. D. *J. Am. Chem. Soc.* **1994**, *116* (12), 5271–5278. https://doi.org/10.1021/ja00091a035.
(223) Polfer, N. C.; Oomens, J.; Suhai, S.; Paizs, B. *J. Am. Chem. Soc.* **2007**, *129* (18), 5887–5897. https://doi.org/10.1021/ja068014d.
(224) Boyd, R.; Somogyi, Á. *J. Am. Soc. Mass Spectrom.* **2010**, *21* (8), 1275–1278. https://doi.org/10.1016/j.jasms.2010.04.017.
(225) van Schaick, G.; Domínguez-Vega, E.; Castel, J.; Wuhrer, M.; Hernandez-Alba, O.; Cianférani, S. *Anal. Chem.* **2023**, *95* (8), 3932–3939. https://doi.org/10.1021/acs.analchem.2c03163.
(226) Malhotra, P.; Udgaonkar, J. B. *Protein Sci.* **2016**, *25* (11), 1924–1941. https://doi.org/10.1002/pro.3015.
(227) Zhong, Y.; Han, L.; Ruotolo, B. T. *Angew. Chem. Int. Ed.* **2014**, *53* (35), 9209–9212. https://doi.org/10.1002/anie.201403784.
(228) Douglas, D. J. *J. Am. Soc. Mass Spectrom.* **1998**, *9* (2), 101–113. https://doi.org/10.1016/S1044-0305(97)00246-8.
(229) Edwards, A. N.; Tran, H. M.; Gallagher, E. S. *J. Am. Soc. Mass Spectrom.* **2021**, *32* (11), 2621–2630. https://doi.org/10.1021/jasms.1c00144.
(230) Hong, S.; Bush, M. F. *J. Am. Soc. Mass Spectrom.* **2019**, *30* (11), 2430–2437. https://doi.org/10.1007/s13361-019-02326-z.

(231) Wang, H.; Eschweiler, J.; Cui, W.; Zhang, H.; Frieden, C.; Ruotolo, B. T.; Gross, M. L. *J. Am. Soc. Mass Spectrom.* **2019**, *30* (5), 876–885. https://doi.org/10.1007/s13361-019-02148-z.
(232) Zercher, B. P.; Hong, S.; Roush, A. E.; Feng, Y.; Bush, M. F. *Anal. Chem.* **2023**, *95* (25), 9589–9597. https://doi.org/10.1021/acs.analchem.3c01222.
(233) Wysocki, V. H.; Kenttämaa, H. I.; Cooks, R. G. *Int. J. Mass Spectrom. Ion Process.* **1987**, *75* (2), 181–208. https://doi.org/10.1016/0168-1176(87)83054-9.
(234) MARjcp52b.Pdf.
(235) Laskin, J.; Futrell, J. *J. Phys. Chem. A* **2000**, *104* (23), 5484–5494. https://doi.org/10.1021/jp000281x.
(236) Price, W. D.; Schnier, P. D.; Williams, E. R. *J. Phys. Chem. B* **1997**, *101* (4), 664–673. https://doi.org/10.1021/jp9628702.
(237) Sciuto, S. V.; Liu, J.; Konermann, L. *J. Am. Soc. Mass Spectrom.* **2011**, *22* (10), 1679. https://doi.org/10.1007/s13361-011-0205-x.
(238) Armentrout, P. B.; Baer, T. *J. Phys. Chem.* **1996**, *100* (31), 12866–12877. https://doi.org/10.1021/jp953329t.
(239) Pratihar, S.; C. Kohale, S.; G. Bhakta, D.; Laskin, J.; L. Hase, W. *Phys. Chem. Chem. Phys.* **2014**, *16* (43), 23769–23778. https://doi.org/10.1039/C4CP03535F.
(240) Gordon, S. M.; Reid, N. W. *Int. J. Mass Spectrom. Ion Phys.* **1975**, *18* (4), 379–391. https://doi.org/10.1016/0020-7381(75)87054-9.
(241) Schnier, P. D.; Klassen, J. S.; Strittmatter, E. F.; Williams, E. R. *J. Am. Chem. Soc.* **1998**, *120* (37), 9605–9613. https://doi.org/10.1021/ja973534h.
(242) Jarrold, M. F. *Chem. Rev.* **2022**, *122* (8), 7415–7441. https://doi.org/10.1021/acs.chemrev.1c00377.
(243) Leney, A. C.; Heck, A. J. R. *J. Am. Soc. Mass Spectrom.* **2017**, *28* (1), 5–13. https://doi.org/10.1007/s13361-016-1545-3.
(244) Marcoux, J.; Robinson, C. V. *Structure* **2013**, *21* (9), 1541–1550. https://doi.org/10.1016/j.str.2013.08.002.
(245) Zhou, M.; Morgner, N.; Barrera, N. P.; Politis, A.; Isaacson, S. C.; Matak-Vinković, D.; Murata, T.; Bernal, R. A.; Stock, D.; Robinson, C. V. *Science* **2011**, *334* (6054), 380–385. https://doi.org/10.1126/science.1210148.
(246) van der Spoel, D.; Marklund, E. G.; Larsson, D. S. D.; Caleman, C. *Macromol. Biosci.* **2011**, *11* (1), 50–59. https://doi.org/10.1002/mabi.201000291.
(247) Yeagle, P. L. *Biochim. Biophys. Acta BBA - Biomembr.* **2014**, *1838* (6), 1548–1559. https://doi.org/10.1016/j.bbamem.2013.11.009.
(248) Laganowsky, A.; Reading, E.; Allison, T. M.; Ulmschneider, M. B.; Degiacomi, M. T.; Baldwin, A. J.; Robinson, C. V. *Nature* **2014**, *510* (7503), 172–175. https://doi.org/10.1038/nature13419.
(249) Poveda, J. A.; Giudici, A. M.; Renart, M. L.; Molina, M. L.; Montoya, E.; Fernández-Carvajal, A.; Fernández-Ballester, G.; Encinar, J. A.; González-Ros, J. M. *Biochim. Biophys. Acta BBA - Biomembr.* **2014**, *1838* (6), 1560–1567. https://doi.org/10.1016/j.bbamem.2013.10.023.
(250) Bechara, C.; Noll, A.; Morgner, N.; Degiacomi, M. T.; Tampe, R.; Robinson, C. V. *Biophys. J.* **2015**, *108* (2), 202a. https://doi.org/10.1016/j.bpj.2014.11.1119.
(251) Pliotas, C.; Dahl, A. C. E.; Rasmussen, T.; Mahendran, K. R.; Smith, T. K.; Marius, P.; Gault, J.; Banda, T.; Rasmussen, A.; Miller, S.; Robinson, C. V.; Bayley, H.; Sansom, M.

S. P.; Booth, I. R.; Naismith, J. H. *Nat. Struct. Mol. Biol.* **2015**, *22* (12), 991–998. https://doi.org/10.1038/nsmb.3120.
(252) Saliba, A.-E.; Vonkova, I.; Gavin, A.-C. *Nat. Rev. Mol. Cell Biol.* **2015**, *16* (12), 753–761. https://doi.org/10.1038/nrm4080.
(253) Hooker, B. S.; Bigelow, D. J.; Lin, C.-T. *Biochem. Biophys. Res. Commun.* **2007**, *363* (3), 457–461. https://doi.org/10.1016/j.bbrc.2007.09.031.
(254) Landreh, M.; Liko, I.; Uzdavinys, P.; Coincon, M.; Hopper, J. T. S.; Drew, D.; Robinson, C. V. *Chem. Commun.* **2015**, *51* (85), 15582–15584. https://doi.org/10.1039/C5CC07045G.
(255) Wilson, J. W.; Rolland, A. D.; Klausen, G. M.; Prell, J. S. *Anal. Chem.* **2019**, *91* (15), 10204–10211. https://doi.org/10.1021/acs.analchem.9b02243.
(256) Barrera, N. P.; Di Bartolo, N.; Booth, P. J.; Robinson, C. V. *Science* **2008**, *321* (5886), 243–246. https://doi.org/10.1126/science.1159292.
(257) Walker, L. R.; Marzluff, E. M.; Townsend, J. A.; Resager, W. C.; Marty, M. T. *Anal. Chem.* **2019**, *91* (14), 9284–9291. https://doi.org/10.1021/acs.analchem.9b02261.
(258) Marty, M. T.; Wilcox, K. C.; Klein, W. L.; Sligar, S. G. *Anal. Bioanal. Chem.* **2013**, *405* (12), 4009–4016. https://doi.org/10.1007/s00216-013-6790-8.
(259) Barrera, N. P.; Isaacson, S. C.; Zhou, M.; Bavro, V. N.; Welch, A.; Schaedler, T. A.; Seeger, M. A.; Miguel, R. N.; Korkhov, V. M.; van Veen, H. W.; Venter, H.; Walmsley, A. R.; Tate, C. G.; Robinson, C. V. *Nat. Methods* **2009**, *6* (8), 585–587. https://doi.org/10.1038/nmeth.1347.
(260) Barrera, N. P.; Robinson, C. V. *Annu. Rev. Biochem.* **2011**, *80* (1), 247–271. https://doi.org/10.1146/annurev-biochem-062309-093307.
(261) Bolla, J. R.; Corey, R. A.; Sahin, C.; Gault, J.; Hummer, A.; Hopper, J. T. S.; Lane, D. P.; Drew, D.; Allison, T. M.; Stansfeld, P. J.; Robinson, C. V.; Landreh, M. *Angew. Chem. Int. Ed.* **2020**, *59* (9), 3523–3528. https://doi.org/10.1002/anie.201914411.
(262) Liu, Y.; Cong, X.; Liu, W.; Laganowsky, A. *J. Am. Soc. Mass Spectrom.* **2017**, *28* (4), 579–586. https://doi.org/10.1007/s13361-016-1555-1.
(263) Reading, E.; Walton, T. A.; Liko, I.; Marty, M. T.; Laganowsky, A.; Rees, D. C.; Robinson, C. V. *Chem. Biol.* **2015**, *22* (5), 593–603. https://doi.org/10.1016/j.chembiol.2015.04.016.
(264) Patrick, J. W.; Boone, C. D.; Liu, W.; Conover, G. M.; Liu, Y.; Cong, X.; Laganowsky, A. *Proc. Natl. Acad. Sci.* **2018**, *115* (12), 2976–2981. https://doi.org/10.1073/pnas.1719813115.
(265) Liu, Y.; LoCaste, C. E.; Liu, W.; Poltash, M. L.; Russell, D. H.; Laganowsky, A. *Nat. Commun.* **2019**, *10* (1), 1352. https://doi.org/10.1038/s41467-019-09333-4.
(266) Zhang, Y.; Liu, L.; Daneshfar, R.; Kitova, E. N.; Li, C.; Jia, F.; Cairo, C. W.; Klassen, J. S. *Anal. Chem.* **2012**, *84* (18), 7618–7621. https://doi.org/10.1021/ac3023857.
(267) Li, J.; Han, L.; Li, J.; Kitova, E. N.; Xiong, Z. J.; Privé, G. G.; Klassen, J. S. *J. Am. Soc. Mass Spectrom.* **2018**, *29* (7), 1493–1504. https://doi.org/10.1007/s13361-018-1936-8.
(268) Sun, J.; Kitova, E. N.; Klassen, J. S. *Anal. Chem.* **2007**, *79* (2), 416–425. https://doi.org/10.1021/ac061109d.
(269) Eschweiler, J. D.; Kerr, R.; Rabuck-Gibbons, J.; Ruotolo, B. T. *Annu. Rev. Anal. Chem.* **2017**, *10* (1), 25–44. https://doi.org/10.1146/annurev-anchem-061516-045414.
(270) Niu, S.; Rabuck, J. N.; Ruotolo, B. T. *Curr. Opin. Chem. Biol.* **2013**, *17* (5), 809–817. https://doi.org/10.1016/j.cbpa.2013.06.019.

(271) Yin, V.; Konermann, L. *J. Am. Soc. Mass Spectrom.* **2021**, *32* (1), 73–83. https://doi.org/10.1021/jasms.0c00089.

(272) Silveira, J. A.; Fort, K. L.; Kim, D.; Servage, K. A.; Pierson, N. A.; Clemmer, D. E.; Russell, D. H. *J. Am. Chem. Soc.* **2013**, *135* (51), 19147–19153. https://doi.org/10.1021/ja4114193.

(273) Zhu, Y.; Roy, H. A.; Cunningham, N. A.; Strobehn, S. F.; Gao, J.; Munshi, M. U.; Berden, G.; Oomens, J.; Rodgers, M. T. *J. Am. Soc. Mass Spectrom.* **2017**, *28* (11), 2423–2437. https://doi.org/10.1007/s13361-017-1753-5.

(274) Wang, W.; Kitova, E. N.; Klassen, J. S. *Anal. Chem.* **2005**, *77* (10), 3060–3071. https://doi.org/10.1021/ac048433y.

(275) Wheeler, L. C.; Donor, M. T.; Prell, J. S.; Harms, M. J. *PLOS ONE* **2016**, *11* (10), e0164740. https://doi.org/10.1371/journal.pone.0164740.

(276) Susa, A. C.; Xia, Z.; Williams, E. R. *Anal. Chem.* **2017**, *89* (5), 3116–3122. https://doi.org/10.1021/acs.analchem.6b04897.

(277) Susa, A. C.; Lippens, J. L.; Xia, Z.; Loo, J. A.; Campuzano, I. D. G.; Williams, E. R. *J. Am. Soc. Mass Spectrom.* **2018**, *29* (1), 203–206. https://doi.org/10.1007/s13361-017-1793-x.

(278) Reardon, P. N.; Jara, K. A.; Rolland, A. D.; Smith, D. A.; Hoang, H. T. M.; Prell, J. S.; Barbar, E. J. *J. Biol. Chem.* **2020**, *295* (15), 4912–4922. https://doi.org/10.1074/jbc.RA119.011653.

(279) Marcoux, J.; Wang, S. C.; Politis, A.; Reading, E.; Ma, J.; Biggin, P. C.; Zhou, M.; Tao, H.; Zhang, Q.; Chang, G.; Morgner, N.; Robinson, C. V. *Proc. Natl. Acad. Sci.* **2013**, *110* (24), 9704–9709. https://doi.org/10.1073/pnas.1303888110.

(280) Leney, A. C.; Fan, X.; Kitova, E. N.; Klassen, J. S. *Anal. Chem.* **2014**, *86* (11), 5271–5277. https://doi.org/10.1021/ac4041179.

(281) Harvey, S. R.; Liu, Y.; Liu, W.; Wysocki, V. H.; Laganowsky, A. *Chem. Commun.* **2017**, *53* (21), 3106–3109. https://doi.org/10.1039/C6CC09606A.

(282) Chorev, D. S.; Baker, L. A.; Wu, D.; Beilsten-Edmands, V.; Rouse, S. L.; Zeev-Ben-Mordehai, T.; Jiko, C.; Samsudin, F.; Gerle, C.; Khalid, S.; Stewart, A. G.; Matthews, S. J.; Grünewald, K.; Robinson, C. V. *Science* **2018**, *362* (6416), 829–834. https://doi.org/10.1126/science.aau0976.

(283) Chorev, D. S.; Tang, H.; Rouse, S. L.; Bolla, J. R.; von Kügelgen, A.; Baker, L. A.; Wu, D.; Gault, J.; Grünewald, K.; Bharat, T. A. M.; Matthews, S. J.; Robinson, C. V. *Nat. Protoc.* **2020**, *15* (5), 1690–1706. https://doi.org/10.1038/s41596-020-0303-y.

(284) Anacleto, J. F.; Pleasance, S.; Boyd, R. K. *Org. Mass Spectrom.* **1992**, *27* (6), 660–666. https://doi.org/10.1002/oms.1210270603.

(285) Donor, M. T.; Ewing, S. A.; Zenaidee, M. A.; Donald, W. A.; Prell, J. S. *Anal. Chem.* **2017**, *89* (9), 5107–5114. https://doi.org/10.1021/acs.analchem.7b00673.

(286) Jones, J. L.; Dongre, A. R.; Somogyi, A.; Wysocki, V. H. *J. Am. Chem. Soc.* **1994**, *116* (18), 8368–8369. https://doi.org/10.1021/ja00097a055.

(287) Shelimov, K. B.; Clemmer, D. E.; Hudgins, R. R.; Jarrold, M. F. *J. Am. Chem. Soc.* **1997**, *119* (9), 2240–2248. https://doi.org/10.1021/ja9619059.

(288) Wyttenbach, T.; Paizs, B.; Barran, P.; Breci, L.; Liu, D.; Suhai, S.; Wysocki, V. H.; Bowers, M. T. *J. Am. Chem. Soc.* **2003**, *125* (45), 13768–13775. https://doi.org/10.1021/ja037204a.

(289) Bush, M. F.; O'Brien, J. T.; Prell, J. S.; Saykally, R. J.; Williams, E. R. *J. Am. Chem. Soc.* **2007**, *129* (6), 1612–1622. https://doi.org/10.1021/ja066335j.

(290) Oh, H.-B.; Lin, C.; Hwang, H. Y.; Zhai, H.; Breuker, K.; Zabrouskov, V.; Carpenter, B. K.; McLafferty, F. W. *J. Am. Chem. Soc.* **2005**, *127* (11), 4076–4083. https://doi.org/10.1021/ja040136n.

(291) Steill, J. D.; Oomens, J. *J. Am. Chem. Soc.* **2009**, *131* (38), 13570–13571. https://doi.org/10.1021/ja903877v.

(292) Hunter, E. P. L.; Lias, S. G. *J. Phys. Chem. Ref. Data* **1998**, *27* (3), 413–656. https://doi.org/10.1063/1.556018.

(293) Morris, R. A.; Knighton, W. B.; Viggiano, A. A.; Hoffman, B. C.; Schaefer III, H. F. *J. Chem. Phys.* **1997**, *106* (9), 3545–3547. https://doi.org/10.1063/1.473465.

(294) Beardsley, R. L.; Jones, C. M.; Galhena, A. S.; Wysocki, V. H. *Anal. Chem.* **2009**, *81* (4), 1347–1356. https://doi.org/10.1021/ac801883k.

(295) Benesch, J. L. P.; Aquilina, J. A.; Ruotolo, B. T.; Sobott, F.; Robinson, C. V. *Chem. Biol.* **2006**, *13* (6), 597–605. https://doi.org/10.1016/j.chembiol.2006.04.006.

(296) Wanasundara, S. N.; Thachuk, M. *J. Phys. Chem. B* **2010**, *114* (35), 11646–11653. https://doi.org/10.1021/jp103576b.

(297) Haynes, S. E.; Polasky, D. A.; Dixit, S. M.; Majmudar, J. D.; Neeson, K.; Ruotolo, B. T.; Martin, B. R. *Anal. Chem.* **2017**, *89* (11), 5669–5672. https://doi.org/10.1021/acs.analchem.7b00112.

(298) Cleary, S. P.; Thompson, A. M.; Prell, J. S. *Anal. Chem.* **2016**, *88* (12), 6205–6213. https://doi.org/10.1021/acs.analchem.6b01088.

(299) Hoi, K. K.; Robinson, C. V.; Marty, M. T. *Anal. Chem.* **2016**, *88* (12), 6199–6204. https://doi.org/10.1021/acs.analchem.6b00851.

(300) Cleary, S. P.; Prell, J. S. *Analyst* **2020**, *145* (13), 4688–4697. https://doi.org/10.1039/D0AN00726A.

(301) *Quantum Structure of the Intermolecular Proton Bond | Science*. https://www.science.org/doi/10.1126/science.1138962 (accessed 2024-02-09).

(302) Freeke, J.; Robinson, C. V.; Ruotolo, B. T. *Int. J. Mass Spectrom.* **2010**, *298* (1), 91–98. https://doi.org/10.1016/j.ijms.2009.08.001.

(303) Landreh, M.; Costeira-Paulo, J.; Gault, J.; Marklund, E. G.; Robinson, C. V. *Anal. Chem.* **2017**, *89* (14), 7425–7430. https://doi.org/10.1021/acs.analchem.7b00922.

(304) Kaldmäe, M.; Österlund, N.; Lianoudaki, D.; Sahin, C.; Bergman, P.; Nyman, T.; Kronqvist, N.; Ilag, L. L.; Allison, T. M.; Marklund, E. G.; Landreh, M. *J. Am. Soc. Mass Spectrom.* **2019**, *30* (8), 1385–1388. https://doi.org/10.1007/s13361-019-02177-8.

(305) Townsend, J. A.; Keener, J. E.; Miller, Z. M.; Prell, J. S.; Marty, M. T. *Anal. Chem.* **2019**, *91* (22), 14765–14772. https://doi.org/10.1021/acs.analchem.9b04263.

(306) Lemaire, D.; Marie, G.; Serani, L.; Laprévote, O. *Anal. Chem.* **2001**, *73* (8), 1699–1706. https://doi.org/10.1021/ac001276s.

(307) Polasky, D. A.; Dixit, S. M.; Keating, M. F.; Gadkari, V. V.; Andrews, P. C.; Ruotolo, B. T. *J. Am. Chem. Soc.* **2020**, *142* (14), 6750–6760. https://doi.org/10.1021/jacs.0c01076.

(308) Keetch, C. A.; Hernández, H.; Sterling, A.; Baumert, M.; Allen, M. H.; Robinson, C. V. *Anal. Chem.* **2003**, *75* (18), 4937–4941. https://doi.org/10.1021/ac034251c.

(309) Gabelica, V.; Vreuls, C.; Filée, P.; Duval, V.; Joris, B.; Pauw, E. D. *Rapid Commun. Mass Spectrom.* **2002**, *16* (18), 1723–1728. https://doi.org/10.1002/rcm.776.

(310) Hammerschmid, D.; van Dyck, J. F.; Sobott, F.; Calabrese, A. N. Interrogating Membrane ProteinProteinsStructure and LipidLipidsInteractions by Native Mass SpectrometryNative Mass Spectrometry. In *Biophysics of Membrane Proteins: Methods and Protocols*; Postis, V. L. G., Goldman, A., Eds.; Methods in Molecular Biology; Springer US: New York, NY, 2020; pp 233–261. https://doi.org/10.1007/978-1-0716-0724-4_11.

(311) Sobott, F.; Robinson, C. V. *Int. J. Mass Spectrom.* **2004**, *236* (1), 25–32. https://doi.org/10.1016/j.ijms.2004.05.010.

(312) Kirshenbaum, N.; Michaelevski, I.; Sharon, M. *J. Vis. Exp.* **2010**, No. 40, 1954. https://doi.org/10.3791/1954.

(313) Chen, C. J.; Williams, E. R. *Chem. Sci.* **2023**, *14* (18), 4704–4713. https://doi.org/10.1039/D3SC00259D.

(314) Oh, M. I.; Consta, S. *J. Phys. Chem. Lett.* **2017**, *8* (1), 80–85. https://doi.org/10.1021/acs.jpclett.6b02319.

(315) Van Berkel, G. J.; Asano, K. G.; Schnier, P. D. *J. Am. Soc. Mass Spectrom.* **2001**, *12* (7), 853–862. https://doi.org/10.1016/S1044-0305(01)00264-1.

(316) Dixit, S. M.; Polasky, D. A.; Ruotolo, B. T. *Curr. Opin. Chem. Biol.* **2018**, *42*, 93–100. https://doi.org/10.1016/j.cbpa.2017.11.010.

(317) Hopper, J. T. S.; Oldham, N. J. *J. Am. Soc. Mass Spectrom.* **2009**, *20* (10), 1851–1858. https://doi.org/10.1016/j.jasms.2009.06.010.

(318) Alexander IV, J. N.; Schultz, G. A.; Poli, J. B. *Rapid Commun. Mass Spectrom.* **1998**, *12* (17), 1187–1191. https://doi.org/10.1002/(SICI)1097-0231(19980915)12:17<1187::AID-RCM300>3.0.CO;2-T.

(319) Marty, M. T. *J. Am. Soc. Mass Spectrom.* **2022**, *33* (10), 1807–1812. https://doi.org/10.1021/jasms.2c00218.

(320) Britt, H. M.; Cragnolini, T.; Thalassinos, K. *Chem. Rev.* **2022**, *122* (8), 7952–7986. https://doi.org/10.1021/acs.chemrev.1c00356.

(321) Hopper, J. T. S.; Robinson, C. V. *Angew. Chem. Int. Ed.* **2014**, *53* (51), 14002–14015. https://doi.org/10.1002/anie.201403741.

(322) Eschweiler, J. D.; Martini, R. M.; Ruotolo, B. T. *J. Am. Chem. Soc.* **2017**, *139* (1), 534–540. https://doi.org/10.1021/jacs.6b11678.

(323) Deng, L.; Kitova, E. N.; Klassen, J. S. *J. Am. Soc. Mass Spectrom.* **2013**, *24* (1), 49–56. https://doi.org/10.1007/s13361-012-0533-5.

(324) McLuckey, S. A.; Van Berkel, G. J.; Goeringer, D. E.; Glish, G. L. *Anal. Chem.* **1994**, *66* (14), 737A-743A. https://doi.org/10.1021/ac00086a001.

(325) Goeringer, D. E.; McLuckey, S. A. *J. Chem. Phys.* **1996**, *104* (6), 2214–2221. https://doi.org/10.1063/1.471812.

(326) McLuckeya, S. A.; Wells, J. M.; Stephenson, J. L.; Goeringer, D. E. *Int. J. Mass Spectrom.* **2000**, *200* (1), 137–161. https://doi.org/10.1016/S1387-3806(00)00306-7.

(327) Mehnert, S. A.; Fischer, J. L.; McDaniel, M. R.; Fabijanczuk, K. C.; McLuckey, S. A. *J. Am. Soc. Mass Spectrom.* **2023**, *34* (6), 1166–1174. https://doi.org/10.1021/jasms.3c00109.

(328) Shepherd, S. O.; Green, A. W.; Resendiz, E. S.; Newton, K. R.; Kurulugama, R. T.; Prell, J. S. *J. Am. Soc. Mass Spectrom.* **2024**. https://doi.org/10.1021/jasms.3c00371.

(329) Larriba, C.; Hogan, C. J. *J. Comput. Phys.* **2013**, *251*, 344–363. https://doi.org/10.1016/j.jcp.2013.05.038.

(330) Ewing, S. A.; Donor, M. T.; Wilson, J. W.; Prell, J. S. *J. Am. Soc. Mass Spectrom.* **2017**, *28* (4), 587–596. https://doi.org/10.1007/s13361-017-1594-2.
(331) Dunbar, R. C. *Mass Spectrom. Rev.* **2004**, *23* (2), 127–158. https://doi.org/10.1002/mas.10074.
(332) Armentrout, P. B. *J. Am. Soc. Mass Spectrom.* **2000**, *11* (5), 371–379. https://doi.org/10.1016/S1044-0305(00)00102-1.
(333) Wilson, J. W.; Donor, M. T.; Shepherd, S. O.; Prell, J. S. *J. Am. Soc. Mass Spectrom.* **2020**, *31* (8), 1751–1754. https://doi.org/10.1021/jasms.0c00117.